Laser Sintered Nanograin SiGe Thermoelectric Thin Film Devices

A Dissertation

Presented to the Faculty of the Graduate School

University of Virginia

In Partial Fulfillment of the Requirements for the Degree of

Doctor of Philosophy in Electrical Engineering

by

Kai Xie

December 2019

Abstract

The energy crisis and environmental problem are drawing more attention to renewable energy research in recent decades. Thermoelectric materials can convert heat directly into electricity with the advantages of long lifespan, maintenance-free operation, and excellent reliability. Si-Ge has been used as the high-temperature thermoelectric material in radioisotope thermoelectric generators (RTGs) by NASA in deep space missions and Moon landings. However, the relatively high cost and low conversion efficiency limit the application of the thermoelectric materials for energy conversion. In this work, laser processing is expected to provide an effective solution to the efficiency and cost problems of thermoelectric materials.

In order to increase the conversion efficiency, thermoelectric materials should have high electrical conductivity, high Seebeck coefficient, and low thermal conductivity, as per the definition of the figure of merit. Laser sintering could minimize grain growth, and thus reduce thermal conductivity via phonon scattering at the grain boundaries. The figure of merit is expected to be enhanced by the reduced thermal conductivity without an appreciable loss in electrical conductivity. In addition, the conversion efficiency is also related to the temperature difference between the hot side and the cold side of the thermoelectric device. The thin-film thermoelectric device has the advantage of high-temperature differences, which also improves conversion efficiency. In terms of the fabrication cost, laser processing has the advantages of low cost, high efficiency, high throughput, and easy operation, which is suitable for large scale manufacturing. Therefore, the laser processing is expected to fabricate thermoelectric devices with high performance and low cost, which is more suitable for commercialization and mass production.

In this work, plasma-synthesis and ball-milling were investigated as the synthesis methods of as-deposited thin films, followed by laser sintering using a quasi-continues-wave infrared

laser. The plasma-synthesized-laser-sintered (PSLS) method resulted in a grain size of 68 nm, which reduced the thermal conductivity to ~1.35 W/m·K from room temperature to 573 K. The Seebeck coefficient increased from 144.9 μV/K at room temperature to 390.1 μV/K at 873 K. The electrical conductivity increased from 16.1 S/cm at room temperature to 62.1 S/cm at 873 K. The figure of merit of the PSLS $Si_{80}Ge_{20}$ was calculated to be 0.60 at 873 K, which is comparable to a value of ~1 for bulk nanostructured materials. The ball-milled-laser-sintered (BMLS) method produced well-alloyed $Si_{80}Ge_{20}$ with an average grain size of 50 nm. The thermal conductivity was found to be ~1.5 W/m·K from room temperature to 573 K. The Seebeck coefficient was 120.2 μV/K at room temperature to 301.5 μV/K at 873 K. The electrical conductivity was measured as 80.9 S/cm at room temperature and 118.5 S/cm at 873 K. Therefore, the figure of merit of the BMLS $Si_{80}Ge_{20}$ was found to be 0.63 at 873 K.

In addition, a device consists of 3 pairs of n-type phosphorus-doped $Si_{80}Ge_{20}$ legs and p-type boron-doped $Si_{80}Ge_{20}$ legs were fabricated with the BMLS method. The maximum temperature difference of 200 K was achieved when the hot-side temperature was 873 K, and the cold side was kept at room temperature in the air (no water cooling). The corresponding maximum thermovoltage and output-power were 311.6 mV and 15.85 μW. The effective power density was calculated as 8.8 mW/cm^2.

In summary, a new method for thermoelectric thin film fabrication using laser sintering of Si and Ge nanoparticles has been demonstrated with a thermal-to-electric conversion efficiency approaching the bulk value. Also, a fundamental understanding of laser-sintered $Si_{80}Ge_{20}$ thermoelectric materials has been provided, and a novel and viable concept of laser processing has been demonstrated for high-efficiency and low-cost thermoelectric device fabrication.

Acknowledgment

I would like to express my deepest appreciation to my advisor, Prof. Mool C. Gupta. I am extremely grateful for the guidance and support he provided in my doctoral studies. Prof. Gupta is a talented scientist and thoughtful mentor. I have learned a lot from his passion for research, deep thinking, rigorous attitude, and supportive mentoring style, which would be incredibly valuable in my future research/career life. I would also like to express my gratitude to my committee members, Prof. Mona Zebarjadi, Prof. Jon Ihlefeld, Prof. Patrick E. Hopkins, and Prof. Kyusang Lee, for the insightful comments and suggestions in the dissertation process.

It was my absolute pleasure to work and spend time with my colleagues in Prof. Gupta's group. Many thanks to Dr. Moon-Hyung Jang, Dr. Ahmed Rasin, Dr. Peixun Fan, Dr. Chris Duska, Dr. Zeming Sun, George Wilkes, Arpan Sinha, Elisa Pantoja, Alan Mulroney, Matt Julian, and Joel Harrison for their friendship and their help in my research. I sincerely thank my collaborators, Prof. Uwe Kortshagen, and his students, Ranee Skinner and Kelsey Mork, from the University of Minnesota.

I would also like to acknowledge the support of the National Science Foundation (NSF) under the award number ECCS-1408443, NASA Langley professor program, and Industry/University Cooperative Research Centers (I/UCRC) program. Thanks to all Nanoscale Materials Characterization Facility (NMCF) and Microfabrication Laboratories UVML facility members, including Richard White, Joseph Thompson, and Catherine A. Dukes. Thanks to ECE staff, including Crystal Aldridge, Dan Fetko, Beth Eastwood-Beatty, and Susan Malone.

I’m deeply indebted to my parents, my mother-in-law, and my grandmother. Their love, support, sacrifices, and encouragement allowed me to pursue academic dreams in the United States. I would like to give special thanks to my wife, Lingjun. Your love and support are the most valuable things to me in the world. We have overcome so many difficulties in our doctoral studies, and I am confident in our future for the rest of life.

Table of Contents

List of Figures

List of Tables

List of Symbols, Abbreviations, and Acronyms

Ar	argon
BMLS	ball-milled-laser-sintered
CPU	central processing unit
CVD	chemical vapor deposition
EDS/EDX	energy-dispersive X-ray spectroscopy
FAST	field-assisted sintering technique
GeH_4	germane
GPHS	general-purpose heat source
H_2	hydrogen
HAADF	high-angle annular dark-field imaging
IC	integrated circuit
IPA	isopropyl alcohol
LPCVD	low-pressure chemical vapor deposition
MBE	molecular beam epitaxy
MEMS	microelectromechanical systems
MOCVD	metal-organic chemical vapor deposition
NC	nanocrystalline
NP	nanoparticles
PED	pulse electroplating
PH_3	phosphine
PID	proportional–integral–derivative
PRR	pulse repetition rate
PSLS	plasma-synthesized-laser-sintered
QCW	quasi-continuous wave
RF	radio frequency
RPM	revolutions per minute
RTG	radioisotope thermoelectric generator
SEM	scanning electron microscope
SiH_4	silane
SIMS	secondary-ion mass spectrometry
SPS	spark plasma sintering
STEM	scanning transmission electron microscopy
TC	thermocouple
TCR	temperature coefficient of resistance
TDTR	time-domain thermoreflectance

TE	thermoelectric
TEG	thermoelectric generator
TEM	transmission electron microscopy
XRD	X-ray diffraction
ZT	figure of merit
XPS	X-ray photoelectron spectroscopy

η_{max}	conversion efficiency
κ	thermal conductivity.
κ_e	electronic thermal conductivity
κ_L	lattice thermal conductivity
λ	wavelength
μ	charge carrier mobility
ρ	electrical resistivity
σ	electrical conductivity
τ	the average time between electron scattering events
$\overline{E}$	the average charge carrier energy
$\overline{T}$	average temperature
A_e	effective device area
C	heat capacity at a constant volume
D	the diameter of the beam prior to the lens
e	elementary charge
E_f	Fermi energy
F	the focal length of the lens
h	Planck constant
I_{work}	working current
k_B	Boltzmann constant
L	Lorenz number
l	phonon mean free path
m^*	carrier effective mass
n	carrier density
P_{max}	maximum output power
P_{out}	power output
R	electrical resistance
R_{int}	internal resistance
S	Seebeck coefficient

T	temperature
T_C	the temperature at the cold side
t_f	film thickness
T_H	the temperature at the hot side
v	the velocity of the phonons
$V_{1\omega}$	first third harmonic voltage
$V_{3\omega}$	third harmonic voltage
V_{load}	the voltage on the load
V_{oc}	open-circuit voltage
w_0	beam waist
$Z\overline{T}$	device thermoelectric figure of merit
$\mathit{\Delta} T_f$	temperature rise in the measured film
$\mathit{\Delta} T_{ref}$	temperature rise in the reference device
$\mathit{\Delta} T_{sample}$	temperature rise in the sample device

Chapter 1. Introduction

1.1. Thermoelectric Materials Overview

1.1.1. General Introduction of Thermoelectric Materials

The energy crisis and environmental deterioration are drawing more attention to renewable energy research in recent decades [1–4]. Although the share of renewable energy is growing, the main source of energy is still fossil fuel worldwide [5]. Fossil-based systems generate a large amount of waste heat, which reduces the total efficiency and generate greenhouse gas at the same time. If the waste heat can be collected and converted to useful energy, it can both fulfill the energy consumption demand and reduce environmental contamination.

Thermoelectric materials can convert heat directly into electricity based on the Seebeck effect discovered by Thomas Johann Seebeck in 1821. The physical explanation of the Seebeck effect is the diffusion of mobile carriers. The mobile charge carriers (electrons or holes) at the hot side have higher thermal energy than those at the cold side. Therefore, the mobile charge carriers will diffuse to the cold side to achieve energy equilibrium. The voltage difference between the hot side and the cold side is called thermovoltage, which is proportional to the temperature difference. The thermovoltage generated per unit temperature is called the Seebeck coefficient.

A typical thermoelectric module is shown in Figure 1.1. The mobile charge carriers are electrons in n-type semiconductors and holes in p-type semiconductors. Both mobile charge carriers have a higher density at the cold side than at the hot side. Therefore, the current flow driven by the thermovoltage is clockwise in the schematic diagram. One p-leg and one n-leg are called one unicouple. In practical applications, thermoelectric generators (TEGs) consist of unicouples connected in serial and in parallel [6, 7].

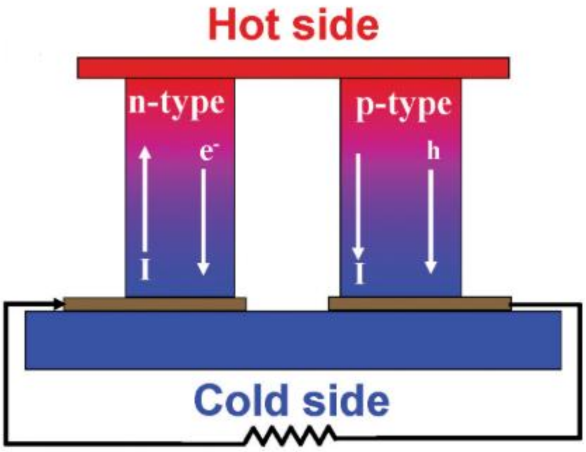

Figure 1.1. Schematic diagram of a thermoelectric generator. Image reprinted from [8].

There are many advantages of TEGs, which includes: 1) simple structure, as the p- and n-legs can be compacted into a limited space; 2) no moving parts or fluids, which means high reliability and maintenance-free; 3) long lifespan, which means when the heat source is available, TEGs can provide a stable and reliable power supply [9].

However, although there are many advantages of thermoelectric materials, the market share of thermoelectrics in renewable energy is still very low [10, 11]. The relatively high cost and low conversion efficiency limit the application of the thermoelectric materials for energy conversion. The conversion efficiency (η_{max}) is expressed as:

$$\eta_{\text{max}} = \frac{T_{\text{H}} - T_{\text{C}}}{T_{\text{H}}} \cdot \frac{\sqrt{1 + Z\overline{T}} - 1}{\sqrt{1 + Z\overline{T}} + \frac{T_{\text{C}}}{T_{\text{H}}}}$$

where T_{H} and T_{C} are the temperatures at the hot side and the cold side, respectively.

$Z\overline{T}$ is the device figure of merit for thermoelectric materials. If the device has only one n-leg or p-leg, the device figure of merit can be expressed as:

$$Z\overline{T} = \frac{\sigma S^2 \overline{T}}{\kappa}$$

where σ is the electrical conductivity, S is the Seebeck coefficient, $\overline{T}$ is the average temperature of the hot side and cold side, and κ is the thermal conductivity.

Therefore, in order to get a good figure of merit, thermoelectric materials should have high electrical conductivity, high Seebeck coefficient, and low thermal conductivity. Moreover, the high conversion efficiency requires a high figure of merit and a large temperature difference.

The efficiency dependence on the heat source temperature with different ZT is shown in Figure 1.2. Currently, available TE materials only have a ZT of around 2. Moreover, most of the high ZT thermoelectric materials (BiTe, SnSe, PbTe) could not work under high temperatures (> 1000K). The most commonly used high-temperature TE material is Si-Ge, which could work under temperatures up to 1300 K [12]. However, the ZT of Si-Ge is not as high as low- and middle-temperature thermoelectric materials.

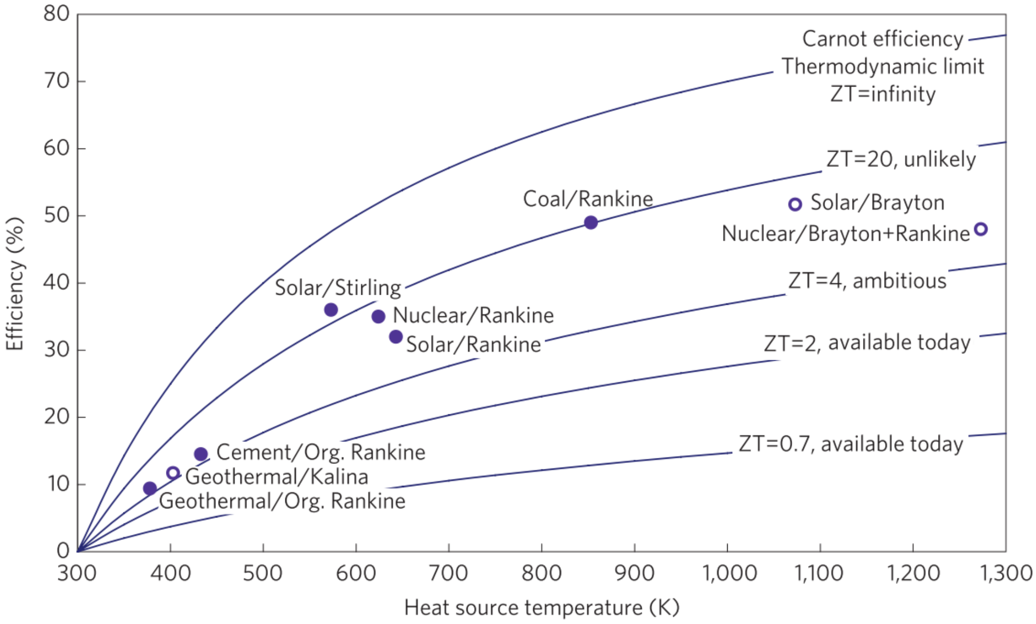

Figure 1.2. The efficiency dependence on the heat source temperature with different ZT when the cold side is at 300 K. Image adapted from [13].

1.1.2. Temperature Dependence of Thermoelectric Properties of Different Materials

Figure 1.3 shows the state-of-the-art figure of merit for thermoelectric materials at different temperatures. Bi-Te, Sn-Se, and Si-Ge are the best candidates because of their high figure of merits. They are the most promising thermoelectric materials for low, middle, and high-temperature applications, respectively.

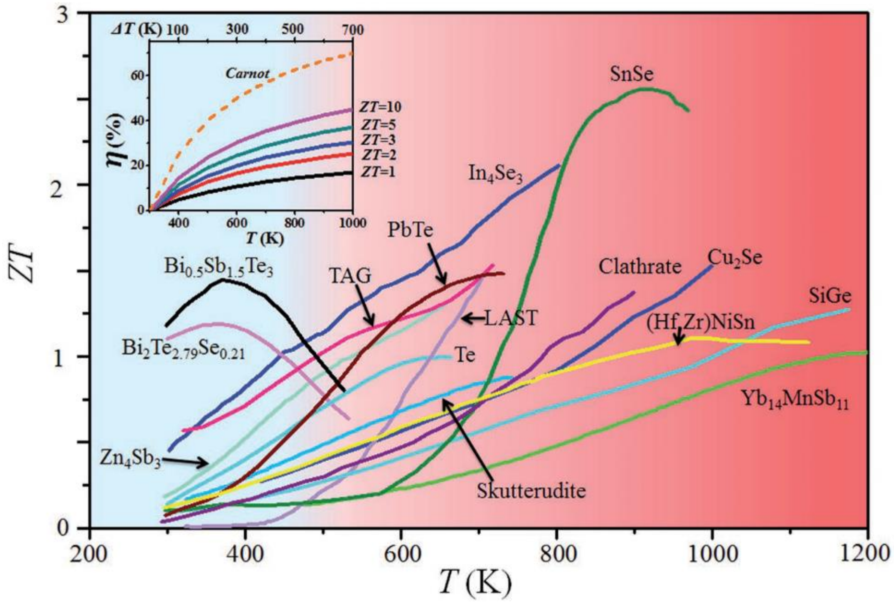

Figure 1.3. ZT as a function of temperature for typical high-efficiency thermoelectric materials, inset is the relation between η, T, and ΔT of materials with different ZT values. Image reprinted from [14].

For low-temperature range applications from room temperature to 573 K, wearable devices and flexible thermoelectric materials are of the most interest. Bismuth telluride (Bi_2Te_3) based materials have the highest ZT values in this temperature range. The nanostructured p-type $Bi_{0.5}Sb_{1.5}Te_3$ showed a ZT of ~1.4 at 373 K enhanced by reducing thermal conductivity via the increased phonon scattering at grain boundaries and defects [15–17]. For an n-type material, the nanostructured $Bi_2Se_{0.3}Te_{2.7}$ showed a ZT of 1.04 at 400 K and was synthesized by hot pressing [18].

For middle-temperature range applications from 573 K to 973 K, the highest ZT thermoelectric material is single-crystal SnSe, which was reported to have a ZT of 2.6 at 923 K in the b-axis direction, which benefits from its ultralow lattice thermal conductivity of 0.25 W/m·K [19–21]. The state-of-the-art textured SnSe polycrystals were fabricated by solvothermal synthesis followed by spark plasma sintering (SPS), which achieved a ZT of 1.36 at 823 K [22]. The untextured SnSe polycrystals doped with Na were fabricated by the conventional melting and annealing method, which showed a ZT of 0.8 at 800 K [23].

For temperature higher than 973 K, Si-Ge is the most promising material due to its high-temperature stability. Si-Ge has been demonstrated as the best composition to achieve a high thermoelectric figure of merit. In NASA deep space missions, a Pu-238 heat source is used in RTGs, and the hot side temperature is 1273 K. Therefore, $Si_{80}Ge_{20}$ is used to make TE modules in RTGs. In 2008, MIT and Boston research group improved the ZT of n-type and p-type $Si_{80}Ge_{20}$ to 1.3 at 1173 K [24] and 0.95 at 1187 K [25], respectively. The direct current hot press was used to make bulk materials with nano-grain structures in both studies.

1.1.3. Thermoelectric Applications

1.1.3.1. Radioisotope thermoelectric generator

Compared with other power sources, thermoelectric devices have many unique advantages, such as long lifespan, maintenance-free operation, and excellent reliability [26]. RTGs have been the best and the only power source when solar energy is not available, such as in deep space missions and Moon landings [27].

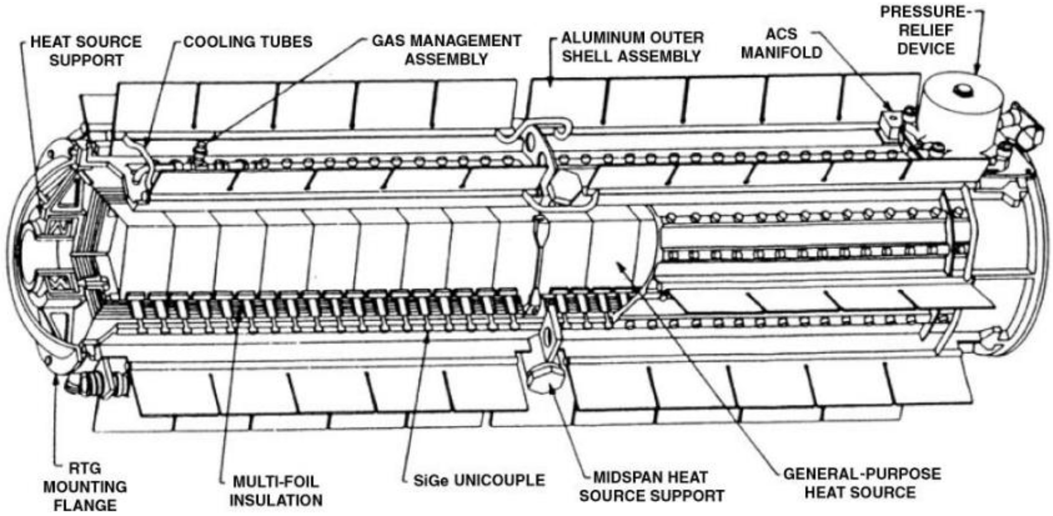

Figure 1.4. Schematic diagram of a general-purpose heat source radioisotope thermoelectric generator (GPHS-RTG) using $Si_{80}Ge_{20}$ thermoelectric elements. Image reprinted from [28].

The structure of a GPHS-RTG is shown in Figure 1.4. It has been used in several space missions such as the Cassini–Huygens, New Horizons, Galileo, and Ulysses [29]. The stability and reliability of RTGs have been well proven by the successes in these missions. In GPHS-RTG, a Pu-238 heat source is used to provide the input heat (4500 W) to the 18 Si-Ge thermoelectric converters. The temperatures of the hot-end and cold-end were 1273 K and 573 K, respectively. However, the efficiency of a GPHS-RTG is only 6.3% due to the low figure of merit of the $Si_{80}Ge_{20}$ [30].

For space missions, the specific power (watt per kilogram) is more important than efficiency alone [31]. The GPHS-RTG has a specific power of 5.1 W/kg, compared with early RTG designs at ~1.4 W/kg. Although the specific power of RTGs is much lower than solar panels, it still operates better when the spacecraft travels away from the sun.

1.1.3.2. Wearable device

In recent years, wearable devices have attracted significant attention in both the areas of business and science [32–35]. TEGs could become an alternative power source and provide up to a few watts for wearable devices [36, 37]. Wearable thermoelectric devices could be used to power fitness bracelets, health monitoring devices, and wireless sensors [38].

Because the human body is not a flat surface, a flexible thermoelectric generator is more suitable for over the skin applications. A prototype of a flexible TEG developed by We et al. is shown in Figure 1.5. The output voltage of the module was 12.1 mV at a temperature difference of approximately 5 K. It also has good bending fatigue strength. The results indicate that flexible thermoelectric devices are promising for mobile device powering.

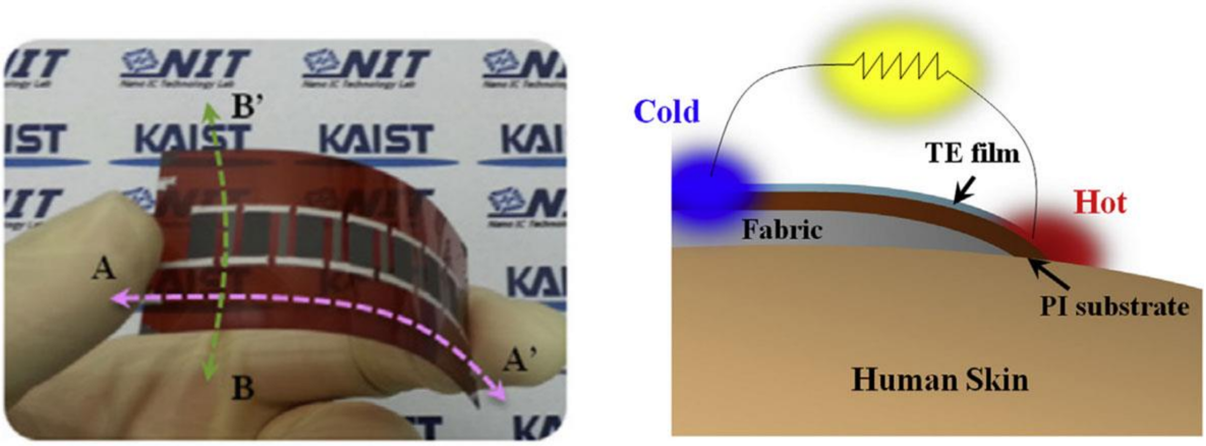

Figure 1.5. (left) Image of a bendable thermoelectric device. (right) Schematic diagram of a TEG mounted on human skin. Image adapted from [39].

1.1.3.3. Automotive TEG

A majority of automobile engine power is wasted as heat in the exhaust and coolant instead of generating the power output. In order to increase the efficiency of the engine, many automobile manufacturers have demonstrated their interest in exhaust heat recovery. BMW, Ford, Renault, and Honda are considering the use of thermoelectric devices to recover the waste heat [4]. Examples of a rectangular shaped heat exchanger can be seen in Figure 1.6 (left). A prototype TEG exhaust heat recovery system developed by Honda is shown in Figure 1.6 (right). The prototype TEG is predicted to produce approximately 1 kW of power. The claimed fuel consumption reduction is 3%. This technology is not effective enough to be installed in commercialized cars and is still in the development stages. Moreover, it also increases the complexity and cost. More effort and research are needed before moving to mass production stages.

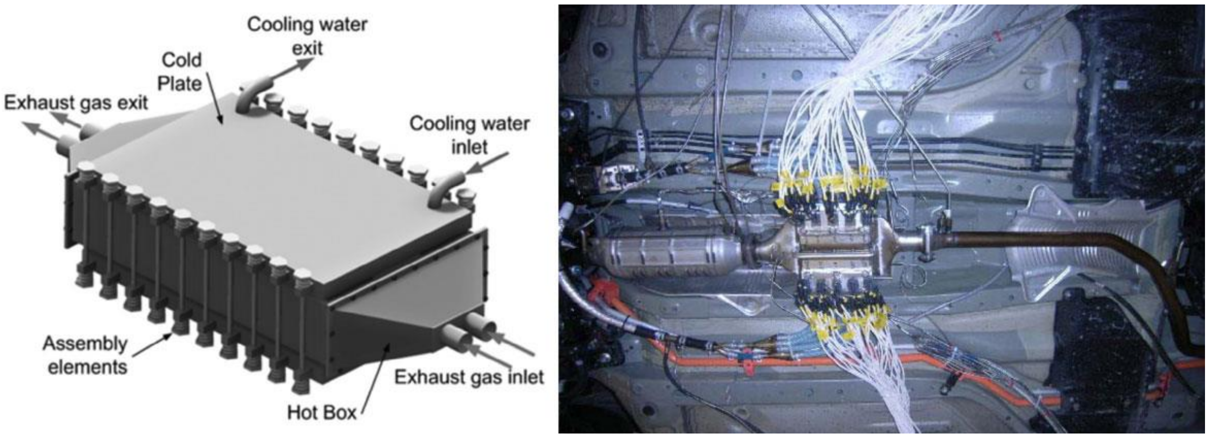

Figure 1.6. (left) Schematic diagram of a rectangular exhaust heat exchanger. (right) Honda prototype TEG exhaust heat recovery system. Both images adapted from [4].

1.1.3.4. On-chip cooling

When an electric current is passed through the circuit of a thermocouple, heat is released at one junction and absorbed at the other junction. This is known as the Peltier Effect, which was discovered by Jean Charles Athanase Peltier in 1834. The Peltier effect is the inverse of the Seebeck effect. Most thermoelectric generators could also be used as Peltier coolers, and vice versa.

The rapid development of micro-devices is targeting better performance and smaller size. On the other hand, the high integration density leads to a great challenge in thermal management. In general, microelectronics, MEMS, and microsensors work better at a low temperature. For example, 2 K above the permissible operating temperature can induce a 10% decrease in chip reliability [40]. Micro Peltier coolers are one of the most promising solutions for on-chip cooling because of their outstanding advantages: no moving parts, high reliability, maintenance-free, and long lifespan. More importantly, micro Peltier coolers are well compatible with chip-manufacturing and thus create well-integrated devices.

Figure 1.7 shows a free-standing on-chip cooling design. The chip is in the middle part, which is also the heat source. The transparent green part is the thermoelectric material. When the current is applied, the middle chip is cooled by the on-chip cooler, and the heat is dispersed to the gray part. Su et al. reported that this design is able to create 10.3 K and 11.2 K cooling temperatures in single-stage and two-stage micro-refrigerators, respectively [41].

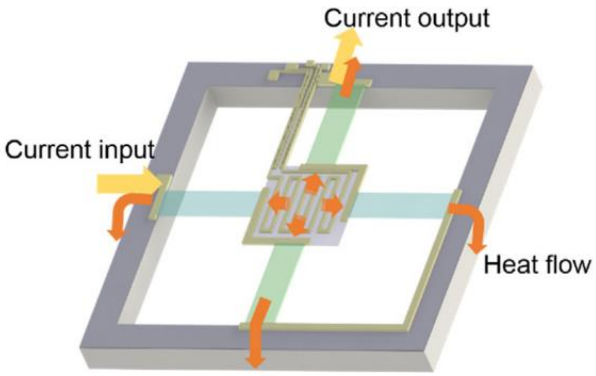

Figure 1.7. Schematic diagram of a free-standing on-chip cooling design. Image reprinted from [41].

1.2. Laser Processing

Lasers have been proved to be a successful tool for large scale manufacturing, because of their low cost, high efficiency, high throughput, and easy operation. In renewable energy applications, laser processing was reported to perform laser doping [42], laser transferring [43], and laser texturing [44], etc.

Laser processing has unique advantages for fabrication processes [45]. Selective laser sintering can heat the sample material to the desired temperature without heating the substrate to the same temperature. This provides a wide substrate selection when compared with conventional methods. Meanwhile, the short duration of the laser pulse and controllable repetition rate could minimize grain growth during processing, which could also reduce the thermal conductivity via nanostructuring. Laser sintering also has much better fabrication efficiency and throughput when compared with traditional sintering methods such as the hot press. Additionally, laser sintering could fabricate the thermoelectric material on top of an arbitrarily shaped surface. Laser sintering can also provide thin-film fabrication using nano- or micro-particles. Therefore, laser sintering could be a fast, easy, and low-cost fabrication method, which is more suitable for commercialization and mass production.

1.3. Challenges and Motivation

Currently, the low efficiency and high cost are the main problems of thermoelectric power generation for large-scale commercialization. The performance of the thermoelectric materials could be improved by nanostructuring, which has been proven to be a promising approach to reduce the thermal conductivity via enhanced phonon scattering at grain boundaries [46–48]. Laser sintering allows fast heating and cooling rates, which could minimize grain growth and lead to nanostructured thermoelectric materials. Additionally, laser sintering is fast, easy, and cost-effective. Therefore, laser sintering is expected to provide an effective solution to the efficiency and cost problems of thermoelectric materials.

Furthermore, studies on thin-film thermoelectric materials are very limited as compared to bulks. Although thin-film thermoelectric materials are more difficult to fabricate and characterize, they also have many advantages compared with the bulk alloy. 1) Thin films are more suitable for large-area applications; 2) thin films have larger dimensions with the same weight, which means larger temperature gradient and lager thermovoltage [49]. 3) Thin films can be easily integrated into planar devices. Therefore, it is important to study the whole fabrication process, such as nanoparticle thin film preparation, laser sintering parameters optimization, and thermoelectric property characterization and device fabrication.

Finally, the fabrication of thermoelectric devices is the other important topic in this work. Traditionally, the n- and p- legs are synthesized separately, then interconnected using welding.

In this work, laser sintering is used to pattern p- and n- legs, which simplify the device fabrication steps for better efficiency and lower cost.

1.4. Research Objectives and Thesis Outline

The objective of this research is to investigate the thermoelectric properties of $Si_{80}Ge_{20}$ thin films prepared by laser sintering of nanoparticles and demonstrate a fast, easy, and cost-effective way to fabricate nanostructured thermoelectric devices. Laser sintering could minimize grain growth, and thus reduce thermal conductivity via phonon scattering at the grain boundaries. The figure of merit is expected to be enhanced by the reduced thermal conductivity without an appreciable loss in electrical conductivity. Laser sintering does not require vacuum-environment and is suitable for the "printing process". Therefore, the laser processing is expected to fabricate thermoelectric devices with high performance and low cost.

The thesis outline is summarized in Figure 1.8. This dissertation is organized in various chapters related to the fabrication, characterization, and device fabrication. After the literature review in Chapter Chapter 2, the fabrication, characterization, and discussions of $Si_{80}Ge_{20}$ as thermoelectric materials are included in Chapter Chapter 3 to Chapter Chapter 5. Then the thermoelectric device fabrication is investigated in Chapter Chapter 6. The details of each chapter are summarized as follows:

$Si_{80}Ge_{20}$ NPs are synthesized and coated onto the quartz substrate before laser sintering. Two different synthesize methods of as-deposited thin films were investigated. 1) Hydrogen terminated $Si_{80}Ge_{20}$ nanocrystals with 5% nominal doping were grown in a capacitively coupled plasma tube reactor and deposited onto a quartz substrate in porous thin films. Plasma synthesis was part of the collaboration with the University of Minnesota [50]. 2) Ball-milling followed by solution coating was the second method. The Si, Ge, and dopant were mixed, and ball milled to get an NP suspension. The NP suspension was spin-coated on the substrate to obtain as-deposited thin films. Both of the plasma synthesis method and the ball milling method followed by laser sintering are discussed in Chapter Chapter 3.

The characterization methods for laser-sintered thermoelectric thin films and devices are discussed in Chapter Chapter 4. The characterization results of $Si_{80}Ge_{20}$ thin films and discussions are included in Chapter Chapter 5. The objective of materials studies in Chapter Chapter 3 to Chapter Chapter 5 is to obtain laser-sintered $Si_{80}Ge_{20}$ thin films with an enhanced figure of merit via nanostructuring.

Lastly, thermoelectric p- and n- legs were fabricated and integrated to form a thin film TEG. The fabrication and characterization results are discussed in Chapter Chapter 6.

Conclusion and future work are presented in Chapter Chapter 7.

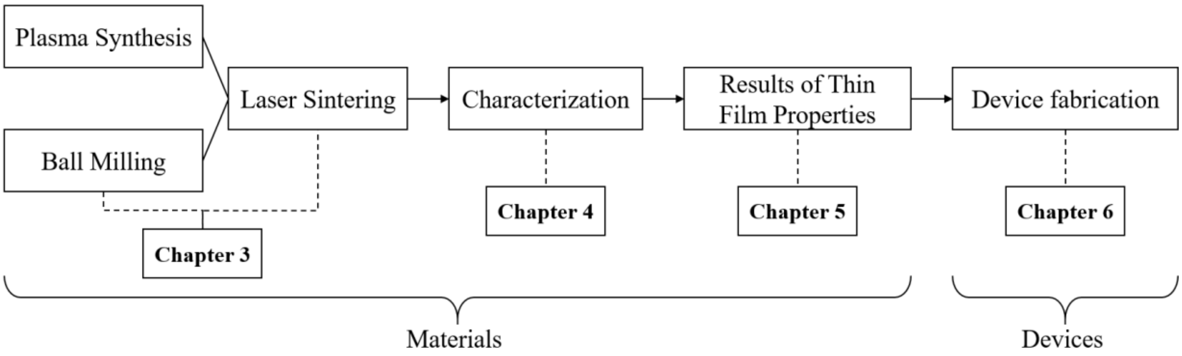

Figure 1.8. Thesis outline.

Chapter 2. Background Information and Literature Review

2.1. Physics of Thermoelectric Materials

The performance of the thermoelectric materials is characterized by:

$$Z\overline{T} = \frac{\sigma S^2 \overline{T}}{\kappa}$$

where σ is the electrical conductivity, S is the Seebeck coefficient, $\overline{T}$ is the average temperature of the hot side and cold side, and κ is the thermal conductivity.

Therefore, in order to get a good figure of merit, thermoelectric materials should have high electrical conductivity, high Seebeck coefficient, and low thermal conductivity. All three physical properties are related to the material band structure and correlated with each other. It is important to find a balance among these parameters. Discussion based on each parameter is provided separately in the following sections.

2.1.1. Electrical Conductivity

The electrical conductivity σ is determined by:

$$\sigma = \frac{1}{\rho} = ne\mu \qquad \text{Equation 2-1}$$

where ρ is the electrical resistivity, n is the carrier density, e is the elementary charge, and μ is the charge carrier mobility.

The charge carrier mobility μ could be calculated by:

$$\mu = \frac{e\tau}{m^*} \qquad \text{Equation 2-2}$$

where e is the elementary charge, τ is the average time between electron scattering events, and m^* is the carrier effective mass.

Therefore, the electrical conductivity could be increased by 1) increasing the carrier density n, or 2) increasing the charge carrier mobility μ. However, increasing the carrier density will also decrease the Seebeck coefficient. Increasing the charge carrier mobility can be realized in two ways, decreasing the carrier effective mass m^* or increasing the scattering time τ. However, the former will also decrease the Seebeck coefficient. The latter is usually realized by reducing the number of defects, dislocations, or impurities, which will also increase thermal conductivity [48, 51].

2.1.2. Seebeck Coefficient

The Seebeck coefficient can be estimated with the following equation for nearly free electrons.

$$\mathrm{S} = \frac{8\pi^2 k_B^2}{3eh^2}\mathrm{m}^* T\left(\frac{\pi}{3n}\right)^{\frac{2}{3}} \qquad \text{Equation 2-3}$$

where $\mathrm{k_B}$ is the Boltzmann constant, e is the elementary charge, h is the Planck constant, m^* is the carrier effective mass, T is the temperature, and n is the carrier density.

Therefore, the Seebeck coefficient could be enhanced by 1) increasing the carrier effective mass m^*, or 2) reducing carrier density n. However, both methods will also decrease electrical conductivity.

The Seebeck coefficient could also be expressed in another form, which is related to the Fermi Level. This is particularly useful when the nanostructuring is discussed in the following Section 2.1.4.2.

$$\mathrm{S} = \frac{1}{e}\left(\frac{\overline{E} - E_f}{T}\right) \qquad \text{Equation 2-4}$$

where e is the elementary charge, $\overline{E}$ is the average charge carrier energy, E_f is the Fermi energy, and T is the temperature.

2.1.3. Thermal Conductivity

The thermal conductivity κ is made up of two parts: the lattice thermal conductivity κ_L and the electronic thermal conductivity κ_e, as shown in Equation 2-5.

$$\kappa = \kappa_\mathrm{L} + \kappa_\mathrm{e} \qquad \text{Equation 2-5}$$

Wiedemann-Franz Law reveals the linear relation between the electronic thermal conductivity κ_e and electrical conductivity, as shown in Equation 2-6.

$$\frac{\kappa_\mathrm{e}}{\sigma} = LT \qquad \text{Equation 2-6}$$

where L is the Lorenz number, and T is the temperature.

The lattice thermal conductivity κ_L can be calculated as:

$$\kappa_\mathrm{L} = \frac{1}{3}Cvl \qquad \text{Equation 2-7}$$

where C is the heat capacity at a constant volume, v is the velocity of the phonons, and l is the phonon mean free path.

Therefore, the electronic thermal conductivity κ_e is always proportional to the electrical conductivity and has no contribution to the improvement of the figure of merit. The lattice thermal conductivity κ_L can be reduced by decreasing the phonon mean free path. This is usually realized via increasing the phonon scattering by doping or defects [52–54]. However, this method will also reduce electrical conductivity.

2.1.4. Optimization Approaches for a High Figure of Merit

As discussed in previous sections, a thermoelectric with a high figure of merit should have high electrical conductivity, high Seebeck coefficient, and low thermal conductivity. However, the three physical properties are correlated with each other and are unable to be enhanced at the same time. Therefore, it is important to balance these properties for the best figure of merit. Two common approaches for improving the performance of Si-Ge thermoelectric materials are discussed in the following sections [55].

2.1.4.1. Carrier Concentration Optimization

Generally, when carrier concentration increases, the thermal conductivity and electrical conductivity will also increase, while the Seebeck coefficient will decrease, as shown in Figure 2.1 (left). The figure of merit will reach the peak value when the carrier concentration is optimized. Figure 2.1 (right) shows the theoretical model of the figure of merit for $Si_{80}Ge_{20}$ and its variation with carrier concentration at different temperatures. The best carrier concentration of n-doped $Si_{80}Ge_{20}$ should be in the $10^{20}\ cm^{-3}$ range.

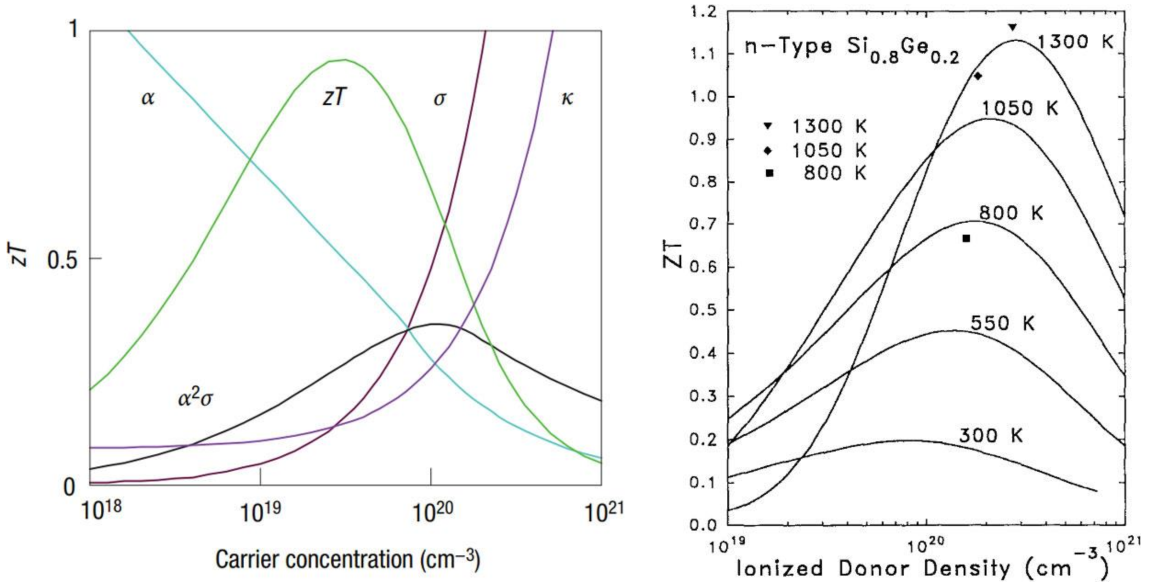

Figure 2.1. (left) The general trend of Seebeck coefficient α, electrical conductivity σ, thermal conductivity κ, power factor $\alpha^2\sigma$, and figure of merit zT variation with carrier concentration. (right) The figure of merit for $Si_{80}Ge_{20}$ and its variation with carrier concentration at different temperatures. Image reprinted from [56] and [57].

2.1.4.2. Nanostructuring

In thermoelectrics, the concept of nanostructuring is to create more grain boundaries by reducing the grain size to the nanoscale, which is close to the mean free path of phonons [52, 58, 59]. The increased phonon scattering could reduce the thermal conductivity via grain boundary scattering while maintaining high electrical conductivity. MIT and Boston University groups used ball-milled nanoparticles followed by a dc hot press to fabricate the p- and n- type silicon germanium bulk alloy [24, 25, 60]. The thermal conductivity was significantly reduced to $\sim 2.5\ \mathrm{W/m \cdot K}$, and the figure of merit was enhanced.

Figure 2.2 shows a TEM image of a nanostructured n-doped $Si_{80}Ge_{20}$ bulk alloy. The grain size is 10-20 nm, which is comparable to the electron de Broglie wavelength of 5-10 nm, much larger than the electron mean free path of 2-5 nm, and smaller than the phonon mean free path

[61]. Therefore, the thermal conductivity is reduced by the nanostructuring via phonon scattering at grain boundaries.

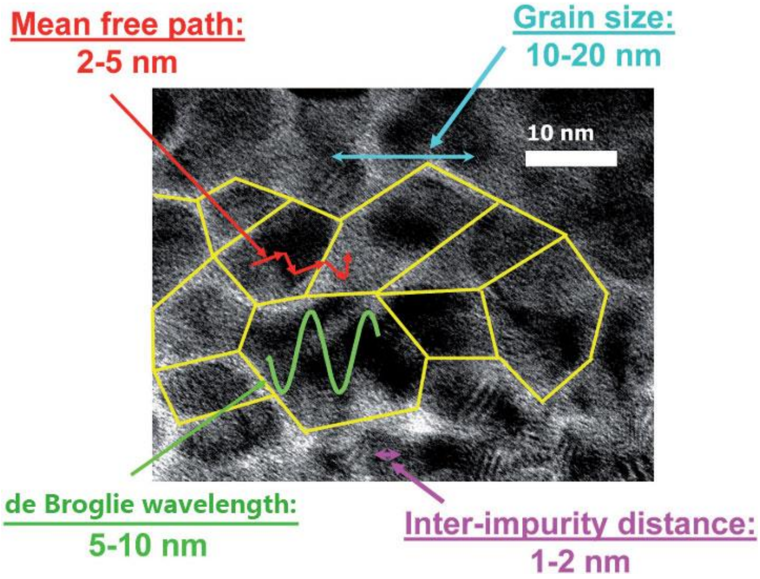

Figure 2.2. A TEM image of nanostructured n-doped $Si_{80}Ge_{20}$ bulk alloy with important numerically calculated results. Image adapted from [8].

Nanostructuring also improves the Seebeck coefficient due to the energy filtering effect [62–64]. From Equation 2-4, it is noted that the Seebeck coefficient is related to the average charge carrier energy. The low energy electrons will be filtered out at grain boundaries so that only high-energy electrons contribute to conduction, as shown in Figure 2.3. Thus the average charge carrier energy is increased by the energy filtering effect, as well as the Seebeck coefficient [65]. In nanostructured thermoelectric materials, there are more vastly grain boundaries than conventional materials. Therefore, the Seebeck coefficient is expected to be improved by nanostructure via the energy filtering effect.

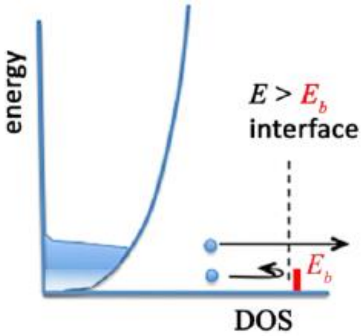

Figure 2.3. Energy filtering effect. Image adapted from [66].

2.2. Physics of thermoelectric devices

For a thermoelectric device with N pairs of unicouples, design theory was demonstrated by Min and Rowe in 1996 [67]. Two of the key conclusions related to this work are summarized below:

1) The maximum power $\mathrm{P_{max}}$ occurs when the load resistance is equal to the internal resistance $\mathrm{R_{int}}$. The max power is:

$$\mathrm{P_{max}} = \frac{\mathrm{V_{oc}^2}}{4\mathrm{R_{int}}} \qquad \text{Equation 2-8}$$

where $\mathrm{V_{oc}}$ is the open-circuit voltage, and $\mathrm{R_{int}}$ is the internal resistance.

2) The optimization of the thermoelement length is based on the design requirement, as shown in Figure 2.4. If the power output per unit area is more important, e.g., in a wearable device or in a limited space, the thermoelement length is shorter. On the other hand, if the conversion efficiency is more important, e.g., in larger area applications, a longer thermoelement length could provide better efficiency.

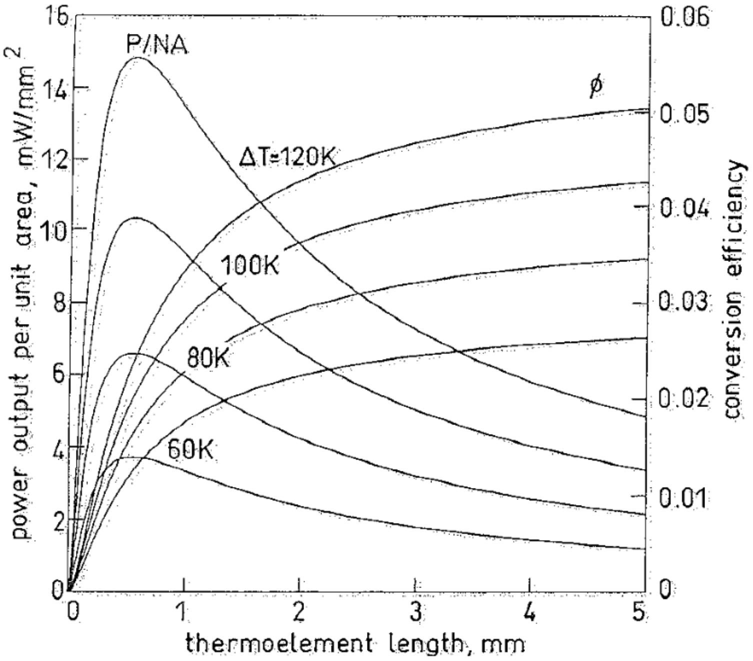

Figure 2.4. Power output per unit area and conversion efficiency as a function of thermoelement length. P/NA is the power output per unit area, where N is the number of legs, and A is the intersectional area of each leg. Image reprinted from [67].

In space missions, specific power is another important factor that needs to be considered. The specific power is used to characterize the output power generated by per unit mass (watt per kilogram). In addition to the design theory mentioned by Min and Rowe, practical design involves more aspects to be considered, such as the mass of RTG frames, thermal insulation, cooling fins, etc. The structural mass should be added to the total weight when the performance of the thermoelectric device is evaluated.

2.3. Si-Ge as a Thermoelectric Material

As discussed in Section 1.1.2, Si-Ge is the most promising high-temperature thermoelectric material due to the high working temperature and high figure of merit at temperatures above 873 K. Si-Ge could also be easily doped with phosphorus (n-type) and boron (p-type). Important applications have been discussed in Section 1.1.3.

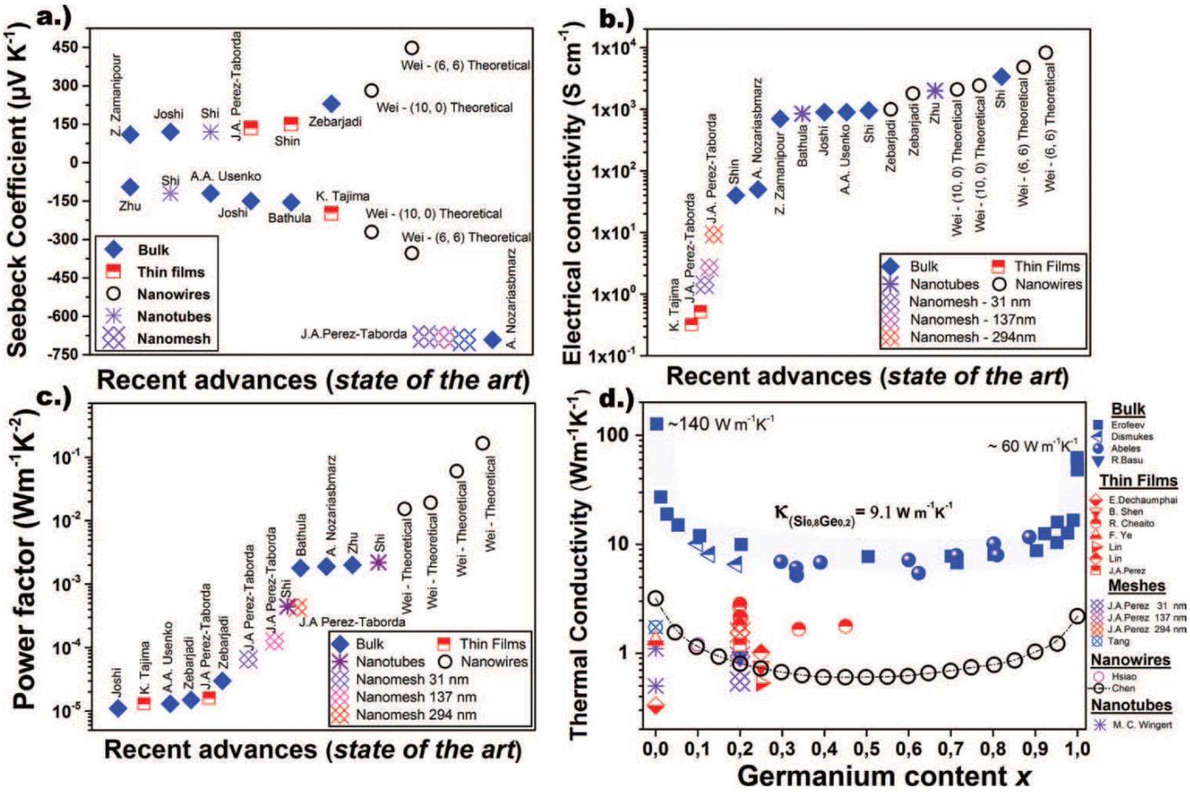

Figure 2.5. A summary of the latest reported measurement results for different structures of Si_xGe_{1-x}, (a) Seebeck coefficient, (b) electrical conductivity, and (c) power factor reported for bulk, thin films, nanomeshes, nanowires, and nanotubes. (d) The thermal conductivity for different Si_xGe_{1-x} nanostructures and bulk samples as a function of the alloy composition. Image reprinted from [12].

High-performance Si-Ge thermoelectrics were fabricated in bulk [24, 25, 68–70], thin films [71–76], nanotubes [44, 77], nanowires [78–80], and nanomeshes [81, 82]. All of these studies were related to reducing thermal conductivity via nanostructuring. A summary of the characterization results is shown in Figure 2.5. Currently, the best figure of merit was reported by a collaboration between MIT and Boston University. The figure of merit of the nanostructured bulk $Si_{80}Ge_{20}$ alloy was measured as 0.95 at 1173 K for p-type and 1.3 at 1173 K for n-type [24, 25].

The advantages of Si-Ge are summarized as follows:

1) It is a non-toxic and environmentally friendly material.
2) It can be used at a high temperature with excellent stability.
3) It is more abundant when compared with other commonly used thermoelectric materials [83], as shown in Table 1.
4) It is compatible with the IC-fabrication process, which may reduce the difficulty of commercialization.

Table 1. The abundance of elements in Earth's crust

	Si	Ge	Bi	Te	Sn	Pb	Se
ppm[1]	282,000	1.5	0.0085	0.001	2.3	14	0.05

1. The unit is parts per million (ppm) by mass (10,000 ppm = 1%).

2.3.1.1. Si-Ge Bulk Alloy

Si-Ge bulk alloy maintains the best figure of merit among all types of Si-Ge thermoelectric materials. The advantage of bulk Si-Ge is the high electrical conductivity and easy fabrication methods, such as spark plasma sintering [54], dc hot press [84], and zone melting [69]. However, the long processing time of Si-Ge bulk alloy also brings with it a long grain-growth time, which leads to a relatively large thermal conductivity. The lowest thermal conductivity is about $\sim 2.5\ \mathrm{W/m \cdot K}$ [24]. Most bulk Si-Ge alloys have a thermal conductivity of $\sim 9\ \mathrm{W/m \cdot K}$ [85, 86].

2.3.1.2. Si-Ge thin films

Si-Ge thin films usually have very low thermal conductivity, mostly close to the amorphous limit at $\sim 1\ \mathrm{W/m \cdot K}$. However, the electrical conductivity is the lowest among all types of Si-Ge, as shown in Figure 2.5 (b). The electrical conductivities of Si-Ge thin films are one to two orders of magnitude lower than their bulk counterparts [87]. This disadvantage leads to a low power factor as well as a low figure of merit.

2.3.1.3. Si-Ge nanotubes, nanowires, and nanomeshes

Si-Ge nanotubes, nanowires, and nanomeshes have excellent properties in some respects. For example, Si-Ge nanotubes have outstanding electrical conductivity, which is even higher than bulk Si-Ge. The thermal conductivity is lower than the thin-film Si-Ge and the amorphous limit. However, the Seebeck coefficients of Si-Ge nanotubes are not high. Si-Ge nanomeshes also have low thermal conductivities, which are lower than thin-film Si-Ge. The Seebeck coefficients of Si-Ge nanomeshes are much higher than any other forms. This may be attributed to the porous structure and the energy filtering effect [88]. The electrical conductivity is between that of thin-film Si-Ge and bulk Si-Ge. However, Si-Ge nanotubes, nanowires, and nanomeshes have two common disadvantages. 1) It is very difficult to measure the high-temperature performance. The samples usually have a very small size, which limits the temperature difference that can be applied to the sample. 2) The fabrication usually involves high cost and low-efficiency facilities. It is unlikely to be commercialized due to the low throughput.

2.4. Critical Parameters in Laser Processing

Laser parameters need to be optimized for the best processing result. The laser light-material interaction and thermal transfer during processing will be affected by the laser wavelength, peak power, average power, pulse energy, pulse width, repetition rate, and beam size. Each parameter will be discussed in the following sections.

2.4.1. Wavelength and Beam Size

The wavelength of the laser is the most important parameter. Because the absorption coefficient depends on the material and the laser wavelength. For example, the absorption spectrum of Si, Ge, and Si_xGe_{1-x} are shown in Figure 2.6.

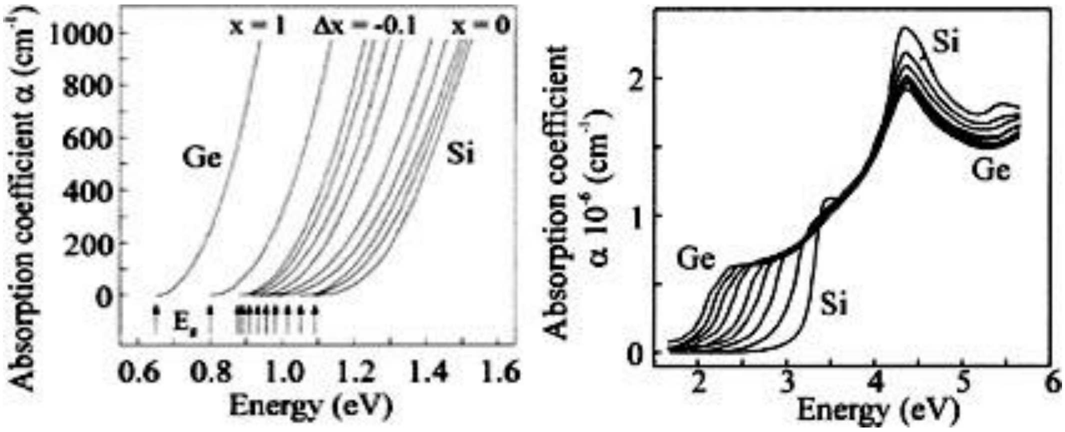

Figure 2.6. (left) The absorption spectrum of Si, Ge, and Si_xGe_{1-x} vs. energy range between 0.5 and 1.4 eV with x varying by increments of 0.1 between Ge (x = 1) and Si (x = 0). (right) The absorption coefficient of Si, Ge, and Si_xGe_{1-x} vs. energy range between 1.5 and 5.5 eV for different compositions. Lines correspond (left to right) to composition values of x = 1 (Ge), 0.915, 0.831, 0.75, 0.635, 0.513, 0.389, 0.218, 0 (Si). Image adapted from [89] and [90].

The selection of the absorption coefficient depends on the processing requirement. In laser-additive manufacturing, a high absorption coefficient is desired since the target material should efficiently interact with the laser light, which leads to an increased manufacturing throughput;

However, in laser sintering, the absorption coefficient should not be too high because a large penetration depth of the laser light could ensure homogeneity throughout the whole depth of the film.

The laser wavelength is also related to the minimum spot size of the laser due to the diffraction limit. The beam waist w_0, or the smallest radius of the beam spot, is calculated:

$$\mathrm{w}_0 = \frac{4\lambda}{\pi} \cdot \frac{f}{d} \qquad \text{Equation 2-9}$$

where λ is the wavelength, f is the focal length of the lens, and d is the diameter of the beam prior to the lens.

Therefore, for laser processing that requires micro/nano-scale resolution, a short wavelength laser is preferred.

2.4.2. Peak/Average Power, Pulse Energy, Pulse Width, and Repetition Rate

The laser used in this work is a quasi-continuous wave ytterbium fiber laser manufactured by IPG Photonics. The model number is YLR-150/1500-QCW-AC. It has two modes, the continuous-wave mode and the long-pulse mode. The product information is summarized in Table 2.

Table 2. Optical characteristics of the fiber laser.

N	Characteristics	Test conditions	Symbol	Min.	Typ.	Max.	Unit
1	Operation Mode			Pulsed / CW			
2	Polarization			Random			
3	Maximal Average Power	Pulsed mode CW mode	$P_{average}$ P_{CW}	150 250			W
4	Maximal Peak Power	Pulsed mode	P_{peak}	1500			W
5	Duty Cycle	Pulsed mode	DC			50*	%
6	Pulse Duration	Pulsed mode	τ	0.2		50**	ms
7	Maximal Pulse Energy	Pulsed mode	E_{max}	15			J
8	Emission Wavelength		λ		1070		nm
9	Emission Linewidth	Pulsed mode, max. output power	$\Delta\lambda$		5	6	nm
10	Long-term Power Instability	Time interval: 4 hrs T= const, max. output power CW & Pulsed modes			± 0.5	± 1	%
11	Red Guide Laser Power			0.1		1.0	mW

* Maximum duty cycle limit is inversely proportional to peak power: 10% for 1500W, 15% for 1000W, ..., 50% for 300W and lower.

** Maximum pulse duration limit is inversely proportional to peak power: 10ms for 1500W, 15ms for 1000W, ..., 50ms for 300W and lower.

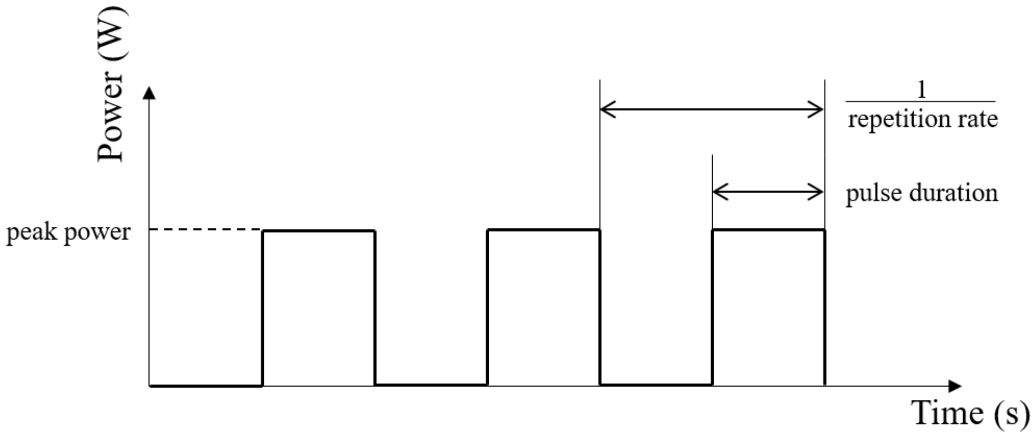

Figure 2.7. Demonstration of critical laser parameters

The meaning of each parameter is indicated in Figure 2.7. The relations among peak power P_{peak}, average power P_{avg}, pulse energy E_{max}, pulse width (pulse duration) τ, duty cycle DC, and repetition rate f could be determined by the following equations

$$P_{\text{avg}} = P_{\text{peak}} \cdot DC \qquad \text{Equation 2-10}$$

$$DC = f \cdot \tau \qquad \text{Equation 2-11}$$

$$E_{\text{max}} = P_{\text{peak}} \cdot \tau \qquad \text{Equation 2-12}$$

The selection of these laser parameters should be based on the processing requirement. For laser ablation and laser carving, high pulse energy is needed for the laser-induced breakdown. Therefore, high peak power and short pulse width are preferred. In order to minimize thermal effects, the pulse width should be less than one nanosecond. For laser sintering, the average power needs to be optimized by adjusting the pulse width and repetition rate. In this work, grain growth needs to be limited due to the requirement of nanostructuring. Therefore, the pulse width should not be too large. However, if the pulse width is too small, the laser-induced processing temperature will not be sufficient for dopant activation.

Chapter 3. Laser Sintering of Si/Ge Nanoparticles to Form $Si_{80}Ge_{20}$

This chapter contains part of manuscripts published as:

1) Xie K, Mork K, Held JT, Mkhoyan KA, Kortshagen U, Gupta MC (2018) Quasi continuous wave laser sintering of Si-Ge nanoparticles for thermoelectrics. *Journal of Applied Physics*, 123(9):094301.
2) Xie K, Mork K, Kortshagen U, Gupta MC (2019) High temperature thermoelectric properties of laser sintered thin films of phosphorous-doped silicon-germanium nanoparticles. *AIP Advances*, 9(1):015227.

This chapter contains part of a manuscript under review:

3) Xie K, Gupta MC (2019) Thermoelectric Properties of SiGe Thin Films Prepared by Laser Sintering of Nanograin Powders. *Submitted.*

3.1. Laser Sintering of Si/Ge Nanoparticles Prepared by Plasma Synthesis

3.1.1. Introduction and Motivation

One of the major problems with current thermoelectric systems is the low conversion efficiency. The efficiency of thermoelectric materials is quantified by the figure of merit, ZT. In order to achieve a high ZT, materials must have a high Seebeck coefficient, high electrical conductivity, and low thermal conductivity. In recent years, studies have shown that nanocrystalline materials can have a better figure of merits than their bulk counterparts [58]. In nanocrystalline materials, phonon scattering is enhanced at grain interfaces, thus reducing the part of the thermal conductivity contributed by phonons κ_p [53]. The overall thermal conductivity may be reduced without significantly affecting the electrical conductivity, which would enhance the figure of merit.

Previous work by NASA found a ZT = 0.7 at 650 ℃ in bulk $Si_{80}Ge_{20}$ with grain sizes on the order of 1-10 μm [30]; while an MIT research group, using bulk $Si_{80}Ge_{20}$ material with a 20 nm grain size, found a ZT = 0.75 at 650 ℃ for p-type (maximum ZT = 0.95 at 900 ℃) [25], and a ZT = 1.05 at 650 ℃ for n-type (maximum ZT = 1.3 at 900 ℃) [24], which are the highest recorded $Si_{80}Ge_{20}$ figure of merits at a high temperature. Field-Assisted-Sintering-Technique (FAST) was used to make bulk materials with nano-grain structures in both studies.

However, high cost and low yield rates are the major problems for the FAST method. Other synthesis methods are needed to fabricate nano-grain thermoelectric materials. Lasers have been proven to be a successful tool for large scale manufacturing [10], because of their low cost, high efficiency, high throughput, and easy operation. In renewable energy applications, laser processing was reported to perform laser doping [42], laser transferring [43], and laser texturing [44].

In this work, thin films were made of plasma synthesized $Si_{80}Ge_{20}$ nanoparticles doped with phosphorous and sintered by a long-pulsed infrared laser. The motivation of this chapter is to demonstrate that laser sintered $Si_{80}Ge_{20}$ thin films with nano grain size have high electrical conductivity and low thermal conductivity, which could be used as a fast, low cost, and easy method for thermoelectric thin-film fabrication.

3.1.2. Experimental Details

The $Si_{80}Ge_{20}$ NPs were synthesized in a nonthermal, low pressure, capacitively coupled plasma tube reactor, as shown in Figure 3.1 [91]. SiH_4 and GeH_4 (diluted 10% in Ar) were used as the precursor gas. PH_3 (15% diluted in H_2) was added to the precursor gas as the dopant source. The precursor gases were simultaneously decomposed in the plasma, producing alloyed $Si_{80}Ge_{20}$ NCs. The $Si_{80}Ge_{20}$ NCs were accelerated through a rectangular nozzle placed downstream and deposited on to a quartz substrate. The substrate was moved by a pushrod to obtain a large-area thin film deposition.

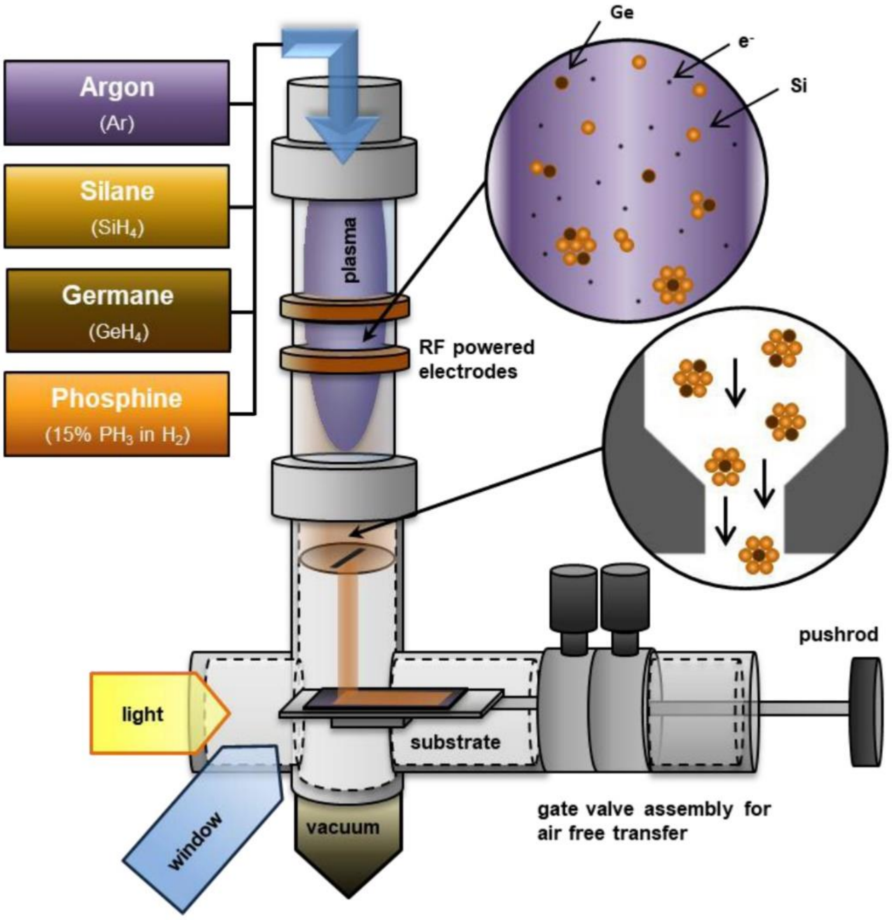

Figure 3.1. Diagram of a non-thermal, capacitively coupled plasma reactor setup. Figure courtesy of Kelsey Mork.

The as-deposited $Si_{80}Ge_{20}$ films were sintered by a QCW laser (IPG photonics YLR-150/1500-QCW-AC) with a 1070 nm wavelength, having a Gaussian profile and pulse duration of 0.1 ms. The peak power of the laser was 1500 W at a 100% set point, and the PRR was between 100 Hz and 1000 Hz, depending on the experiment. For long pulse lasers, both the peak power and the average power are important. The heating effect of the laser was varied by the laser peak power, PRR, pulse width, spot size, and sample scanning speed. The beam was first reflected by a mirror before passing through a lens with a focal point 3 cm above the sample. This focal point was chosen to decrease the laser intensity at the surface of the sample and increase the area covered by beam scanning. The sample chamber was mounted beneath the beam on a computer-controlled x-y stage, allowing for a smooth raster scan of the sample. The sample was covered with a quartz slide to reduce dopant and film loss. The chamber was pumped down to 10^{-2} Torr before being purged with argon gas. Low flow argon gas was then maintained throughout the sintering process to reduce oxidation of the sample. A schematic diagram of the experimental setup is shown in Figure 3.2.

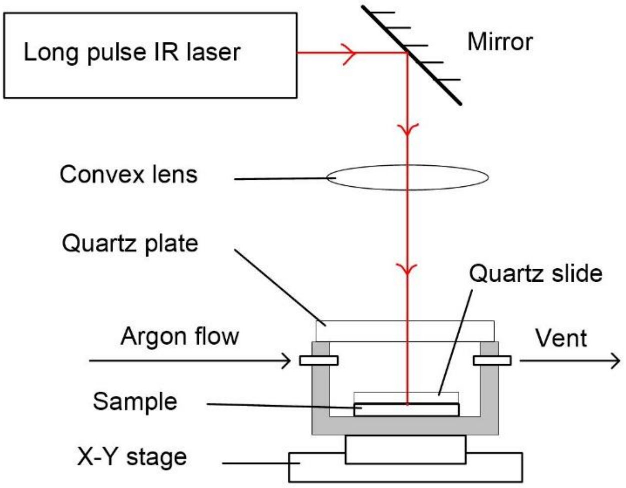

Figure 3.2. Schematic diagram of the experimental setup used to laser sinter $Si_{80}Ge_{20}$ thin films.

3.2. Laser Sintering of Si/Ge Nanoparticles Prepared by Ball Milling

3.2.1. Introduction and Motivation

In this section, plasma synthesis and laser sintering are used as a novel $Si_{80}Ge_{20}$ thin film synthesis method, which may potentially be applied for mass production [50, 92]. The plasma-synthesized laser-sintered (PSLS) $Si_{80}Ge_{20}$ thin films showed a figure of merit of 0.6 at 873 K [93]. This is comparable with the bulk nanostructured n-type $Si_{80}Ge_{20}$ materials reported by Wang et al. in 2008 with a figure of merit of ~1 at 873 K [24]. Although the laser sintering process discussed in Chapter Chapter 3 has many advantages such as no vacuum requirement, fast process speed, adaptability with the "printing" process, etc. The preparation of the as-deposited films still involves plasma synthesis, which has vacuum requirements and relatively high cost. Moreover, plasma synthesis is not able to be integrated with the laser sintering process in an assembly line. Also, it was hard to activate the dopants in the plasma synthesized nanoparticles. This may also limit its application in mass production .

In this section, a new film preparation method is discussed, and the laser sintering method is improved. Ball milling and suspension coating methods are used to prepare the film. The improved laser sintering method can provide faster processing in comparison to the method reported in Chapter Chapter 3 [93, 94]. The electrical conductivity, Seebeck coefficient, and thermal conductivity of the n-type $Si_{80}Ge_{20}$ thin films sintered with different laser power were measured or estimated up to 873 K and compared with other reported $Si_{80}Ge_{20}$ thin films, bulk nanostructured $Si_{80}Ge_{20}$, and the $Si_{80}Ge_{20}$ material used in (RTGs). The motivation of this chapter is to demonstrate that low-cost nanograin $Si_{80}Ge_{20}$ thin films prepared by ball milling and the laser sintering process have a comparable thermoelectric figure of merit to other $Si_{80}Ge_{20}$ thermoelectric materials. The performance can be further improved at a higher operating temperature.

3.2.2. Experimental Details

The Si powders (99.999%, Sigma Aldrich), Ge powders (99.999%, Sigma Aldrich), and P chunks (99.99%, Sigma Aldrich) were mixed and crushed with a pestle in a stainless-steel mortar. The nominal composition of the ball milling powder was $Si_{80}Ge_{20}$ + 2% Phosphorous. The mixed powders were wet ball-milled with isopropyl alcohol (IPA) in Restch PM200 at 400 RPM for 3 hours. Then the nanopowder paste was diluted with methanol and preserved in a sealed glass bottle to prevent oxidation. It was ultrasonicated for 15 min to get uniformly dispersed suspension before use.

The nanopowder suspension was spin-coated on the quartz substrate. The thickness can be adjusted by the amount of suspension applied. After soft baking at 80 ℃ for 3 min, the samples were stored in a vacuum chamber for more than 24 hours to prevent oxidation and evaporate the residual organic solvent.

The as-deposited $Si_{80}Ge_{20}$ thin films were sintered with a QCW near-infrared laser of wavelength 1070 nm laser (IPG photonics YLR-150/1500-QCW-AC). The laser sintering was performed at the pulse repetition rate (PRR) at 1000 Hz, the pulse width at 0.1 ms, and scanning speed at 40 mm/s. The peak power of the laser was 1500W at a 100% set point. The samples were sintered with different laser power from 20% to 40%. The laser beam was controlled by a Galvo to perform the raster scan. The sample was covered with a quartz slide and placed about 1 cm above the focal point. This working distance was chosen to decrease the laser intensity at the surface of the sample and to increase in the area covered by laser beam scanning. The chamber was purged with argon gas; then, the argon flow was maintained throughout the sintering process to reduce the oxidation of the sample. A schematic diagram of this experimental setup is shown in Figure 3.3.

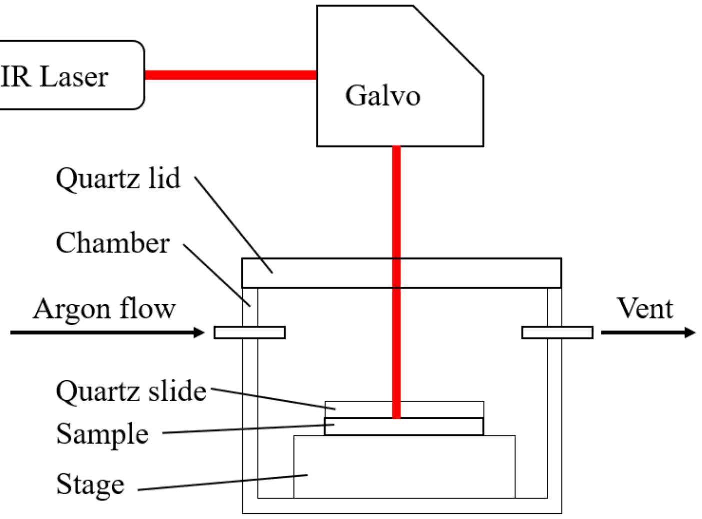

Figure 3.3. Schematic diagram of the experimental setup of laser sintering.

Chapter 4. Characterization Methods of Thermoelectric Thin Films

This chapter contains part of manuscripts published as:

1) Xie K, Mork K, Held JT, Mkhoyan KA, Kortshagen U, Gupta MC (2018) Quasi continuous wave laser sintering of Si-Ge nanoparticles for thermoelectrics. *Journal of Applied Physics*, 123(9):094301.
2) Xie K, Mork K, Kortshagen U, Gupta MC (2019) High temperature thermoelectric properties of laser sintered thin films of phosphorous-doped silicon-germanium nanoparticles. *AIP Advances*, 9(1):015227.

4.1. Surface Morphology using SEM

The surface morphology of the samples was observed using SEM (FEI Quanta 650 Scanning Electron Microscope). The SEM images provide a better understanding of the sintering quality, such as percolation structure, balling structure, grain growth, and densification.

4.2. Composition using EDS

The composition of the $Si_{80}Ge_{20}$ thin films was confirmed by EDS. EDS mapping was used to determine the element distribution and the Si to Ge ratio. However, the dopant concentration after sintering could not be determined by EDS due to the sensitivity limitations.

4.3. Crystallization and Grain Size using XRD

The crystallization and the grain size were determined by XRD. The XRD spectra analysis was done using the MAUD program developed by Lutterotti et al. [95]. The composition of the thin films was confirmed by the peak position analysis result of MAUD. Peak broadening of diffraction peaks permits quantitative size analysis of the grain utilizing the Williamson–Hall method.

4.4. Seebeck Coefficient and Electrical Conductivity using Modified Four-Point Probe Method

Seebeck coefficient and electrical conductivity were measured using the developed experimental setup, as shown in Figure 4.1. The electrical probes used in the method are similar to those proposed by Iwanaga *et al*. [96]. A Nickel-Chromium wire and a Nickel-Alumel wire worked as a type K thermocouple. Additionally, the Nickel-Chromium wires were simultaneously used to measure the thermal voltage. This design ensures the temperature is measured at the same location where the thermal voltage is measured, which is especially important for thin films. A large probe may work as a heat sink, resulting in mismatching of the temperature and voltage measurements.

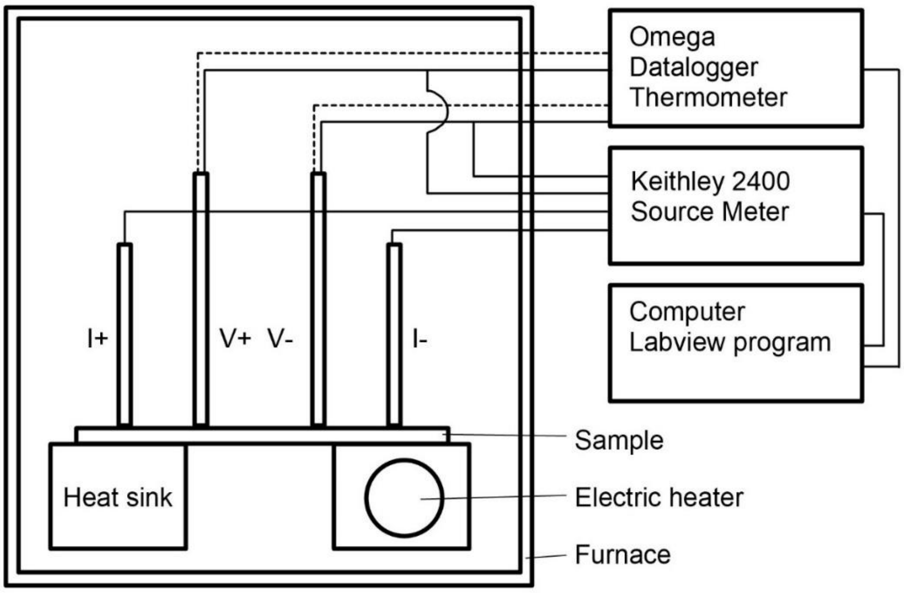

Figure 4.1. Seebeck coefficient and electrical conductivity measurement setup. The solid lines are nickel-chromium wires, while the dash lines are nickel-alumel wires.

When the Seebeck coefficient is measured, only the V+ probe and V- probe are used. The furnace is used to create desired ambient temperature, while the electric heater and heat sink are used to create different temperature gradients. The temperatures of the V+ probe (cold side) and the V- probe (hot side) and the Seebeck voltage readings were recorded by the LabVIEW program simultaneously.

When the electrical conductivity is measured, all 4 probes are used. The temperature is controlled by the furnace, while the electric heater is shut down. When the temperature readings of the V+ probe and the V- probe are equal and stable, the current provided by the source meter is applied to the I+ probe and the I- probe. Then the voltage and temperature readings are recorded by the LabVIEW program. Each measurement includes one heating and one cooling process, similarly to the Seebeck coefficient measurement.

4.5. Carrier Mobility using Hall Effect Measurement

Carrier mobility and concentration were measured by an Ecopia HMS-3000 Hall Measurement System. The sintered thin films were cut into a square shape as required by the Van der Pauw method. The contacts were made by applying silver pastes at the four corners of the sample in the Van der Pauw pattern.

4.6. Out-of-plane Thermal Conductivity using the 3ω-Method

The out-of-plane thermal conductivity of the thin films was determined using the experimental setup developed based on the 3ω-method [97–100], as shown in Figure 4.2. There are several difficulties in measuring thermal conductivity at a high temperature. 1) For thermoelectric or semiconductor thin films, a silica thin film is used as an insulating layer for the 3ω-method. However, the laser-sintered films are rough and porous, making it difficult to deposit a well-insulated SiO_2 layer using CVD [101]. 2) SU-8 was used as the insulating layer to measure the thermal conductivity of the $Si_{80}Ge_{20}$ film under room temperature [94]. However, the maximum temperature is limited due to the low softening point of SU-8 at 473 K. 3) The rough surface and high porosity also increased the difficulty for performing time-domain thermoreflectance (TDTR) measurements on the samples. The scattered signal from surface roughness leads to a low signal-to-noise ratio, which cannot be fit to models.

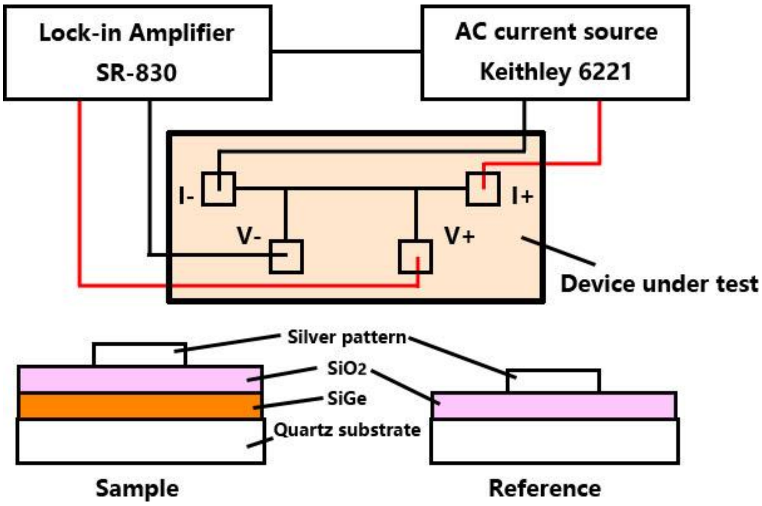

Figure 4.2. Schematic diagram of the differential 3ω-method measurement setup.

The insulating layer for 3ω-method measurement in this work is made of sol-gel SiO_2 [102, 103]. There are two key reasons for this selection. Firstly, the SiO_2 thin films should have low porosity. A denser insulating layer will have better thermal conductivity, which is preferred for the 3ω-method measurement. Secondly, the SiO_2 thin films should be able to fill the pores and valleys of the original porous film to provide a smooth surface and ensure complete electrical insulation. Then the silver heater pattern was transferred onto the sample device and the reference device by photolithography [101]. Alternating current with angular frequency ω was applied to the silver heater. The temperature rise can be described by the following:

$$\Delta T = 2\frac{dT}{dR}\mathrm{R}\frac{V_{3\omega}}{V_{1\omega}}$$

where R is the electrical resistance, RdT/dR is the reciprocal of the temperature coefficient of resistance (TCR) of the silver heater, $V_{1\omega}$ and $V_{3\omega}$ are the first and third harmonic voltage. The temperature rise in the $Si_{80}Ge_{20}$ film $\Delta \mathrm{T_f}$ can be derived as follows:

$$\Delta T_{\mathrm{f}} = \Delta T_{\mathrm{sample}} - \frac{P_{\mathrm{sample}}}{P_{\mathrm{ref}}}\Delta T_{\mathrm{ref}}$$

where ΔT_{sample} is the temperature rise in the sample device, ΔT_{ref} is the temperature rise in the reference device. Therefore, temperature rise through the $Si_{80}Ge_{20}$ film ΔT_{f} can be calculated by subtracting the ΔT_{ref} from ΔT_{sample}. P_{sample} and P_{ref} are the thermal powers applied to the sample device and to the reference device, respectively. In order to simplify the calculation and minimize the heat loss error, both thermal powers can be adjusted to the same value. Then the thermal conductivity can be derived by the following:

$$\kappa = \frac{\mathrm{P}_{\text{sample}} t_{\text{f}}}{lw\Delta T}$$

where t_{f} is the film thickness, l is the length of the heater, and w is the width of the heater.

4.7. In-plane Thermal Conductivity using Heat Spreader Method

The nanocrystalline $Si_{80}Ge_{20}$ films with a thickness of 10 µm should be thermally homogeneous materials, and thus in-plane and out-of-plane thermal conductivities were expected to be the same. Therefore, the in-plane thermal conductivity is measured to support this statement. The experiment was assisted by Prof. Mona Zebarjadi's group.

The in-plane thermal conductivity of the thin films was determined using the heat spreader method [104]. An aluminum heater was coated on top of the sample using thermal evaporation. Joule heating from the line heater created a temperature drop in the in-plane direction. The temperature distribution was recorded by a thermal infrared camera. A MatLab program was developed for data post-processing. Missing data were interpolated using the k-nearest neighbors algorithm. Then the temperature drop was curve-fitted with the $e^{-\beta x} + \mathrm{C}$ equation. The coefficient β could be used to calculate the thermal conductivity k_x.

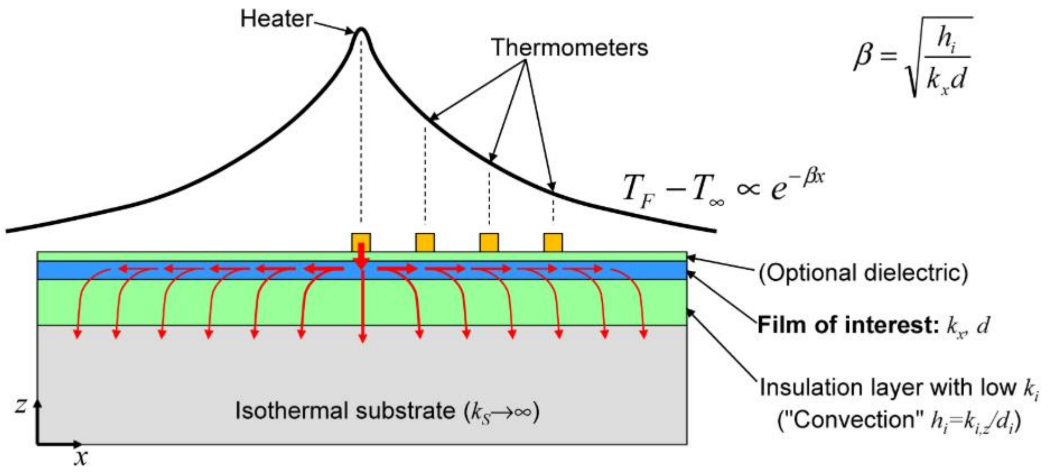

Figure 4.3. A heat spreader method to measure the in-plane thermal conductivity of a supported film. Image reprinted from [104]**.**

It is worth mentioning that the accuracy of this method is expected to be lower than the 3ω-method in $Si_{80}Ge_{20}$ thin film measurement [105]. The heat spreader method is most suitable for relatively high in-plane thermal conductivity materials according to the boundary condition described by Dames [104]. However, it is still a valuable characterization method for verification of thermal homogeneity of the $Si_{80}Ge_{20}$ films.

Chapter 5. Results and Discussions on Thermoelectric Thin Films

This chapter contains part of manuscripts published as:

1) Xie K, Mork K, Held JT, Mkhoyan KA, Kortshagen U, Gupta MC (2018) Quasi continuous wave laser sintering of Si-Ge nanoparticles for thermoelectrics. *Journal of Applied Physics*, 123(9):094301.
2) Xie K, Mork K, Kortshagen U, Gupta MC (2019) High temperature thermoelectric properties of laser sintered thin films of phosphorous-doped silicon-germanium nanoparticles. *AIP Advances*, 9(1):015227.

This chapter contains part of a manuscript under review:

3) Xie K, Gupta MC (2019) Thermoelectric Properties of SiGe Thin Films Prepared by Laser Sintering of Nanograin Powders. *Submitted.*

5.1. Thermoelectric Thin Films Prepared by Plasma Synthesis and Laser Sintering

5.1.1. Properties of Plasma-Synthesized $Si_{80}Ge_{20}$ Nanoparticles

To investigate the structure and the degree of alloying of the $Si_{80}Ge_{20}$ NP films, $Si_{80}Ge_{20}$ NCs were deposited directly onto carbon-coated copper TEM grids (thin carbon/holey support) and transferred with less than 30 seconds of air exposure into an aberration-corrected FEI Titan G2 60-300 (scanning) transmission electron microscope (STEM) equipped with a Super-EDX detector. HAADF STEM images were acquired at 200 kV (imaging only) and 60 kV (elemental mapping) with a 25 mrad convergence semi-angle and an 80 pA beam current. Spatially resolved STEM-EDX maps of individual particles were acquired with 350×350 pixels over a 15×15 nm^2 area with a pixel dwell time of 3 μs/pixel, an acquisition time of 10 min, and drift correction after every frame. The K-edges of Si, Ge, and O were background-subtracted and integrated, producing elemental maps. A three-pixel Gaussian blur was applied to the images shown in Figure 5.1 (a) to aid in visualization. The image shows spherical geometry and no obvious elemental segregation. The elemental maps of Si+Ge, Si, Ge, and O are shown in Figure 5.1 (b) and (c). The data for each element is radially averaged around the center of the particle to obtain the radial map shown in Figure 5.1 (d). It confirms a relatively uniform distribution of Si and Ge throughout the NC, as well as the presence of a thin ~1 nm oxide layer. Figure 5.1 (e) shows the image of a cluster of 8-10 nm diameter spherical NCs, which shows crystal lattice fringes and uniform alloying. These measurements were done by our collaborator at the University of Minnesota.

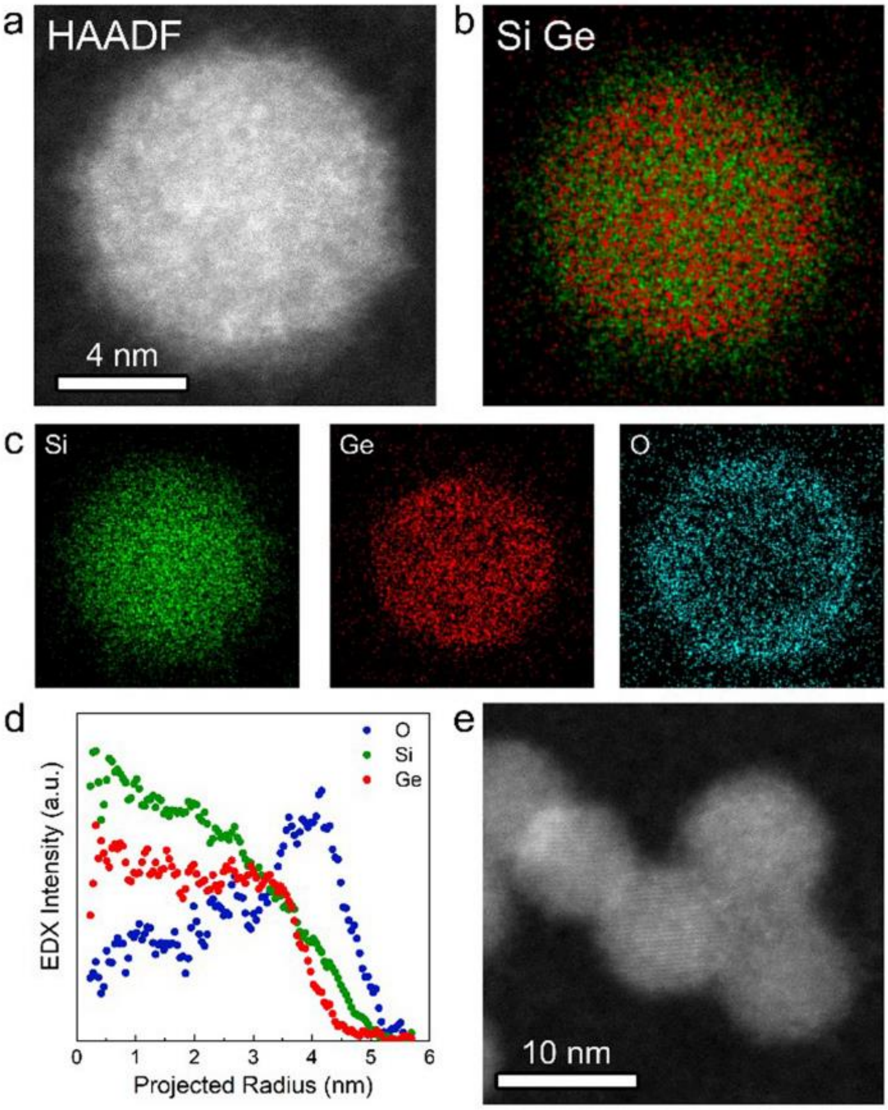

Figure 5.1. Representative STEM-EDX analysis. (a) 60 kV HAADF image of a 5% (nominal) P-doped $Si_{80}Ge_{20}$ NC. (b) Composite map of Si (green) and Ge (red). (c) Independent elemental maps of Si, Ge, and O. (d) Radially averaged EDX intensity, (e) 200kV HAADF image of a different cluster of 8-10nm diameter spherical $Si_{80}Ge_{20}$ NCs. [94]

Figure 5.2 shows the TEM image and the corresponding diffraction pattern of a larger $Si_{80}Ge_{20}$ NC cluster. The diffraction pattern confirms the polycrystalline structure. The enlarged TEM image in Figure 5.2 (left) shows that a shell that is rich in oxygen may have different structures when compared to the rest of the grain.

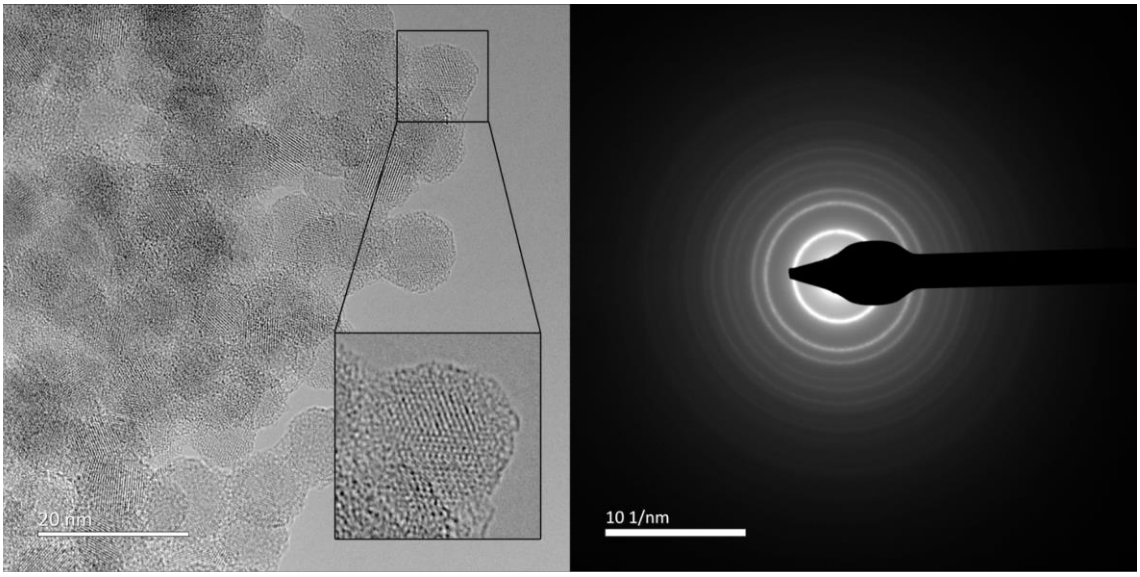

Figure 5.2. TEM image (left) and the corresponding diffraction pattern (right) of a larger $Si_{80}Ge_{20}$ NC cluster.

The nanocrystals composing the film were found to be crystalline, spherical, well alloyed, and had an average crystallite size of 8 nm with a 10-15% standard deviation. Past research on this synthesis method has found the active dopant levels in the synthesized nanoparticle films to be lower than the nominal levels with the phosphorous dopants included via lattice substitution [50].

Films were found to be between 3 and 10 microns thick, depending on the deposition time, homogeneous on the scale required for laser sintering, and extremely porous. These thicknesses are significantly larger than those of other published thin-film type thermoelectric materials [71, 76, 106–108]. Thicker films may allow for a larger temperature gradient to be obtained, thus increasing the thermovoltage output. The high porosity of the films combined with the deactivation of charge carriers during minor oxidation resulted in immeasurably low electrical conductivity of the pre-sintered films [109].

5.1.2. Sintering by Long Pulse Laser

An infrared long-pulse laser of wavelength 1070 nm was chosen for this study because it can heat a large thickness of the film, which will provide better sintering uniformity. There are two major benefits to using a long pulse laser instead of a short pulse laser. First, the thermal effect of the long-pulse laser lasts longer than the short-pulse laser, resulting in deeper heat penetration depth. Additionally, the longer thermal duration will provide better uniformity. Second, the thermal effect of the long-pulse laser works better as an annealing method and will improve the film's crystal structure.

The high energy imparted to the $Si_{80}Ge_{20}$ films by the long-pulse laser during sintering resulted in the melting of the films. During the melting and the resolidification process, the relatively lower melting temperature of the germanium caused it to transition from liquid to solid form before the solidification of silicon. This caused the germanium to segregate out of the $Si_{80}Ge_{20}$ alloy, forming balls of germanium rich material in some cases and webbing patterns of germanium rich material in other cases. This can be seen in the backscattering SEM images in Figure 5.3, where the germanium rich materials appear whiter than the silicon-rich. In addition to modifying the alloy fraction of the $Si_{80}Ge_{20}$, the temperature needed to melt the material far surpasses the melting temperature of the phosphorous dopant. The high heat could cause one of two effects; some dopants could evaporate out of the material and causing high loss of dopants. Although the quantitative result of dopant loss was difficult to measure because of the high porosity, the dopant loss was qualitatively observed by performing Energy-dispersive X-ray spectroscopy (EDS) before and after laser sintering process; alternatively, phosphorus atoms that were previously not fourfold substitutionally incorporated into the crystal lattice, could be better incorporated into the lattice structure after laser processing. This would result in an increase in electrical conductivity due to activated dopant atoms and improved conductive paths.

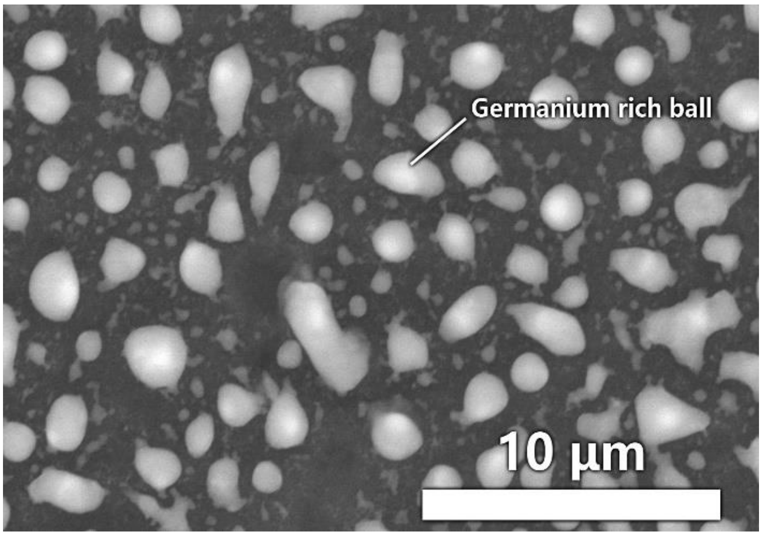

Figure 5.3. SEM, in backscatter mode, images of the balling structure. The bright part indicates a germanium rich region. The laser parameters were 225 W peak power, 300 Hz PRR, 0.1 ms pulse width, and 0.5 mm/s scanning speed.

In order to understand the processes of dopant reactivation and dopant loss, several attempts were made to measure the dopant concentration of post sintered samples. However, the porosity and rough surface of the samples makes it difficult for SIMS characterization. Meanwhile, the low concentration of phosphorus was too close to the confidence limits of EDS and XPS to get an accurate quantitative measure.

5.1.3. Laser Crystallization and Grain Size

Figure 5.4 shows the XRD spectra of the fused quartz substrate (bottom spectrum) and of the laser-sintered sample (top spectrum). The three clear peaks shown in the top spectrum confirm that the thin film is well-alloyed $Si_{80}Ge_{20}$. The broadened diffraction peaks indicate that the grain size is small. By calculating from the XRD spectra using the Williamson–Hall method, the average grain size was determined as 68 nm. The as-deposited thin film has an average grain size of 8 nm, as reported in Section 5.1.1 [94]. There is still room for improvement in grain size reduction. The peak position also confirms that the composition of Si:Ge is 80:20.

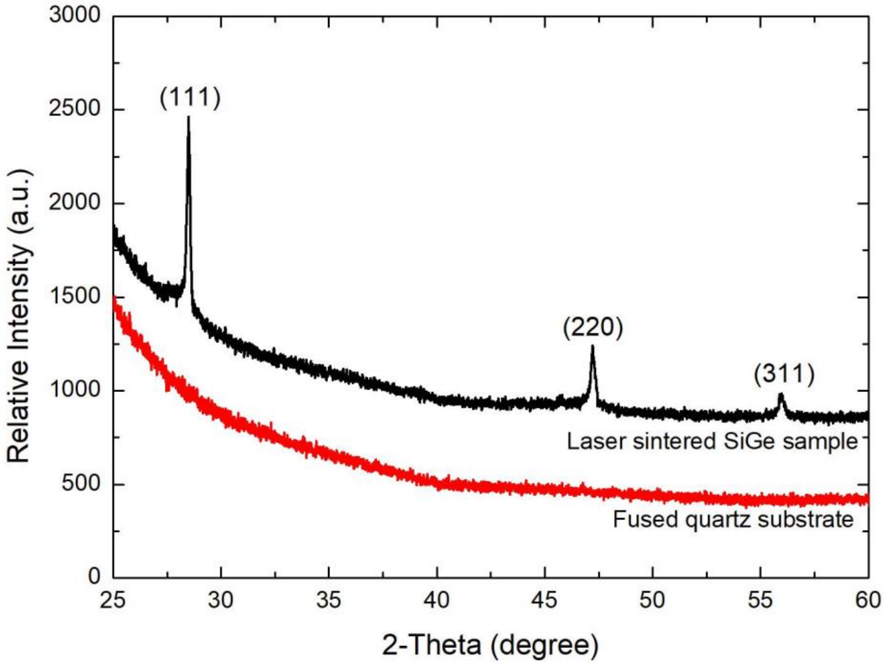

Figure 5.4. XRD patterns for the fused quartz substrate and the laser-sintered $Si_{80}Ge_{20}$ sample

5.1.4. Segregation of Germanium and Balling Structure

The laser Gaussian beam shape is good for process parameter optimization in laboratory experiments because it can sinter the film with different laser energy densities in one scan. The process of the germanium segregation can be seen in Figure 5.5 (a) to (d). The figure shows the impact of the Gaussian beam profile and surface morphology variation. It also shows different surface morphologies after sintering with different laser energy densities. All figures were taken under SEM backscatter mode. The brighter parts have a higher average atomic number, and the darker parts have a lower average atomic number. The thickness of the films was measured as 3-5 μm, which is larger than the penetration depth of SEM predicted by Kanaya-Okayama formula [110]. Therefore, brighter areas in the figure show germanium rich regions while darker areas show silicon-rich regions. Figure 5.5 (d) shows the film sintered by the peak of the Gaussian beam, where the laser energy density was the highest. The maximum sintering temperature of location (d) was higher than that of location (a), the edge of the Gaussian beam. When the temperature was relatively low, the germanium phase had a low viscosity and could only form small islands, as shown in Figure 5.5 (a). The electrical conductivity was close to zero because the islands were separated from each other, and no conductive path was formed. When the temperature became higher, there were two possibilities. If the germanium rich phases wet the substrate well, a semi-continuous percolation structure is formed. Such a structure had high electrical conductivity. This could be because of better-connected pathways and limited dopant evaporation, which will be discussed in the following sections. However, if the germanium rich phases did not wet the substrate well, the previously mentioned small islands of germanium began to merge together and formed small balls, as shown in Figure 5.5 (b). When the laser energy density was even higher, the small balls began to merge together and formed large islands, as shown in Figure 5.5 (c) and (d). Meanwhile, the high processing temperature would result in too much dopant loss. Lack of conductive path and too low dopant concentration resulted in a near-zero electrical conductivity.

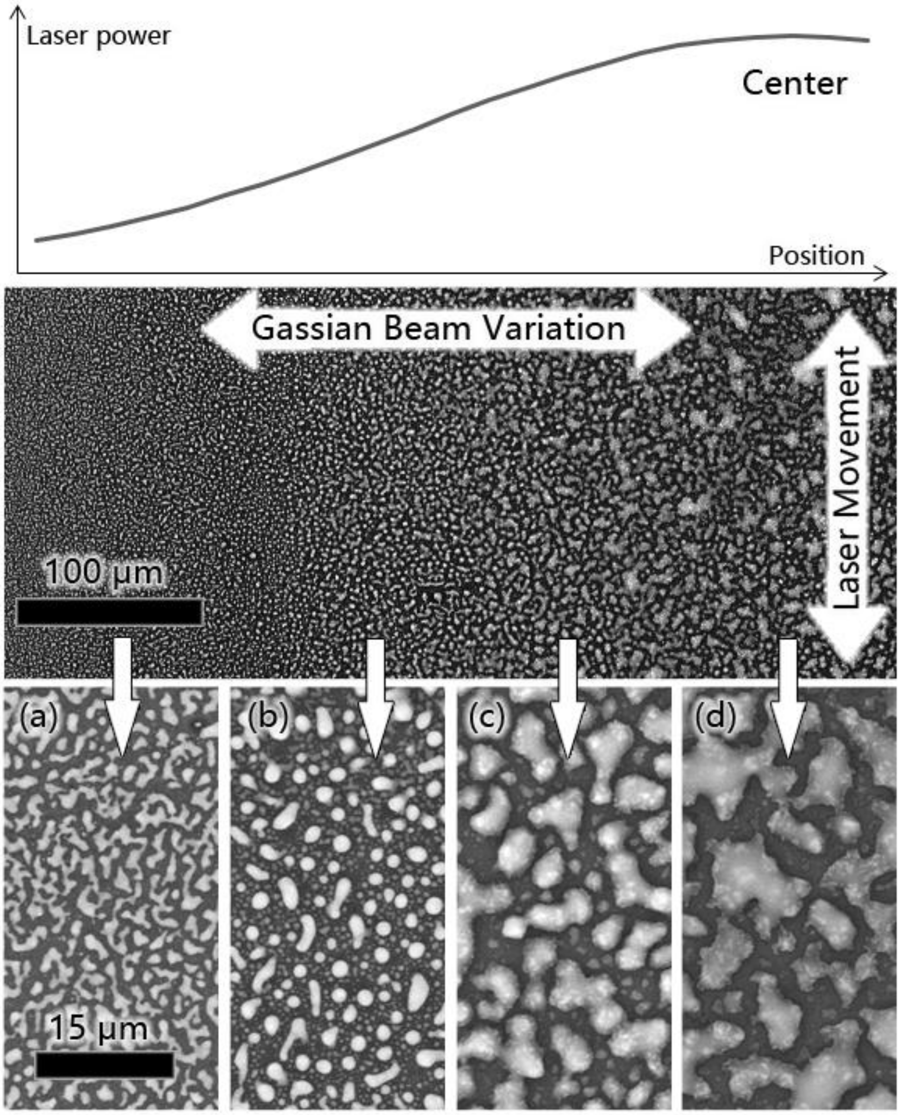

Figure 5.5. SEM, in backscatter mode, images of the surface morphology changes due to the Gaussian beam profile. Brighter areas show germanium rich regions, while darker areas show silicon-rich regions. (a) shows the films sintered by the edge of the Gaussian beam, with (b)-(c) approaching the center of the beam and (d) showing the film sintered by the center of the Gaussian beam. The incident Gaussian beam power profile is plotted at the top.

5.1.5. Surface Morphology

Certain sintering experiments resulted in the balling structure, as shown in Figure 5.3 and Figure 5.5 (b). The surface morphology shows segregation and discontinuity, resulting in an electrical conductivity too small to be measured. This could be due to a variety of factors. Poorly chosen sintering parameters or improper cleaning of the substrate surface could both cause balling. The quartz substrate was also a potential cause of this balling structure as the molten silicon-germanium did not wet the quartz well.

The percolation structure is a more desirable structure, as shown in Figure 5.6 (b). The results shown in Figure 5.6 (a) to (c) were for sintering at the same laser peak power of 225 W, the same scanning speed of 0.5 mm/s, but different PRRs (a) 200 Hz, (b) 400 Hz, and (c) 800 Hz. The corresponding tilted-view SEM images are shown on the right. The SEM images were taken using the backscattering mode that allows for some elemental analysis. The bright part is germanium-rich, while the dark part is silicon-rich. Figure 5.6 (a) and (c) have much lower electrical conductivities when compared with Figure 5.6 (b), but the mechanisms are very different. Figure 5.6 a) shows the balling structure beginning to appear because of bad substrate wetting. In Figure 5.6 (c), the surface morphology shows that the laser intensity was too high, resulting in elemental segregation and accumulations of germanium. Although the conductive regions are still interconnected, there are fewer conductive paths and are narrower than those in Figure 5.6 (b). Thus, the electrical conductivity of (c) was lower than that of (b). Figure 5.6 (b) shows the best surface morphology as well as the best electrical conductivity because of the selection of proper laser processing parameters. The nanoparticles were interconnected, and the surface was more uniform than the other two figures. The process temperature was also high enough to reactivate dopant atoms.

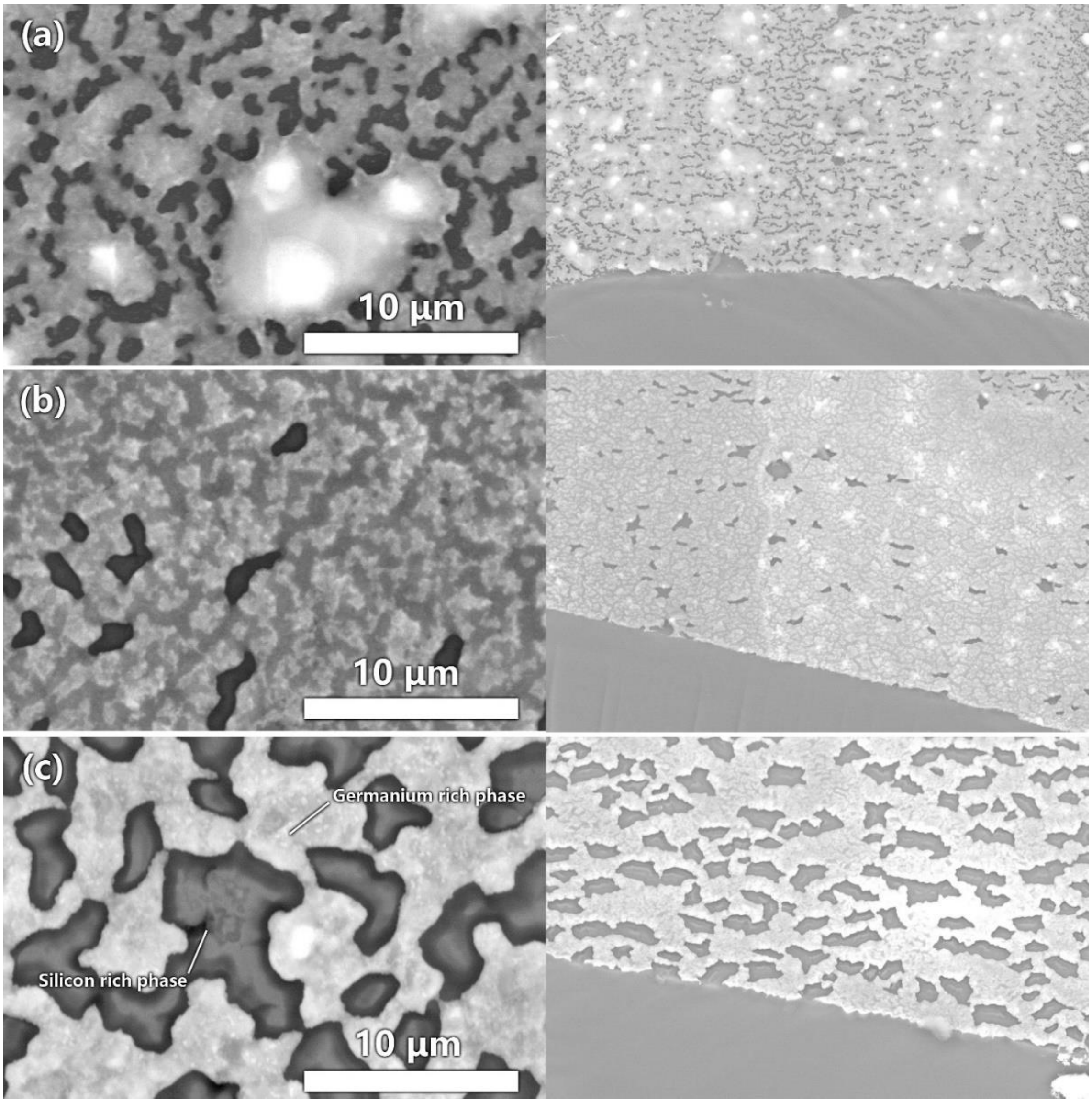

Figure 5.6. SEM, in backscatter mode, images of $Si_{80}Ge_{20}$ nanoparticles with the same laser peak power of 225 W, the same scanning speed of 0.5 mm/s, but different PRRs (a) 200 Hz, (b) 400 Hz, and (c) 800 Hz. The corresponding tilted-view SEM images are shown on the right.

5.1.6. Electrical Conductivity

The high-temperature electrical conductivity measurement results are shown in Figure 5.7. Firstly, the thin film behaves very differently than bulk materials. The electrical conductivity of thin-film type $Si_{80}Ge_{20}$ increases when the temperature is raised, while bulk nanostructured

$Si_{80}Ge_{20}$ shows a decrease in electrical conductivity. Secondly, the slopes of increasing electrical conductivity of various $Si_{80}Ge_{20}$ thin films are very similar. For our champion laser sintered thin film, the electrical conductivity increases from 22.3 S/cm at room temperature to 62.1 S/cm at 873 K, as shown in Figure 5.7. Since the figure of merit is related to the electrical conductivity via $ZT \propto \sigma$, the high electrical conductivity at higher temperatures improves the figure of merit.

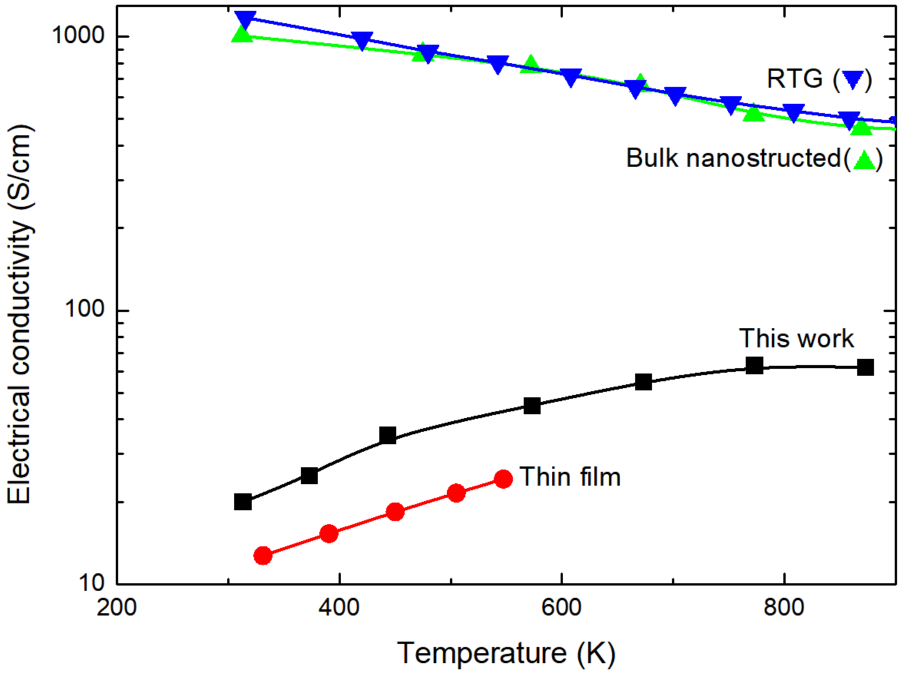

Figure 5.7. Electrical conductivity variation with temperature and comparisons with other reported thin film, bulk nanostructured, and RTG $Si_{80}Ge_{20}$ materials.

5.1.7. Thermal Conductivity

The high-temperature thermal conductivity measurement results are shown in Figure 5.8. The room- and high-temperature thermal conductivities (573 K) were measured as 1.34 $\mathrm{W/m \cdot K}$ and 1.37 $\mathrm{W/m \cdot K}$, respectively. Thus, within the measurement accuracy, the thermal conductivity remains constant in this temperature range. Wang *et al.* reported that the thermal conductivity was significantly reduced by the interfaces created by nanostructures and was not significantly affected by the measurement temperature [24]. Therefore, it is reasonable that the thermal conductivity of the thin film in this study at 873 K is similar to that at room temperature. The predicted high-temperature thermal conductivity will be used in the figure of merit estimation.

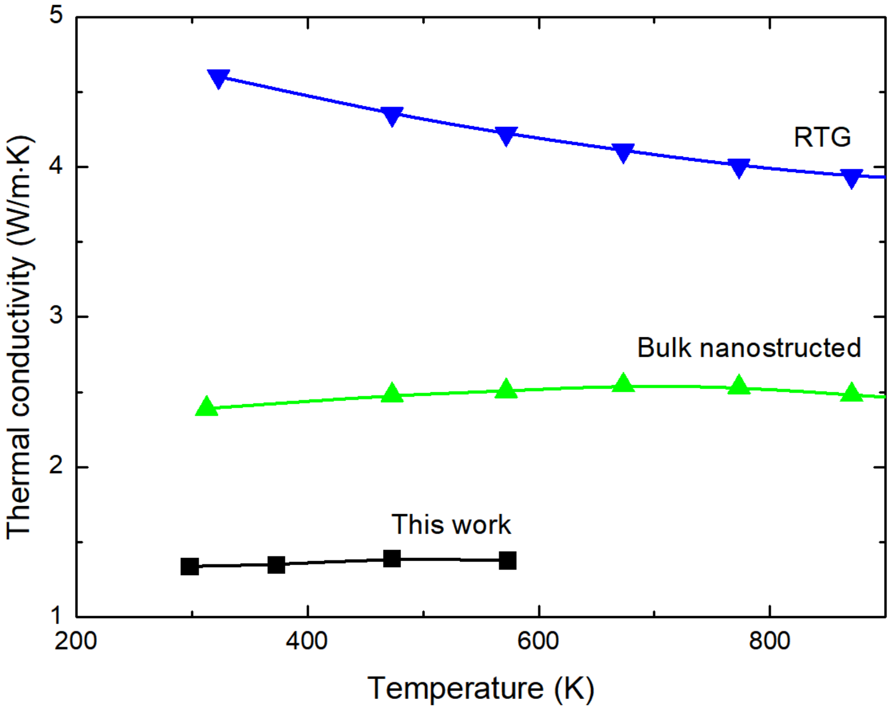

Figure 5.8. Thermal conductivity variation with temperature measurement results and comparisons with other reported bulk nanostructured and RTG $Si_{80}Ge_{20}$ materials.

5.1.8. Seebeck Coefficient

The high-temperature Seebeck coefficient measurement results and a comparison with other laser sintered thin film [76], bulk nanostructured [24], and RTG [24] $Si_{80}Ge_{20}$ materials are shown in Figure 5.9. Firstly, the absolute value of the Seebeck coefficient of n-type $Si_{80}Ge_{20}$ increases with temperature. Secondly, thin-film $Si_{80}Ge_{20}$ has both a higher Seebeck coefficient and a higher rate of increase when the temperature is raised. The Seebeck coefficient of the thin-film $Si_{80}Ge_{20}$ reported in this work increases faster than bulk nanostructured $Si_{80}Ge_{20}$ samples and the other reported thin-film samples. For our champion laser sintered thin film, the Seebeck coefficient increases from -144.9 μV/K at room temperature to -390.1 μV/K at 873 K, as shown in Figure 5.9.

The Seebeck coefficient of thin-film $Si_{80}Ge_{20}$ increases more than bulk nanostructured $Si_{80}Ge_{20}$ at elevated temperatures. Such a phenomenon can be explained by the porosity of the thin film [111]. In this work, the highly porous as-deposited film was sintered by laser, and the porosity was reduced. The nanopores formed during laser sintering can improve the Seebeck coefficient due to the energy filtering effect [112]. By carefully selecting the laser power, pulse width, and repetition rate, the post-sintered film gains a significantly higher Seebeck coefficient at high temperature when compared to bulk nanostructured $Si_{80}Ge_{20}$.

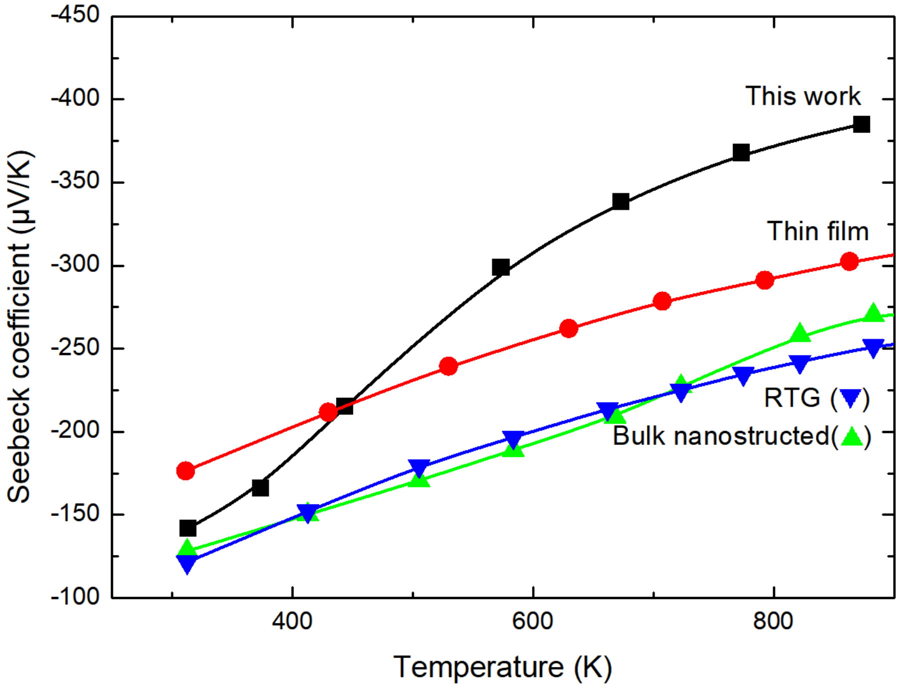

Figure 5.9. Seebeck coefficient variation with temperature measurement results and comparisons with other reported thin film, bulk nanostructured, and RTG $Si_{80}Ge_{20}$ materials.

5.1.9. Figure of Merit

The figure of merit of $Si_{80}Ge_{20}$ at 873 K can be estimated using the measured or estimated data. The best sample produced by laser sintering had a Seebeck coefficient of 390.1 μV/K at 873 K, an electrical conductivity of 62.1 S/cm at 873 K, and a thermal conductivity of 1.37 W/m · K at 573 K. As previously discussed, it is reasonable to assume that the thermal conductivity value at 573 K is similar to 873 K [24]. Therefore, the figure of merit at 873 K is estimated to be 0.60. In comparison, bulk nanostructured $Si_{80}Ge_{20}$ samples synthesized by Wang *et al.* using FAST had a figure of merit of ~1 at 873 K [24]. The difference is primarily due to the lower electrical conductivity of $Si_{80}Ge_{20}$ thin films, which may be improved further with higher doping. However, this result already demonstrates that when the temperature is raised to 873 K, the figure of merit of thin-film $Si_{80}Ge_{20}$ is comparable with bulk nanostructured $Si_{80}Ge_{20}$.

5.1.10. High-Temperature Stability

$Si_{80}Ge_{20}$ is typically used as a high-temperature thermoelectric material. Therefore, it is important to test the thermal stability because the thin films need to operate for long times under high temperature in real applications [9, 28].

The room temperature electrical conductivities for laser sintered $Si_{80}Ge_{20}$ thin films were measured between 3.6 S/cm and 70.5 S/cm depending upon the laser sintering parameters. The laser sintering parameters affect the activated dopant concentration and surface morphologies, which affects the electrical conductivity. The room temperature Seebeck coefficients are measured on the same batch of samples and show values between -139.6 µV/K and -145.2 µV/K. The Seebeck coefficients of different samples are all similar because it is mostly independent of the laser sintering process, as reported in Section 5.1.8 [94].

A sample with a room-temperature electrical conductivity of 12.3 S/cm and a Seebeck coefficient of -142.5 µV/K was split into two pieces, and all physical parameters were measured on both pieces to ensure the results were close enough to each other, i.e., within measurement system error.

The first piece (sample A) was heated to 1073 K and kept in 10^{-8} Torr vacuum for 3 hours, while the second piece (sample B) was heated to 1073K for 3 hours in the air. The results of the high-temperature stability test are shown in Table I. After taking the sample out of the furnace, an obvious oxidation layer was formed on top of sample B, while no obvious change was visually noticed on sample A. The electrical conductivity and Seebeck coefficient became non-detectable on sample B. However, after removing the top 80 nm of the oxide-containing thin film using argon ion sputtering, the electrical conductivity recovered to 11.3 S/cm and the Seebeck coefficient recovered to -141.6 μV/K. This experiment indicates that oxidation is the main problem when the temperature is elevated in the air. On the other hand, when the heating was carried out in vacuum at a temperature of 1073 K, sample A only showed a slight change of the Seebeck coefficient and the electrical conductivity, indicating that the air oxidation needs to be avoided for high ZT. Table 3 is the summary of the high-temperature stability tests.

Table 3. High-temperature stability test results

	Electrical conductivity (S/cm)	Seebeck coefficient (μV/K)
Room Temperature	12.3	-142.5
1073 K in vacuum for 3 hours	12.9	-139.5
1073 K in the air for 3 hours	(not measurable)	(not measurable)
1073 K in the air after sputtering	11.3	-141.6

5.2. Thermoelectric Thin Films Prepared by Ball Milling and Laser Sintering

5.2.1. Surface Morphology and EDS

Figure 5.10 (a) shows the SEM of an as-deposited $Si_{80}Ge_{20}$ thin film. The ball milling parameters were optimized to get a smaller particle size while minimizing the contamination due to the ball milling process. Figure 5.10 (a) indicates that most of the particles were less than 1 μm. The EDS result of the as-deposited $Si_{80}Ge_{20}$ thin films confirmed that the ratio of

Si:Ge was 80:20, and the contamination was less than the detection limit of EDS. The thickness of the as-deposited $Si_{80}Ge_{20}$ thin films was measured as 15 μm.

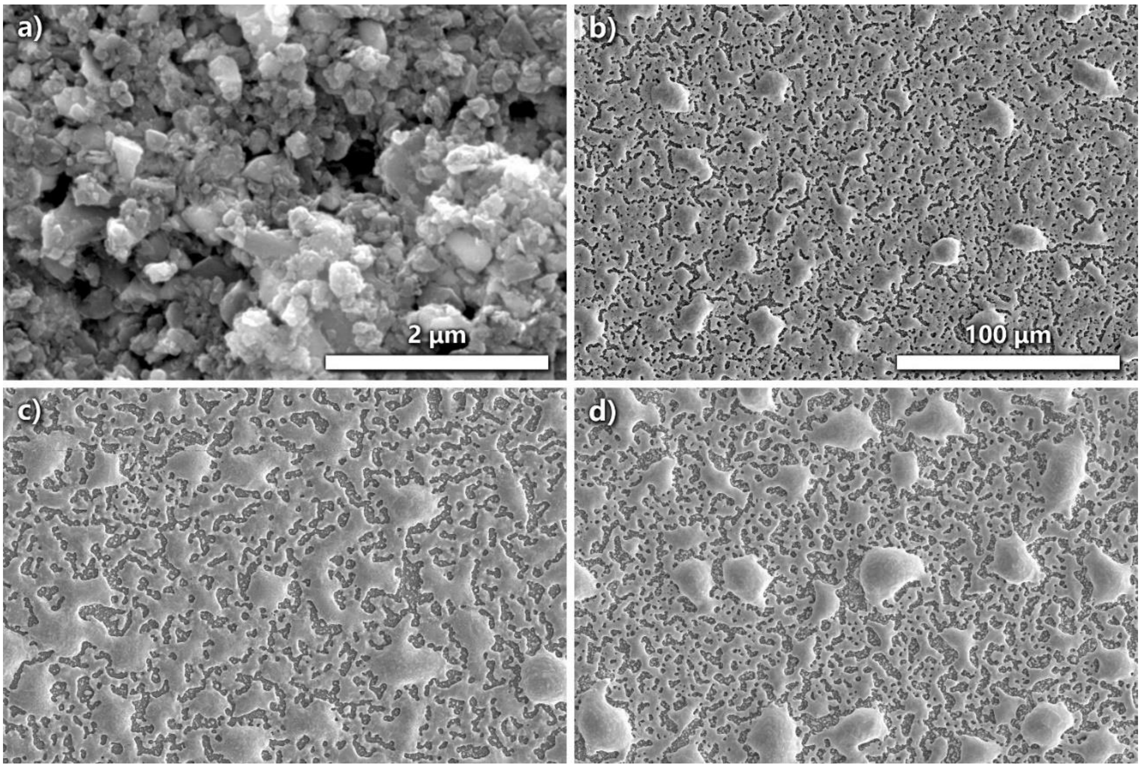

Figure 5.10. (a) SEM image of an as-deposited $Si_{80}Ge_{20}$ thin film showing sub-micron particles. SEM image of the laser-sintered $Si_{80}Ge_{20}$ thin films with laser power of (b) 20%, (c) 30%, (d) 40%.

Three samples were sintered with different laser power (P) of 20%, 30%, and 40%, as shown in Figure 5.10 (b), (c), and (d), separately. The scale bar in (b) also applies to (c) and (d). These samples were selected to demonstrate the effect of the different laser sintering power. All other laser sintering parameters were the same, as reported in Section 3.1.2. There are two different surface morphologies of laser-sintered $Si_{80}Ge_{20}$ thin films, which are designated as balling structure and percolation structure. The percolation structure forms when the laser sintering generates good wetting to the substrate. The percolation structure has more conductive paths and thus produces higher electrical conductivity than the balling structure

[113]. In all three samples, both balling structures and percolation structures were formed during laser sintering. However, in the P = 30% sample, the balling phenomenon was the least. Therefore, there is a "laser sintering power window" for the best substrate wetting. This is an important concept for the selection of laser sintering parameters, which will be further discussed in Section 5.3.1.

5.2.2. Crystallization and Grain Size

The crystal structure was determined by XRD for the deposited and laser-sintered thin films, and the results are shown in Figure 5.11 for quartz substrates, PSLS $Si_{80}Ge_{20}$ thin films, as-deposited ball milling thin films, and laser-sintered ball milling thin films (P = 30%).

The silicon peaks and germanium peaks are marked with # and * in the spectrum of the as-deposited $Si_{80}Ge_{20}$ thin film, separately. The $Si_{80}Ge_{20}$ alloy peaks were not found in the as-deposited films. The substrate fused quartz had a relatively strong X-ray background signal, which made the $Si_{80}Ge_{20}$ alloy peaks difficult to be detected. By calculating the XRD spectrum of as-deposited $Si_{80}Ge_{20}$ thin films using the Williamson–Hall method, the average grain sizes of silicon and germanium were determined as 47 nm and 34 nm, separately. The average grain size was much smaller than the particle size observed in the SEM image. This indicates that there were multiple grain sizes within each particle, which could be explained by the grain refinement during the ball milling process. However, the as-deposited thin films did not have any mechanical alloying phenomenon, as reported by other studies [24, 84, 114]. Wang et al. reported that the well alloyed as-milled $Si_{80}Ge_{20}$ had an average grain size of 12 nm, which was smaller than the grain size in our experimental setup. This could be due to the shorter ball milling time and the lower ball milling kinetic energy in our experiment. However, an extended ball milling time or higher RPM was creating detectable metal contamination. The MAUD program quantitative analysis was used to confirm the ratio of Si:Ge to be 79.2:20.8, which verified that the composition of the as-deposited thin film was as planned.

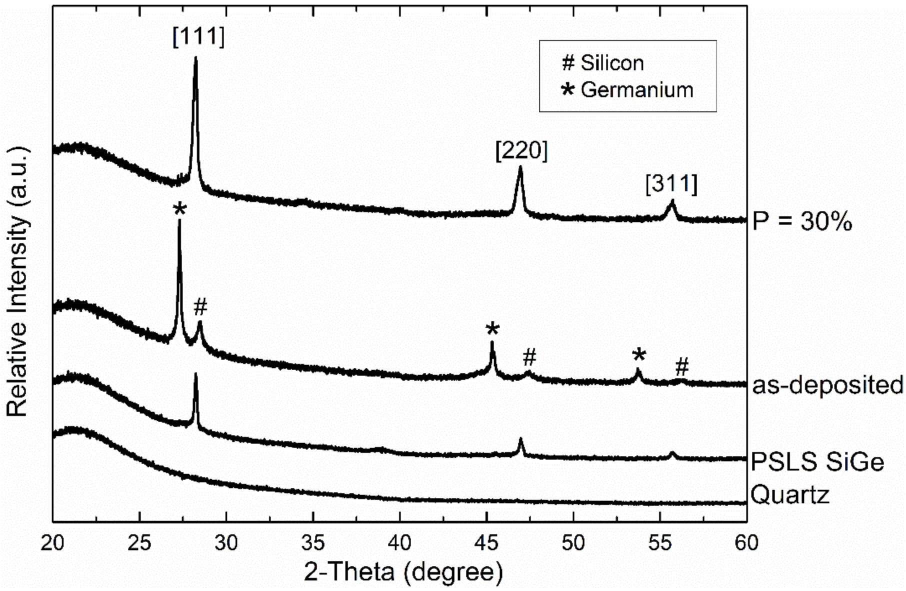

Figure 5.11. XRD patterns for quartz substrates, PSLS $Si_{80}Ge_{20}$ thin films, as-deposited ball milling thin films, and laser-sintered ball milling thin films (P = 30%)

The XRD patterns of laser-sintered ball milling thin films (P = 30%) and PSLS $Si_{80}Ge_{20}$ thin films are also shown in Figure 5.11. The three clear broadened peaks shown in the top spectrum confirmed that the P = 30% sample was well-alloyed $Si_{80}Ge_{20}$ with a small grain size. By calculating the XRD spectrum using the Williamson–Hall method, the average grain size of laser-sintered $Si_{80}Ge_{20}$ thin film was 50 nm, which was slightly larger than in an as-deposited thin film. The small increase indicates that the laser sintering was capable of creating well alloyed thermoelectric materials while minimizing grain growth. In comparison with the PSLS method, although the starting average grain size was only 8 nm, the laser-sintered thin films had a larger final average grain size of 68 nm [50, 93, 94]. In the plasma synthesized thin film, the particle size was similar to the size of the grain. When the laser was applied to the porous film, the heat could accumulate in each particle and lead to quick melting and recrystallization, which significantly increased the average grain size from 8 nm to 68 nm. In comparison, the as-deposited thin film prepared by ball milling in this work had a lower porosity and larger particle sizes. When the sample was irradiated by laser, the less heat accumulation and hence the slower recrystallization resulted in a slower grain size growth, which was from 47 nm/34 nm to 50 nm. Therefore, the average grain size of 50 nm in this work was better than PSLS $Si_{80}Ge_{20}$ thin films. The peak positions also confirmed that the composition of Si:Ge was 80:20, which was the same as the starting material composition.

5.2.3. TEM Study

TEM images of laser-sintered $Si_{80}Ge_{20}$ thin films are shown in Figure 5.12, and both figures are BMLS samples. In comparison with as-deposited thin films, $Si_{80}Ge_{20}$ nanoparticles were melted and interconnected with each other. Oxide shells could also be observed. As seen from the image, the typical grain sizes were in the range of 20-50 nm. These results indicate that the as-deposited nanoparticles were not completely but partially melted and solidified. During the laser sintering, two processes occur simultaneously: 1) The adjacent nanoparticles were melted and merged together to form a larger grain. 2) The necking formed between nanoparticles created the percolation structure and provided the electrically conductive paths. The former is the process that increases the grain size and the thermal conductivity, thus reducing the figure of merit. The latter is the process that increases the electrical conductivity.

Therefore, the laser sintering parameters need to be optimized for a good balance between the two factors.

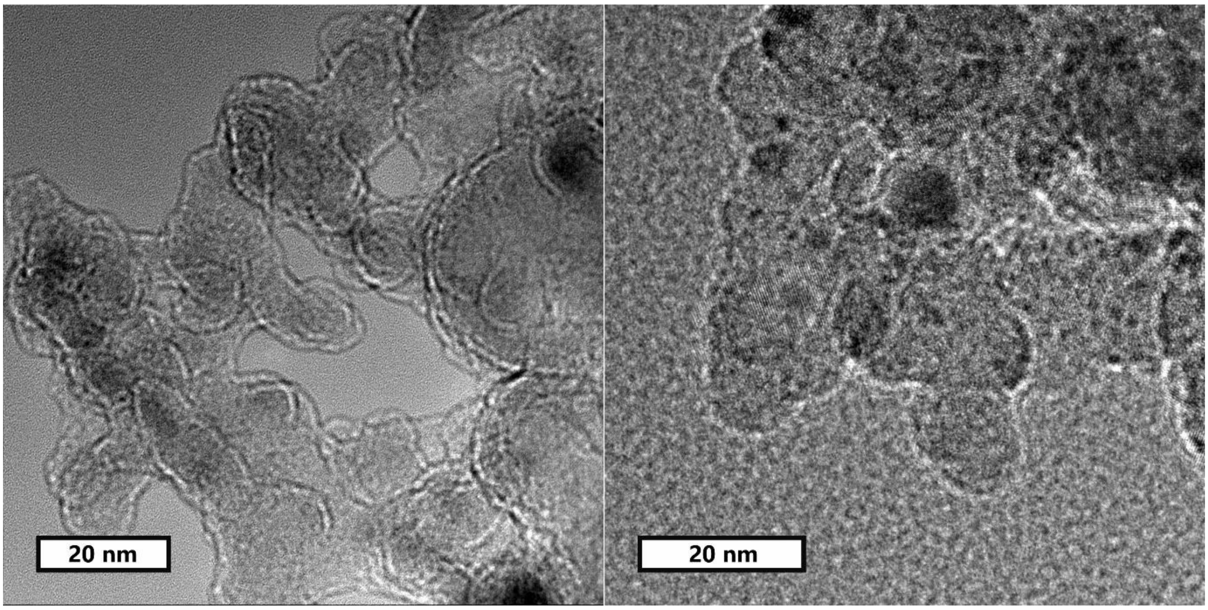

Figure 5.12. TEM images of two different BMLS $Si_{80}Ge_{20}$ thin films.

5.2.4. Electrical Conductivity

The high-temperature electrical conductivity measurement results and comparisons with other reported RTG, bulk nanostructured $Si_{80}Ge_{20}$ materials, and PSLS $Si_{80}Ge_{20}$ thin films are shown in Figure 5.13. In Section 5.1.6, it has been pointed out that thin films behave very differently than bulk materials [93]. In this work, for our best laser sintered thin film, the electrical conductivity of the P = 30% sample increased from 80.9 S/cm at room temperature to 118.5 S/cm at 873 K. Although the increasing of electrical conductivity with the temperature was also observed in this work, the improvement from room temperature to 873 K was not as great as the PSLS method, which is 1.46 times instead of 3.1 times. There are two reasons to explain this phenomenon. Firstly, the thickness of the P = 30% sample was 10 µm after sintering, which was thicker than 3-5 µm in the PSLS method. Secondly, the dopant concentration in the P = 30% sample was higher. The phosphorus ratio can be precisely controlled by adjusting the ball milling material composition, while the PSLS method can only change the nominal composition by adjusting the gas flow rate of the precursor gas. From the EDS results, the increase of the atomic percentage of phosphorus in as-deposited $Si_{80}Ge_{20}$ thin films also confirmed this conclusion. Although the electrical conductivity of the bulk nanostructured $Si_{80}Ge_{20}$ is still larger than the laser-sintered $Si_{80}Ge_{20}$ thin films, they are now in the same order of magnitude at high-temperature.

It is important to minimize oxidation during the ball milling and the laser sintering process. The EDS results did not find any oxygen in the well-handled samples. However, some other samples, which contained up to 6 at% oxygen, did not show measurable electrical conductivity. This result indicates that the performance was highly related to the oxidation. Because of the small particle size, even a small percentage of the oxidation shells could form insulating layers between conductive regions in the percolation structure [115–117].

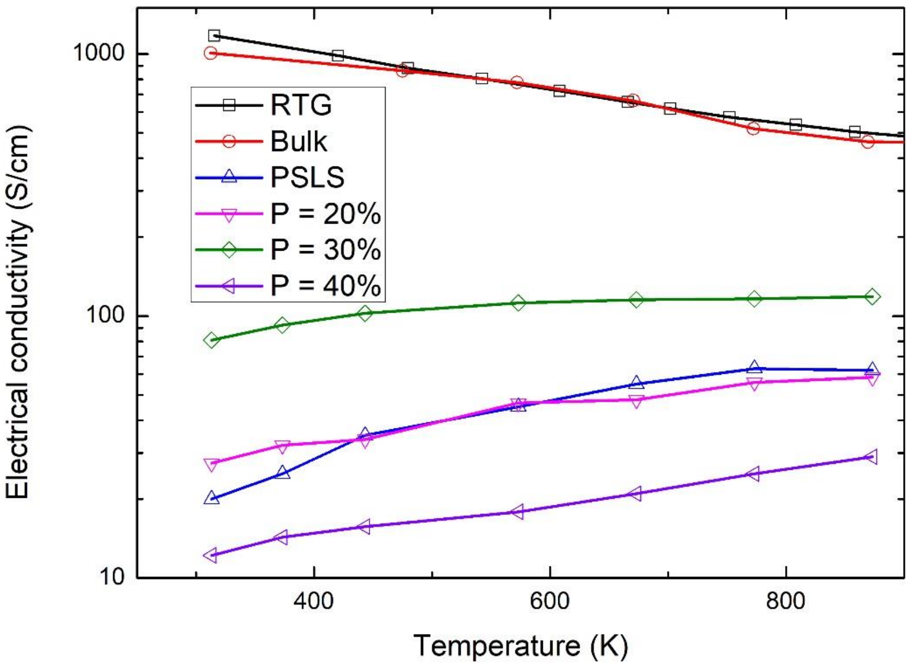

Figure 5.13. Electrical conductivity variation with temperature measurement results and comparisons with other reported RTG, bulk nanostructured $Si_{80}Ge_{20}$ materials, and PSLS $Si_{80}Ge_{20}$ thin films.

5.2.5. Hall Mobility and Carrier Concentration

The Hall mobility was measured on three laser-sintered samples. The as-deposited samples did not show any electrical conductivity. Thus, hall mobility measurements could not be performed. The results are summarized in Table 4.

Table 4. Electric properties of laser-sintered $Si_{80}Ge_{20}$ thin films with different laser-sintering power.

Laser Power	Hall mobility $cm^2V^{-1}s^{-1}$	Carrier concentration $\times 10^{19}\ cm^{-3}$	Electrical conductivity S/cm
P = 20%	10.5	1.6	27.4
P = 30%	10.0	5.0	80.9
P = 40%	13.9	0.54	12.2

The carrier concentration increases with the laser sintering power, then significantly decreases when it reaches the peak value. This trend indicates that the high laser power could activate more dopants, but it could also cause thermal evaporation loss. Because of the much lower melting point of phosphorus (860 K) compared with silicon (1687 K) and germanium (1211 K), the loss of the material during laser sintering was much significant for phosphorus. The thermal evaporation during laser sintering could be the main factor of dopant loss. Therefore, there is a "laser sintering power window" for the best carrier concentration. This is the second important criterion for the selection of laser sintering parameters, which will be further discussed in Section 5.3.1. For the P = 30% sample with the best electrical conductivity, the carrier concentration was $5.0 \times 10^{19}\ cm^{-3}$. In comparison, the ideal carrier concentration should be in the $10^{20}\ cm^{-3}$ range from both experimental and theoretical studies [24, 54, 58]. The porosity of the thin film and the dopant loss during laser sintering could be the reason for the one order of magnitude smaller carrier concentration. Currently, the cover glass placed on top of the laser-sintered sample reduced the dopant loss. However, future work could be done to further improve the dopant concentration, such as starting with a higher concentration of phosphorus or carrying out laser sintering with a dielectric coating on top of as-deposited films.

5.2.6. Seebeck Coefficient

The high-temperature Seebeck coefficient measurement results and a comparison with PSLS $Si_{80}Ge_{20}$ thin films, bulk nanostructured, and RTG $Si_{80}Ge_{20}$ materials are shown in Figure 5.14. The absolute value of the Seebeck coefficient of n-type $Si_{80}Ge_{20}$ increased with temperature, which improved the figure of merit at a high temperature. The Seebeck coefficient of the $Si_{80}Ge_{20}$ thin films increased faster than their bulk counterparts.

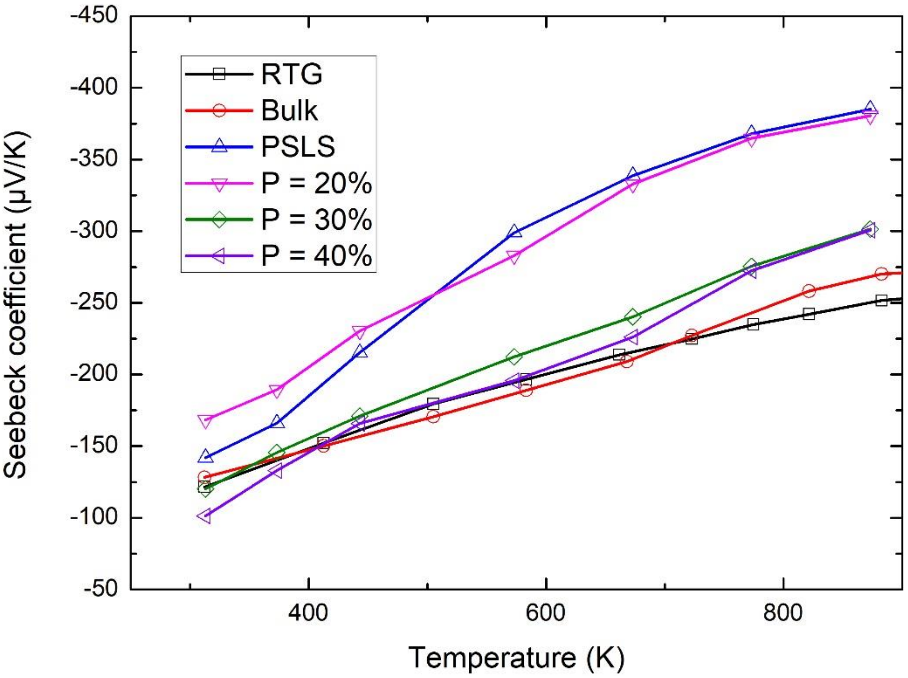

Figure 5.14. Seebeck coefficient variation with temperature measurement results and comparisons with other reported RTG, bulk nanostructured $Si_{80}Ge_{20}$ materials, and PSLS $Si_{80}Ge_{20}$ thin films.

For our best laser sintered thin film, the Seebeck coefficient of the P = 30% sample increased from -120.2 μV/K at room temperature to -301.5 μV/K at 873 K. Although the Seebeck coefficient of $Si_{80}Ge_{20}$ thin films increased more than bulk nanostructured $Si_{80}Ge_{20}$ at elevated temperatures, this increase was not as significant as that measured in PSLS $Si_{80}Ge_{20}$ thin films and the P = 20% sample. There are two major reasons that can explain the results. Firstly, the porosity created by the nanopores induced by laser sintering contributed to the increase of the Seebeck coefficient. The energy filtering effects can be used to explain such improvement [14, 112, 118]. However, the porosity of the thin films in this work was not as high as that in PSLS $Si_{80}Ge_{20}$ thin films and the P = 20% sample. Therefore, although the Seebeck coefficient was still improved and better than the bulk type $Si_{80}Ge_{20}$, it was not as large as PSLS. Secondly, the carrier concentration in the P = 30% sample was three times higher than that in the P = 20% sample. The Seebeck coefficient enhancement due to the energy filtering effect is more obvious when the dopant concentration is low, as reported by Lu et al. [118]. However, the improvement of the Seebeck coefficient due to the low dopant concentration is not high enough to compensate for the loss of electrical conductivity. In this work, although the P = 20% sample had a much larger Seebeck coefficient at high temperature, the figure of merit and the power factor were still lower than the P = 30% sample. There is a trade-off of the electrical conductivity and the Seebeck coefficient by carefully selecting the laser sintering parameters.

5.2.7. Thermal Conductivity

The high-temperature thermal conductivity measurement results and comparisons with other reported RTG, bulk nanostructured $Si_{80}Ge_{20}$ materials, and PSLS $Si_{80}Ge_{20}$ thin films are shown in Figure 5.15. Various works have reported that the thermal conductivity of nanostructured $Si_{80}Ge_{20}$ materials is not significantly affected by the temperature [24, 25]. Therefore, the same assumption is made, which is that the thermal conductivity of the P = 30% sample at 873 K could be estimated to be 1.5 $\mathrm{W/m \cdot K}$. This number is slightly higher than the PSLS $Si_{80}Ge_{20}$ thin films. It could be attributed to two factors. Firstly, the porosity of the thin films in this work was lower. Secondly, the average grain size was slightly larger than the PSLS $Si_{80}Ge_{20}$ thin films. However, the figure of merit was still enhanced by the relatively low effective thermal conductivity through phonon scattering at grain boundaries.

The thermal conductivity of the P = 20% sample was lower than the P = 30% sample, which could be another evidence of the theory in Section 5.2.6. The lower thermal conductivity may be due to the higher porosity in the P = 20% sample. By laser sintering of as-deposited $Si_{80}Ge_{20}$ thin films with the same thickness, the P = 30% sample ended with a thinner final thickness. The P = 20% sample was not sintered with a high enough temperature, so the densification would not be as good as the P = 30% sample. In conclusion, samples with higher porosity have a higher Seebeck coefficient and a lower thermal conductivity, but the improvement was not sufficient to compensate for the loss of electrical conductivity due to the higher porosity. Therefore, the overall performance was best for the P = 30% sample.

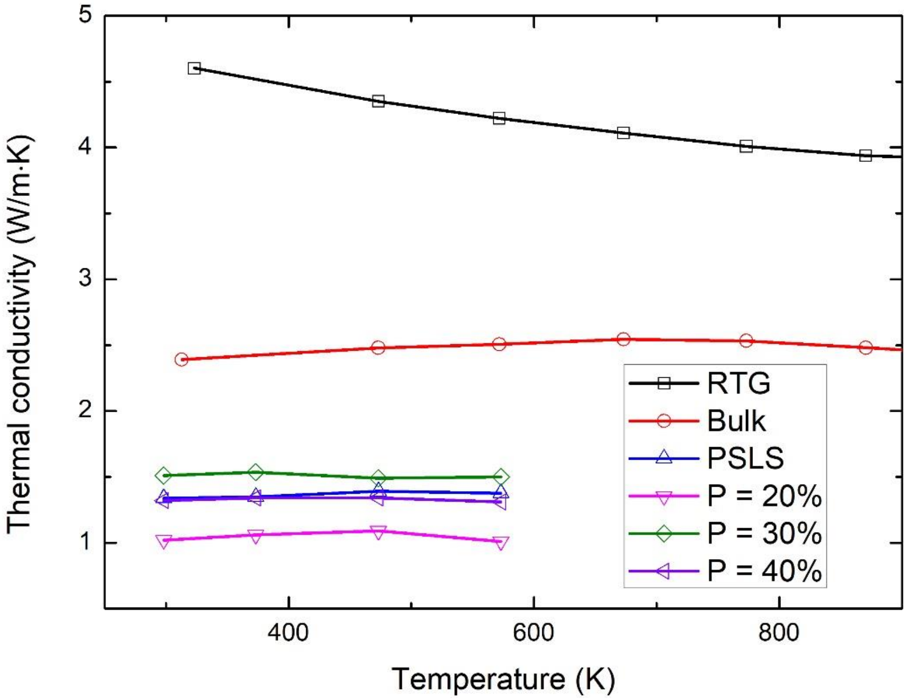

Figure 5.15. Thermal conductivity variation with temperature measurement results and comparisons with other reported RTG, bulk nanostructured $Si_{80}Ge_{20}$ materials, and PSLS $Si_{80}Ge_{20}$ thin films.

5.2.8. Figure of Merit

The figure of merit can be calculated or estimated using the previously measured results. The temperature dependence of the figure of merit is compared with bulk nanostructured and

RTG $Si_{80}Ge_{20}$ materials, as shown in Figure 5.16. The P = 30% sample had a Seebeck coefficient of -301.5 μV/K at 873 K and an electrical conductivity of 118.5 S/cm at 873 K. The thermal conductivity was estimated to be 1.5 $W/m \cdot K$ at 873 K, which was similar to the number at 573 K. Therefore, the figure of merit at 873 K was estimated to be 0.63. In comparison, the PSLS $Si_{80}Ge_{20}$ thin films reported in Section 5.1.9 had a figure of merit of 0.6 at 873 K [93]. The nanostructured n-type $Si_{80}Ge_{20}$ samples synthesized by Wang et al. using dc hot press had a figure of merit of ~1 [24].

The figure of merit of the $Si_{80}Ge_{20}$ thin films reported in this work is better than PSLS $Si_{80}Ge_{20}$ thin films and is comparable with the bulk type nanostructured $Si_{80}Ge_{20}$. Meanwhile, the trend shown in Figure 5.16 indicates that the figure of merit of our samples should get closer to the bulk type nanostructured $Si_{80}Ge_{20}$ at a higher temperature. This conclusion is also supported by the faster increasing Seebeck coefficient and the increasing of electrical conductivity variation with temperature, which significantly improves the performance of the $Si_{80}Ge_{20}$ thin films at a higher temperature. The laser-sintered films could be doped further using a p-doped sol-gel thin film or by gas phase doping process. This should enhance the electrical conductivity further, and hence a large figure of merit could be realized.

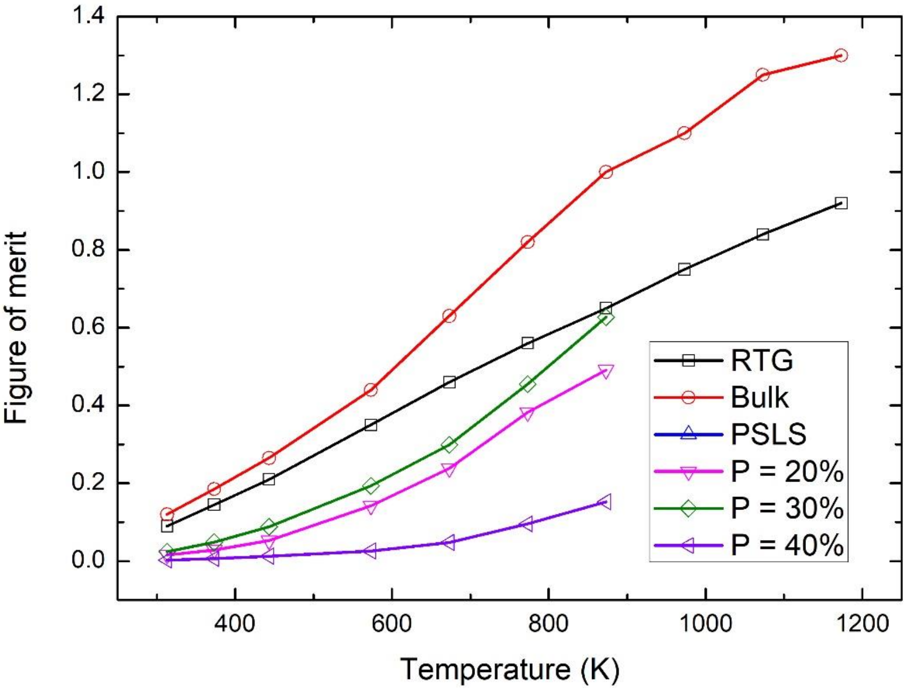

Figure 5.16. The figure of merit variation with temperature measurement results and comparisons with other reported RTG, bulk nanostructured $Si_{80}Ge_{20}$ materials, and PSLS $Si_{80}Ge_{20}$ thin films.

5.3. Discussion

5.3.1. Laser Sintering Power Window

There are two kinds of "laser sintering power window" mentioned in Section 5.2.1 and 5.2.5. The power-window for the best substrate wetting is the range of the laser power that can form the percolation structure. The power-window for the best carrier concentration is the range of the laser power that can maximize the dopant activation while minimizing the dopant evaporation loss. The difficulty in laser sintering is that the two power-windows are not necessarily overlapping. Therefore, other laser sintering parameters need to be changed if two power-windows are mismatching. For example, focal distance, pulse repetition rate, pulse width, scanning speed, scanning interval, and spot overlapping could be adjusted to match two power-windows. Therefore, the improved laser sintering setup would benefit from the use of high-speed Galvo instead of the x-y stage for laser sintering [94]. There are several advantages to this change. Firstly, it provides more flexibility in scanning speed to ease the power-windows matching requirements. A higher scanning speed resulted in a shorter film heating time and a smaller substrate heating effect. The dopant loss during sintering should be minimized to achieve better dopant concentration, which is desired for thermoelectric materials [119]. Finally, a higher scanning speed means better fabrication efficiency.

Although there have been many publications about the Si-Ge being used as high-temperature thermoelectric materials, most of them are the bulk type. The thin film Si-Ge thermoelectric materials are not well studied. This may be relevant to the difficulty in the fabrication and characterization of Si-Ge thin films. Firstly, some traditional methods, such as chemical vapor deposition and epitaxial growth, are expensive and slow. Therefore, it would be difficult to obtain thin films with enough thickness. Secondly, the dopant concentration cannot be precisely controlled. The dopant concentration may not be the same as the precursor gas ratio [93, 94]. Finally, the characterizations of thin films are more difficult. For example, it is more difficult to make reliable contacts; The 3ω-method is needed to measure the thermal conductivity, which is complicated and time-consuming. However, thin films also have many unique advantages: 1) They are more suitable for large surface area applications. 2) Thin films can be easily integrated into chip devices. 3) With the same weight of thermoelectric materials, thin films can cover a larger area than bulk materials, which means a larger temperature gradient can be realized.

In comparison with PSLS $Si_{80}Ge_{20}$ thin films, the BMLS $Si_{80}Ge_{20}$ thin film has many unique advantages. Firstly, the dopant concentration can be precisely controlled. $Si_{80}Ge_{20}$ thermoelectric materials require a high doping level for the best figure of merit [120–122]. But the plasma synthesis method had difficulty in increasing the phosphorus ratio in the thin film. In contrast, the amount of phosphorus being added to the ball milling process can be precisely controlled. Secondly, the micron-sized particles with nanograins are more suitable for laser sintering. The nanograins inside the particles are less affected when the particles are laser-sintered to form a percolation structure. The thermal conductivity is reduced by the nanograins, and the electrical conductivity is enhanced from the percolation structure. Finally, the ball milling process does not require a vacuum environment. Therefore, all steps introduced in this section could be integrated together in an assembly line, which will be suitable for low-cost mass production.

5.3.2. The Opposite Trend of Electrical Conductivity and Seebeck Coefficient

Most studies of bulk thermoelectric materials show that the electrical conductivity decreases and the Seebeck coefficient increases with temperature [24, 25, 123–125]. However, in prepared thin films, it has been found that the electrical conductivity and the Seebeck coefficient increased with temperature at the same time, as shown in Figure 5.7 and Figure 5.9. The electrical conductivity of our best sample increased from 80.9 S/cm at room temperature to 118.5 S/cm at 873 K. The Seebeck coefficient of the same sample increased from -120.2 μV/K at room temperature to -301.5 μV/K at 873 K.

There have been several studies reporting a similar phenomenon. Takashiri et al. reported that $Si_{0.8}Ge_{0.2}$ films doped at $4.3 \times 10^{19}\ \mathrm{cm}^{-3}$ with boron and synthesized by LPCVD showed simultaneously increased electrical conductivity and Seebeck coefficient with temperature [108]. A possible explanation suggested by this paper is that the segregation of the dopant at the grain boundaries may reduce the overall effective concentration of the extrinsic charge carriers [126].

Suen et al. reported that SnSe thin films synthesized by pulsed laser glancing-angle deposition showed increasing electrical conductivity and Seebeck coefficient at 300-477 K [127]. The paper explained this occurs due to the increasing intrinsic electron carrier concentration due to the thermal excitation [128].

Tajima et al. reported that phosphorus-doped $Si_{0.8}Ge_{0.2}$ thin films with carrier concentration from 10^{17}–$10^{18}\ \mathrm{cm}^{-3}$ and synthesized by RF-sputtering and thermal annealing had the same phenomenon from room temperature to 573 K [129]. The paper did not provide any explanation for the increasing of the electrical conductivity and Seebeck coefficient with temperature. However, this paper pointed out that local segregation of phosphorus may occur in the Si-Ge thin film.

Nishibori et al. reported that both Si thin films and Si-Ge thin films showed the same phenomenon from room temperature to 773 K [130]. Three types of samples were measured, Si-sputtering, Si-LPCVD, and Si-Ge-sputtering. The Si-sputtering sample showed an increasing Seebeck coefficient and slightly increasing electrical conductivity with temperature. The Si-Ge-sputtered sample showed an increasing Seebeck coefficient from 523K to 773 K and increasing electrical conductivity with temperature. The authors attributed this change in trend to the doping level of the films.

Stoib et al. reported that Si-Ge thin films synthesized by the laser-sintering of nanoparticles showed the same phenomenon from room temperature to 573 K [76]. The electrical conductivities of samples with Si/Ge ratios from 95:5 to 60:40 were measured and found to demonstrate the same trend. The authors used an empirical power law, $\sigma \propto \mathrm{T}^{\alpha}$, to describe the relationship between electrical conductivity and temperature, where the coefficient $\alpha > 0$ indicated increasing electrical conductivity with temperature. The authors also found that the coefficient decreased with the carrier concentration. Meanwhile, the secondary ion mass spectroscopy results indicated that approximately 40% of the dopant atoms were in the core of grains, while the remaining accumulated in the outer shell of grains. The results confirmed the segregation of the dopant at the grain boundaries mentioned in other papers [108, 129].

In conclusion, the phenomenon of increasing electrical conductivity and Seebeck coefficient with temperature could be explained by the segregation of the dopant at the grain boundaries. The overall carrier concentration was $5 \times 10^{19}\ \mathrm{cm}^{-3}$ in our best sample. However, due to the dopant segregation, the carrier concentration was not homogenous. The dopant atoms accumulated in the outer shell of the nanoparticles, and the carrier concentration at grain boundaries was higher after laser sintering. The core of grains may have a lower carrier concentration. Lu et al. reported that the carrier mobility of the samples with high doping concentrations decreased with increasing temperature, while the opposite behavior was found for samples with a low concentration [118]. The turning point was at a doping concentration between $1 \times 10^{19}\mathrm{cm}^{-3}$ and $3 \times 10^{19}\mathrm{cm}^{-3}$. In our sample, the segregation of dopant atoms may result in the carrier concentration at the grain boundaries being higher than the turning point, and the carrier concentration at the cores to be lower than the turning point.

Therefore, the high-temperature electrical behavior of an inhomogeneous, porous, percolated structure thin film cannot be explained by the simplified grain boundary trapping model [131]. The dopant segregation could be one of the important factors. Other theories may contribute to the explanation of this phenomenon, such as the tunnel junctions between conductive regions [132], and the distribution of low electrical conductivity barriers [133].

Chapter 6. Fabrication of Thermoelectric Devices

This chapter contains part of a manuscript under review:

Xie K, Gupta MC (2019) High Temperature Thermoelectric Energy Conversion Devices Using Si-Ge Thick Films Prepared by Laser Sintering of Nano/Micro Particles. *Submitted.*

6.1. Introduction and Motivation

Currently, the wide-scale application of thermoelectric materials is limited by their high cost and low efficiency [134]. The efficiency of thermoelectric devices could be improved by (1) using a thermoelectric material with a high figure of merit, (2) creating a large temperature difference between the hot and cold sides. The n-type $Si_{80}Ge_{20}$ thin film fabricated by the laser sintering process can reach a figure of merit of 0.6 at 873 K [93]. The figure of merit was improved by enhancing phonon scattering at nano-sized grain boundaries to reduce the thermal conductivity [24, 25]. The figure of merit of the n-type $Si_{80}Ge_{20}$ thin film is comparable with state-of-the-art bulk nanostructured $Si_{80}Ge_{20}$ reported by Want et al. in 2008 [24]. For the increase in temperature difference, a film type thermoelectric device is expected to maintain a larger temperature difference due to the larger dimensions.

In this chapter, ball milling of Si-Ge particles to achieve micro/nano particles followed by the laser-sintering method was used to fabricate a thick film thermoelectric device. We show a good figure of merit of the nanostructured $Si_{80}Ge_{20}$ film and a large temperature difference to achieve high-efficiency thermoelectric conversion devices. The ball-milling-laser-sintering (BMLS) method allows for easier doping of films and is of lower cost, and thus more suitable for mass production. The open-circuit voltage, output power, and internal resistance were measured at various temperature differences. The advantage of the BMLS method and potential applications are discussed.

6.2. Experiment

The BMLS method reported in Section 3.2 was used to fabricate the thermoelectric generator (TEG) [135]. The Si powders (99.999%, Sigma Aldrich), Ge powders (99.999%, Sigma Aldrich), and dopants were mixed in two different stainless-steel mortars. Phosphorus chunks (99.99%, Sigma Aldrich) were used for the n-type doping, and boron nanoparticles (99.9%, 100 nm, US Research Nanomaterials, Inc) were used for the p-type doping. The nominal composition of the ball milling powders was $Si_{80}Ge_{20}$ + 2% dopant. The mixtures were crushed with pestles and wet ball-milled with isopropyl alcohol (IPA) in Restch PM200 at 400 RPM for 3 hours. Then the n-type and p-type nanopowder pastes were diluted with methanol and preserved in two sealed glass bottles to prevent oxidation.

The BMLS-TEG process flow diagram is shown in Figure 6.1, and various steps of fabrication are described: (a) The n-type Si-Ge suspension was ultrasonicated for 15 min to get a uniform dispersion, then spin-coated on a quartz substrate. The film thickness can be adjusted by the spin speed and the viscosity of the nanopowder suspension. Then the sample was soft baked at 80 ℃ for 3 min to evaporate the residual organic solvent. (b) The as-deposited Si-Ge films were sintered with a quasi-continuous wave (QCW), near-infrared laser of wavelength 1070 nm laser. The laser sintering was performed at the pulse repetition rate (PRR) at 1000 Hz, the pulse width at 0.1 ms, scanning speed at 40 mm/s, and laser peak power at 300 W. These parameters were optimized to obtain good dopant concentration and percolation morphology

[93, 94]. The p-type Si-Ge legs were patterned by the selective laser sintering using a Galvo. (c) The sample was ultrasonicated in methanol to remove the unsintered nanoparticles and dried with nitrogen gas. (d) the revealed n-type Si-Ge legs were covered and protected by Kapton tapes. (e) Steps (a) – (c) were repeated with the n-type Si-Ge suspension to obtain the n-type $Si_{80}Ge_{20}$ legs. The optimized laser power was 35% instead of 30%. This may be due to the higher melting point of the boron. (f) The contacts were formed by thermal-evaporation of aluminum to connect the legs together.

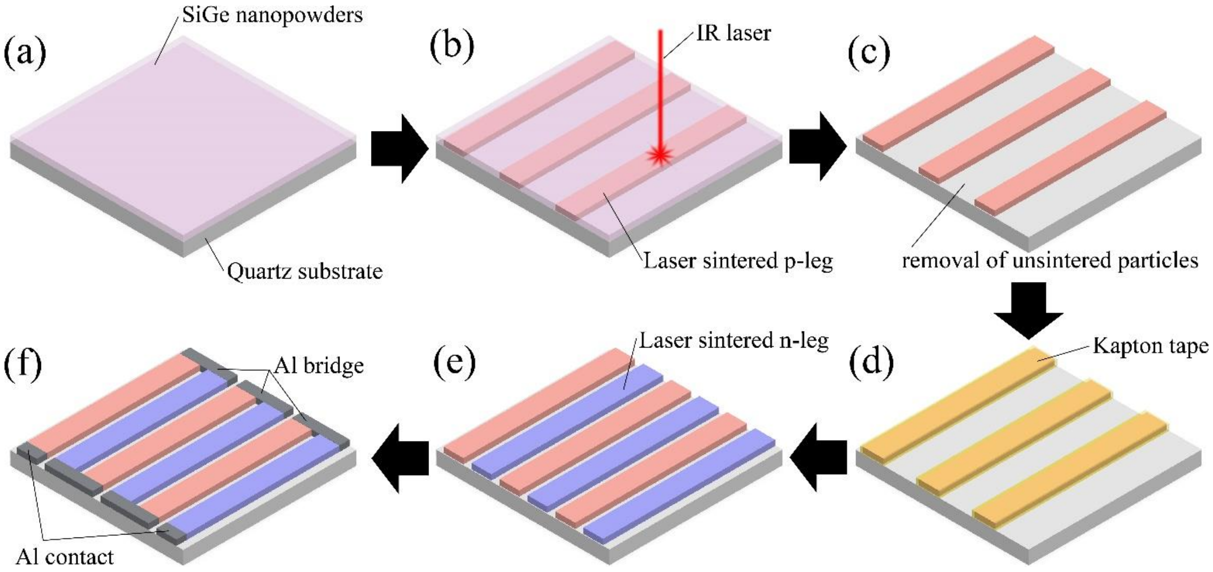

Figure 6.1. Process flow for the fabrication of a BMLS-TEG

The thermoelectric properties of the BMLS-TEG were measured using the experimental setup shown in Figure 6.2 (left). The whole setup was put inside a furnace to provide a high-temperature environment. An electrically nonconducting thermal grease was applied between the BMLS-TEG and the copper blocks to improve thermal conduction and was also used to attach thermal couple (TC) to the aluminum bridges. The maximum working temperature for the thermal grease was 1000 °C. The hot side temperature was measured by TC1 and TC2, and the cold side temperature was measured by TC3 and TC4. The open-circuit thermal voltage (V_{oc}) was measured with Keithley 2400 source meter.

The performance of each leg was measured individually by changing the position of the TCs. The TCs were used as the thermal voltage probe and the temperature sensor at the same time. Because the thermal grease could affect the electrical contact of TCs and films, the individual leg performance measurement must be performed before the device characterization.

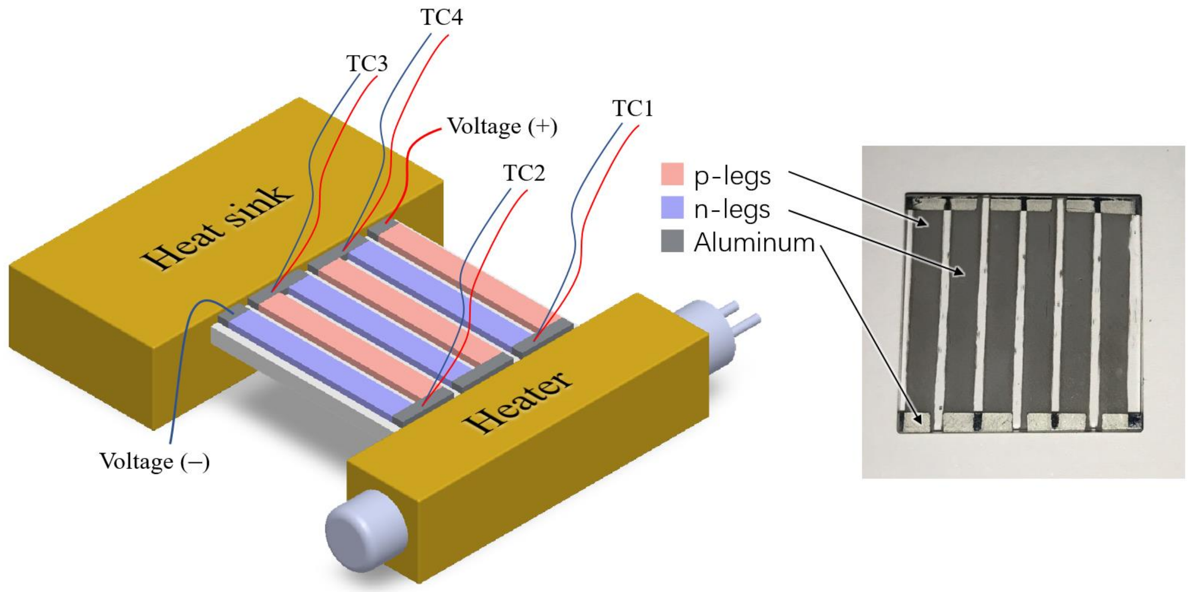

Figure 6.2. (left) Thermoelectric properties characterization setup, (right) optical image of the prototype BMLS-TEG.

6.3. Results

6.3.1. Thermoelectric Properties of p- and n-Type Legs

Figure 6.2 (right) shows the optical image of the prototype BMLS-TEG, which consists of 3 pairs of p- and n-type legs. Each leg is $3 \text{ mm} \times 21.5 \text{ mm} \times 10\ \mu\text{m}$.

Figure 6.3 shows the measured results for the Seebeck coefficient and electrical conductivity variation with temperature for p- and n-type legs. The properties of n-legs are very similar to the results reported in Section 5.2 [93]. The error bars were calculated from the variability of different legs. The small error bars in Figure 6.3 (left) indicate the laser-sintered $Si_{80}Ge_{20}$ films had a relatively stable Seebeck coefficient. This confirms that the Seebeck coefficient is primarily determined by the composition [76, 94]. In contrast, the surface morphology and carrier concentration of each leg may not be identical. Therefore, the variation of electrical conductivity was much larger, as shown in Figure 6.3 (right).

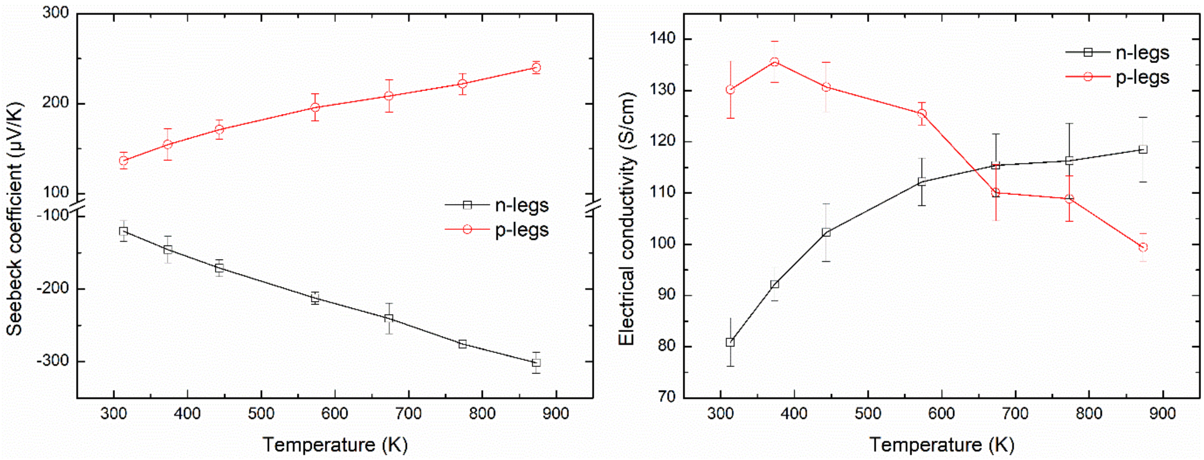

Figure 6.3. (left) The measured Seebeck coefficient variation with temperature, (right) The measured electrical conductivity variation with temperature. The error bars in both graphs indicate the variability of different legs.

The simultaneously increasing electrical conductivity and Seebeck coefficient phenomenon has been discussed in Section 5.3.2. The opposite trend of the electrical conductivity may be explained by the segregation of the dopant at the grain boundaries [108, 126, 129]. In this thermoelectric device, the electrical conductivity and the Seebeck coefficient of n-legs increased with temperature at the same time, as shown in Figure 6.3. However, the p-legs showed the same behavior as most of the bulk TE materials, i.e., the electrical conductivity decreases with temperature, and the Seebeck coefficient increases with temperature.

The overall carrier concentration of n-legs was 5×10^{19} cm^{-3}, as discussed in Section 5.2.5. However, due to dopant segregation, the carrier concentration may not be homogenous. The dopant atoms may accumulate in the outer shell of the nanoparticles [76]. Therefore, the carrier concentration at grain boundaries may be higher after laser sintering, while the core of grains may have lower carrier concentration. In n-legs, the segregation of dopant atoms might lead to the carrier concentration at grain boundaries to be higher than the turning point, and the carrier concentration inside the grains to be lower than the turning point. Therefore, when the temperature was increased, the grains with low carrier concentration may contribute to the increase in the electrical conductivity and the Seebeck coefficient. In contrast, the p-legs were doped with boron, which has a much higher melting point in comparison with phosphorus. The out-diffusion of dopants in p-legs during laser sintering would not be as significant as that in n-legs. Therefore, the electrical conductivity and Seebeck coefficient variations with the temperature of p-legs were similar to bulk thermoelectric materials. The opposite trend was not observed, possibly due to the less dopant segregation.

6.3.2. Open-Circuit Voltage

The high-power heater in the measurement setup was controlled by a proportional-integral-derivative (PID) controller to maintain the hot side (TC1 and TC2) at 873 K during the test. The final temperature of the cold side could be adjusted by changing the furnace temperature and the size of the heat sink. V_{oc} was recorded by a LabVIEW program under different temperature differences, as shown in Figure 6.4.

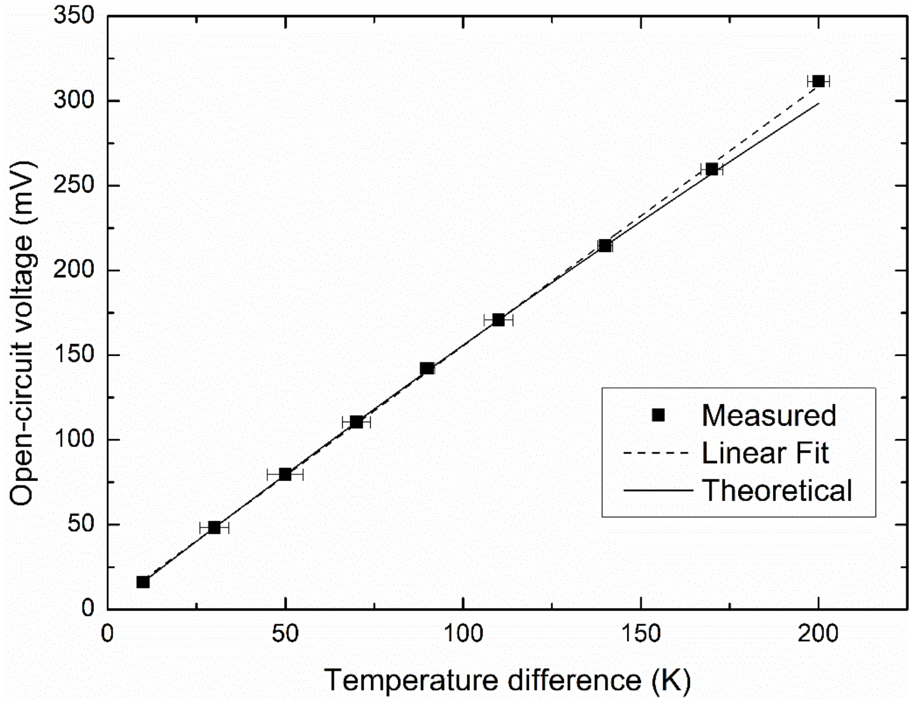

Figure 6.4. The measured open-circuit voltage variation with temperature differences. The theoretical value is simulated based on the Seebeck coefficients of p- and n-type legs.

The measured V_{oc} shows a linear dependence on the temperature difference. The temperature error bars are determined by the readings from the four thermal couples. The highest V_{oc} of 311.6 mV was obtained at the temperature difference of 200 ± 2 K. The $V_{oc}/\Delta T$ was found to be 1.53 mV/K. This value matched well with the estimated value from Seebeck coefficients of n-type and p-type $Si_{80}Ge_{20}$ films $(288.5 + 231.1)\mu V/K \times 3 \text{ pairs} = 1.56 \text{ mV/K}$. This result confirms that the small TCs directly attached to the device have much better accuracy than attaching to the hot/cold blocks.

6.3.3. Thermoelectric Power Output

The thermoelectric power output of the BMLS-TEG could be calculated by $P_{out} = V_{load} \times I_{work}$, where V_{load} is the voltage on the load and I_{work} is the current. Therefore, the different external loads were connected to the BMLS-TEG, and the load voltage (V) and the current (I) were measured by a digital multimeter.

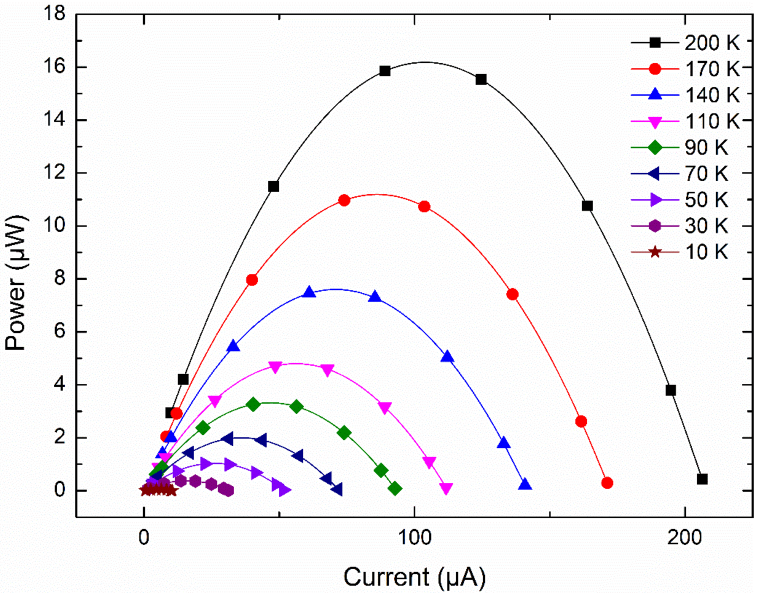

Figure 6.5. The output power vs. current at different temperature differences.

The measured results of power vs. current at different temperature differences are shown in Figure 6.5. The output power at each temperature difference could be calculated by $P_{out} = V_{oc}I - I_{work}^2 R_{int}$, where $V_{oc}I$ is the total power, which is a constant when the temperature difference is the same, $I_{work}^2 R_{int}$ is the joule heating loss due to the internal resistance. The maximum power of $15.85\ \mu W$ was obtained at a temperature difference of 200 ± 2 K. The effective device area (Aₑ) of the BMLS-TEG was $6 \times 3\ mm \times 10\ \mu m = 0.18\ mm^2$. The effective power density was calculated by $P_{max}/A_e = 8.8\ mW/cm^2$.

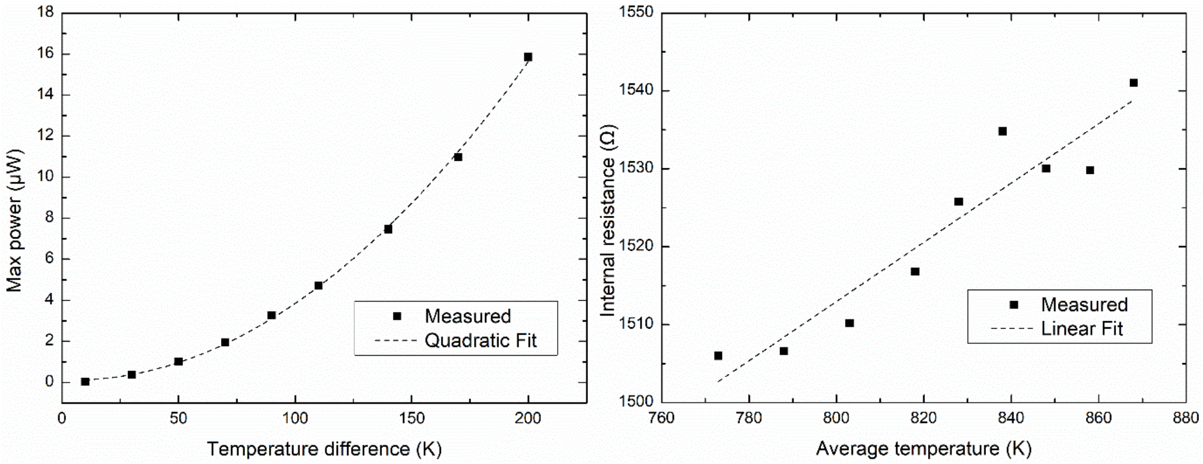

Figure 6.6. (left) The max power variation with temperature differences, (right) The internal resistance variation with average temperatures.

6.3.4. Internal Resistance

The maximum power $P_{max} = V_{oc}^2/4R_{int}$ occurs when the load resistance is equal to the internal resistance R_{int}. The max power variation with temperature differences is shown in Figure 6.6 (left). The result confirms that the temperature difference could significantly impact the performance of the thermoelectric devices ($P_{max} \propto \Delta T^2$). The advantage of the film type thermoelectric device is that it is much easier to maintain a large temperature difference compared with the bulk type thermoelectric device. The temperature difference obtained in this work is 200 K. This could be further improved by using a thinner substrate or by improving the cooling method at the cold end.

The internal resistance variation with average temperatures is shown in Figure 6.6 (right). The internal resistance slightly increased from 1506 Ω to 1541 Ω when the average temperature increased from 773 K to 873 K. If the resistance is estimated using the same electrical conductivities as in Section 5.2.7, 3 pairs of p-legs and n-legs with the dimension of $3\ \mathrm{mm} \times 21.5\ \mathrm{mm} \times 10\ \mu\mathrm{m}$ should have a total resistance of 440 Ω [93]. This value is much smaller than the measured value. The difference between calculated and measured resistances is possibly due to the presence of the contact resistance and some oxidation of the film.

6.4. Discussion

Rowe et al. pointed out that conversion efficiency increases with the thermoelement length. However, the peak value of the power output per area (effective power density, $\mathrm{mW/mm^2}$) is achieved at a relatively shorter thermoelement length [67]. Conventional bulk thermoelectric modules are mostly made of p- and n-type pellets [136]. The thermoelement length is usually 1-2 mm, which is optimized for the best effective power density. In practical applications, the area of the heat source is usually small, such as the CPU or a wearable device. In this circumstance, the power density would be the primary concern because of the limited heating area.

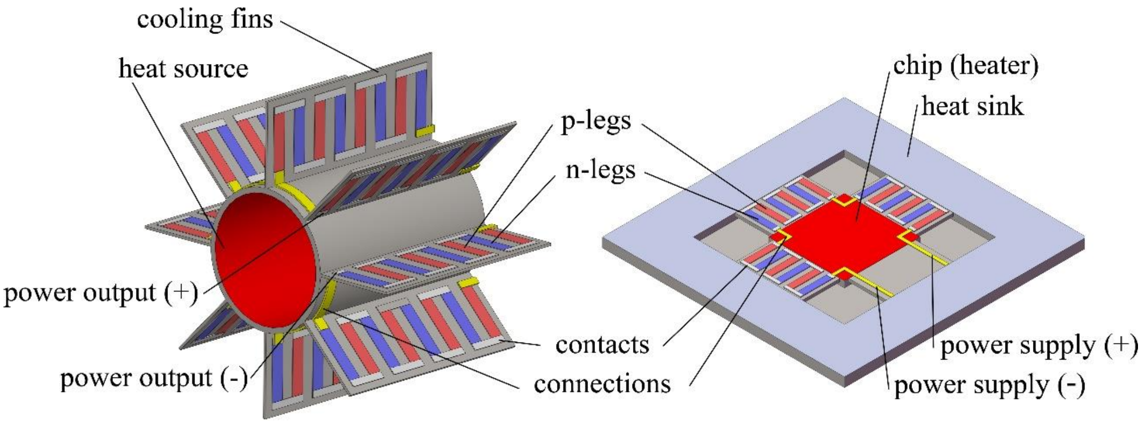

Figure 6.7. (left) Schematic diagram of a BMLS-TEG for large-area applications. (right) Schematic diagram of an on-chip cooling device.

The BMLS-TEG is suitable for the optimized energy conversion efficiency instead of the effective power density. If the heating area is large but with a relatively low heat power density ($\mathrm{W/cm^2}$), it is not cost-effective to cover the whole area with bulk thermoelectric modules. In contrast, for the same volume of the used thermoelectric materials, a BMLS-TEG may cover a much larger area. This means the more heat power could be used by the BMLS-TEG than used by the bulk thermoelectric module. Meanwhile, it is easier to maintain a large temperature gradient for the BMLS-TEG due to a large thermoelement length, which is one of the most significant advantages. Figure 6.7 (left) shows a schematic diagram of a BMLS-TEG for large-area applications. A high-temperature pipe, for example, the exhaust pipe or the engine pipe of automobiles, is installed with several cooling fins. The TEG could be fabricated on both sides of cooling fins using solution-coating followed by laser-sintering. The TEG could generate electricity from the temperature difference between the edge of the cooling fins and the high-temperature pipe. There are two advantages to this design. 1) It does not change the major structure of the original design. If a conventional bulk TEG is used, it needs to be installed between the cooling fins and the heat pipe. 2) As discussed in Section 6.3.4, the maximum power output occurs when the load resistance is equal to the internal resistance. In this design, the serial or parallel connection of all thermoelectric modules could be adjusted by changing the pattern of the metal connections.

Figure 6.7 (right) shows a BMLS-TEG used as planar thermoelectric modules for on-chip cooling applications. Currently, the planar thermoelectric modules are mostly fabricated using metal-organic chemical vapor deposition (MOCVD) [40, 137], low pressure chemical vapor deposition (LPCVD) [41, 138], pulse electroplating (PED) [139], Magnetron sputtering [140], and molecular beam epitaxy (MBE) [141]. However, these methods have three common disadvantages. Firstly, they require expensive facilities and complicated recipe adjustments that increase the cost of fabrication. For example, the nominal precursor gas ratio may not produce the same stoichiometric films. The dopant concentration also needs additional adjustment to reach the designed level. High-temperature annealing is needed for recrystallization and dopant activation [142, 143]. In contrast, the BMLS method can control the material composition in an easy and precise way. The crystallization and dopant activation could be done at the same time during the laser sintering process. Secondly, the deposition rate in these methods is relatively slow. It takes several hours to fabricate the legs of μ-TEGs using conventional methods [144]. Therefore, these methods are not suitable for mass production due to the slow speed and the high cost. In contrast, BMLS method can fabricate a thick film at a much higher speed. The total cost of the BMLS method is also lower than any conventional method. Finally, p- and n-type legs are fabricated separately in all these methods, which bring additional assembly steps or photolithography steps. In contrast, the thermoelectric legs were patterned by the selective laser sintering in BMLS method, which allows the fabrication on arbitrary shapes. The selective laser sintering also allows the use of low-temperature flexible substrates, which could be used to fabricate a flexible TEG. These unique advantages make the BMLS method to be more attractive for mass production, and could be used to substitute the MEMS approach for μ-TEGs or other micro-thermoelectric modules.

Chapter 7. Conclusion and Future Work

7.1. Conclusions

In this work, the laser sintering process was used as a versatile method for fabricating $Si_{80}Ge_{20}$ thin films for thermoelectric applications. The as-deposited nanoparticle thin films were prepared by a plasma synthesis method and a ball milling method. This thesis demonstrates that these novel fabrication methods are easier, faster, and lower-cost ways to fabricate the film type thermoelectric devices with high performance than traditional methods.

Firstly, a study was made using phosphorus-doped $Si_{80}Ge_{20}$ thin films prepared by laser sintering of plasma-synthesized nanoparticles. The grain size of as-deposited thin films was 8 nm. The grain growth during laser sintering resulted in a grain size of 68 nm. Therefore, the thermal conductivity was reduced to ~1.35 W/m · K from room temperature to 573 K, which would enhance the figure of merit. The Seebeck coefficient of the laser-sintered thin films increased from -144.9 μV/K at room temperature to -390.1 μV/K at 873 K. The electrical conductivity increased from 16.1 S/cm at room temperature to 62.1 S/cm at 873 K and demonstrated an opposite trend when compared to bulk nanostructured materials. The figure of merit of the PSLS $Si_{80}Ge_{20}$ was estimated to be 0.60 at 873 K, which is comparable to a value of ~1 for bulk nanostructured materials [24].

Secondly, a study was made using phosphorus-doped $Si_{80}Ge_{20}$ thin films prepared by laser sintering of ball-milled micro/nano particles. Although mechanical alloying is not significantly observed during ball milling in this work, laser sintering is capable of producing well-alloyed $Si_{80}Ge_{20}$ with an average grain size of 50 nm. The thermal conductivity was found to be

~$1.5\ \mathrm{W/m \cdot K}$ from room temperature to 573 K. The Seebeck coefficient was -120.2 μV/K at room temperature to -301.5 μV/K at 873 K. The electrical conductivity was measured as 80.9 S/cm at room temperature and 118.5 S/cm at 873 K. Therefore, the figure of merit of the BMLS $Si_{80}Ge_{20}$ was found to be 0.63 at 873 K which is comparable to a value of ~1 for bulk nanostructured materials [24].

Additionally, based on the experimental results, the following points are highly important in order to achieve ideal thermoelectric properties of $Si_{80}Ge_{20}$:

1. Surface morphology should be in a percolation structure instead of a balling structure. Substrate wetting and proper laser sintering parameters need to be optimized.
2. The laser power needs to be optimized for the best carrier concentration, which can maximize dopant activation while minimizing the dopant evaporation loss.
3. It is important to obtain dense thin films to achieve high ZT [111, 145], which could be fulfilled by starting with a denser as-deposited thin film or optimization of laser processing parameters.

Finally, a device consists of 3 pairs of n-type phosphorus-doped $Si_{80}Ge_{20}$ legs and p-type boron-doped $Si_{80}Ge_{20}$ legs were fabricated with the BMLS method. The maximum temperature difference of 200 K was achieved when the hot-side temperature was 873 K, and the cold-side was kept at room temperature in the air (no water cooling). The corresponding maximum thermovoltage and output-power were $311.6\ \mathrm{mV}$ and $15.85\ \mu\mathrm{W}$. The effective power density was calculated as $8.8\ \mathrm{mW/cm^2}$. The performance of the device could be further improved by increasing the hot side temperature to about $1000\ ^\circ\mathrm{C}$ and cooling the cold side by water circulation, to generate a larger temperature difference. The demonstrated method will be suitable for thermoelectric devices for large-area applications on arbitrary shapes. The presented method will also find applications for on-chip cooling and powering, which could substitute MEMS-based fabrication methods for μ-TEGs or other micro-thermoelectric modules with a simpler, cheaper, and faster fabrication process.

In conclusion, a new method for thermoelectric thin film fabrication using laser sintering of Si and Ge nanoparticles has been demonstrated with a thermal-to-electric conversion efficiency approaching the bulk value. Also, a fundamental understanding of laser-sintered $Si_{80}Ge_{20}$ thermoelectric materials has been provided, and a novel and viable concept of laser processing has been demonstrated for high-efficiency and low-cost thermoelectric device fabrication.

7.2. Future work

7.2.1. Preparation of As-Deposited Thin Films

In comparison with the plasma synthesis method, the ball milling method is more promising because it is easier, faster, and cost-effective. Therefore, the BMLS method was used to fabricate thermoelectric devices in this work. For future work, the ball milling process could be further improved. Firstly, if the porosity of as-deposited $Si_{80}Ge_{20}$ thin films could be further reduced, the laser-sintered thermoelectric thin films could have a higher density, which is preferred for thermoelectric devices [82, 146]. Secondly, if the average grain size of as-deposited thin films could be further reduced without a significant lowering of the particle size, this could decrease the final thermal conductivity without sacrificing the electrical conductivity.

Finally, if the ball milling process was performed with a higher kinetic energy device, mechanical alloying should be able to produce micro/nano particles with smaller grain sizes. The grain size after laser sintering could be further reduced, thus leading to a lower thermal conductivity and a better figure of merit.

7.2.2. Carrier Concentration

The electrical conductivity of the thin film $Si_{80}Ge_{20}$ reported in this work is still lower than bulk type $Si_{80}Ge_{20}$ materials. In this work, the carrier concentration was measured as $5.0 \times 10^{19}\ cm^{-3}$. However, the ideal carrier concentration should be in the $10^{20}\ cm^{-3}$ range from both experimental and theoretical studies [24, 54, 58]. This difference may be caused by dopant evaporation during laser sintering or unactivated dopant in the films. There are several approaches that could be attempted. Firstly, improving the ball milling process could improve the lattice substitution of phosphorus atoms into the crystal lattice. Better incorporation of dopant atoms could reduce the dopant out-diffusion during laser sintering, which will increase the dopant concentration. Secondly, better optimization of laser sintering parameters is needed, such as laser power, pulse width, repetition rate, wavelength, etc. The dopant activation should be maximized while maintaining the percolation structure.

7.2.3. Flexible Substrates

One of the most significant advantages of selective laser sintering is that the entire substrate is not heated to high temperatures. Therefore, the laser sintering method would be suitable for the fabrication of flexible thermoelectric devices. Kapton tapes with high-performance thermoelectric materials, e.g., BiTe, are promising for wearable thermoelectric energy harvesting.

7.2.4. Thermoelectric Devices

For future work, the device design could also be further improved for enhanced device performance besides the improvement of the thermoelectric materials mentioned in Section 7.2.1 and 7.2.2. Firstly, a larger temperature difference may be obtained by using thinner substrates. Secondly, the hot-end temperature could be increased by using a better heat source, and the cold-end temperature could be decreased by using cooling fins or a water-cooling system. In GPHS-RTG used by NASA, a Pu-238 heat source is used to provide the input heat (4500 W) to the 18 Si-Ge thermoelectric converters. The temperatures of the hot-end and cold-end were 1000 ℃ and 300 ℃, respectively [30]. Because the temperature difference will significantly improve the maximum power output ($P_{max} \propto \Delta T^2$), when ΔT increases from 200 K to 700 K, the performance of thermoelectric devices will be greatly improved. Finally, the contact resistance should be minimized by the selection of proper contact materials. Meanwhile, the contact material should also be able to work at high temperatures without deterioration [147].

References

1. He J, Tritt TM (2017) Advances in thermoelectric materials research: Looking back and moving forward. Science (80-) 357:. https://doi.org/10.1126/science.aak9997
2. Alam H, Ramakrishna S (2013) A review on the enhancement of figure of merit from bulk to nano-thermoelectric materials. Nano Energy 2:190–212. https://doi.org/10.1016/j.nanoen.2012.10.005
3. Schierning G (2014) Silicon nanostructures for thermoelectric devices: A review of the current state of the art. Phys status solidi 211:1235–1249. https://doi.org/10.1002/pssa.201300408
4. Orr B, Akbarzadeh A, Mochizuki M, Singh R (2016) A review of car waste heat recovery systems utilising thermoelectric generators and heat pipes. Appl. Therm. Eng. 101:490–495
5. Koumoto K, Terasaki I, Funahashi R (2006) Complex Oxide Materials for Potential Thermoelectric Applications. MRS Bull 31:206–210. https://doi.org/10.1557/mrs2006.46
6. Kim HS, Liu W, Ren Z (2017) The bridge between the materials and devices of thermoelectric power generators. Energy Environ Sci 10:69–85. https://doi.org/10.1039/C6EE02488B
7. C.A M, S.I O (2015) Design Analysis Of Kitchen-Waste-Heat Energy For The Production Of Telephones’ Chargers As An Alternative Grid Technology. J Multidiscip Eng Sci Technol 2:2801–2805
8. Minnich AJ, Dresselhaus MS, Ren ZF, Chen G (2009) Bulk nanostructured thermoelectric materials: current research and future prospects. Energy Environ Sci 2:466. https://doi.org/10.1039/b822664b
9. Bonham B, Guisbiers G (2017) Thermal stability and optical properties of Si–Ge nanoparticles. Nanotechnology 28:245702. https://doi.org/10.1088/1361-6528/aa726b
10. Gupta MC, Carlson DE (2015) Laser processing of materials for renewable energy applications. MRS Energy Sustain 2:E2. https://doi.org/10.1557/mre.2015.3
11. Taborda JAP, Romero JJ, Abad B, et al (2016) Low thermal conductivity and improved thermoelectric performance of nanocrystalline silicon germanium films by sputtering. Nanotechnology 27:175401. https://doi.org/10.1088/0957-4484/27/17/175401
12. Pérez-Taborda JA, Caballero-Calero O, Martín-González M (2017) Silicon-Germanium (SiGe) Nanostructures for Thermoelectric Devices: Recent Advances and New Approaches to High Thermoelectric Efficiency. In: New Research on Silicon - Structure, Properties, Technology. InTech
13. Vining CB (2009) An inconvenient truth about thermoelectrics. Nat Mater 8:83–85. https://doi.org/10.1038/nmat2361
14. Yang L, Chen Z-G, Dargusch MS, Zou J (2018) High Performance Thermoelectric Materials: Progress and Their Applications. Adv Energy Mater 8:1701797. https://doi.org/10.1002/aenm.201701797

15. Poudel B, Hao Q, Ma Y, et al (2008) High-Thermoelectric Performance of Nanostructured Bismuth Antimony Telluride Bulk Alloys. Science (80-) 320:634–638. https://doi.org/10.1126/science.1156446
16. Sood A, Cheaito R, Bai T, et al (2018) Direct Visualization of Thermal Conductivity Suppression Due to Enhanced Phonon Scattering Near Individual Grain Boundaries. Nano Lett 18:3466–3472. https://doi.org/10.1021/acs.nanolett.8b00534
17. Usenko A, Moskovskikh D, Gorshenkov M, et al (2017) Enhanced thermoelectric figure of merit of p -type Si 0.8 Ge 0.2 nanostructured spark plasma sintered alloys with embedded SiO 2 nanoinclusions. Scr Mater 127:63–67. https://doi.org/10.1016/j.scriptamat.2016.09.010
18. Yan X, Poudel B, Ma Y, et al (2010) Experimental studies on anisotropic thermoelectric properties and structures of n-type Bi2Te2.7Se0.3. Nano Lett 10:3373–3378. https://doi.org/10.1021/nl101156v
19. Zhao LD, Lo SH, Zhang Y, et al (2014) Ultralow thermal conductivity and high thermoelectric figure of merit in SnSe crystals. Nature 508:373–377. https://doi.org/10.1038/nature13184
20. Burton MR, Liu T, McGettrick J, et al (2018) Thin Film Tin Selenide (SnSe) Thermoelectric Generators Exhibiting Ultralow Thermal Conductivity. Adv Mater 30:1801357. https://doi.org/10.1002/adma.201801357
21. Chang C, Wu M, He D, et al (2018) 3D charge and 2D phonon transports leading to high out-of-plane ZT in n-type SnSe crystals. Science (80-) 360:778–783. https://doi.org/10.1126/science.aaq1479
22. Shi X, Chen ZG, Liu W, et al (2018) Achieving high Figure of Merit in p-type polycrystalline Sn0.98Se via self-doping and anisotropy-strengthening. Energy Storage Mater 10:130–138. https://doi.org/10.1016/j.ensm.2017.08.014
23. Wei TR, Tan G, Zhang X, et al (2016) Distinct Impact of Alkali-Ion Doping on Electrical Transport Properties of Thermoelectric p-Type Polycrystalline SnSe. J Am Chem Soc 138:8875–8882. https://doi.org/10.1021/jacs.6b04181
24. Wang XW, Lee H, Lan YC, et al (2008) Enhanced thermoelectric figure of merit in nanostructured n-type silicon germanium bulk alloy. Appl Phys Lett 93:193121. https://doi.org/10.1063/1.3027060
25. Joshi G, Lee H, Lan Y, et al (2008) Enhanced Thermoelectric Figure-of-Merit in Nanostructured p-type Silicon Germanium Bulk Alloys. Nano Lett 8:4670–4674. https://doi.org/10.1021/nl8026795
26. Samarelli A, Ferre Llin L, Cecchi S, et al (2014) Prospects for SiGe thermoelectric generators. Solid State Electron 98:70–74. https://doi.org/10.1016/j.sse.2014.04.003
27. El-Genk MS, Saber HH, Caillat T (2003) Efficient segmented thermoelectric unicouples for space power applications. Energy Convers Manag 44:1755–1772. https://doi.org/10.1016/S0196-8904(02)00217-0
28. Yang J, Caillat T (2006) Thermoelectric Materials for Space and Automotive Power Generation. MRS Bull 31:224–229. https://doi.org/10.1557/mrs2006.49

29. Bennett G, Lombardo J, Hemler R, et al (2006) Mission of Daring: The General-Purpose Heat Source Radioisotope Thermoelectric Generator. In: 4th International Energy Conversion Engineering Conference and Exhibit (IECEC). American Institute of Aeronautics and Astronautics, Reston, Virigina
30. Mason LS (2007) Realistic Specific Power Expectations for Advanced Radioisotope Power Systems. J Propuls Power 23:1075–1079. https://doi.org/10.2514/1.26444
31. Whalen SA, Apblett CA, Aselage TL (2008) Improving power density and efficiency of miniature radioisotopic thermoelectric generators. J Power Sources 180:657–663. https://doi.org/10.1016/j.jpowsour.2008.01.080
32. Bae EJ, Kang YH, Jang K-S, et al (2016) Solution synthesis of telluride-based nano-barbell structures coated with PEDOT:PSS for spray-printed thermoelectric generators. Nanoscale 8:10885–10890. https://doi.org/10.1039/C5NR07032E
33. Chen X, Dai W, Wu T, et al (2018) Thin Film Thermoelectric Materials: Classification, Characterization, and Potential for Wearable Applications. Coatings 8:244. https://doi.org/10.3390/coatings8070244
34. Bahk J-H, Fang H, Yazawa K, Shakouri A (2015) Flexible thermoelectric materials and device optimization for wearable energy harvesting. J Mater Chem C 3:10362–10374. https://doi.org/10.1039/C5TC01644D
35. Siddique ARM, Mahmud S, Heyst B Van (2017) A review of the state of the science on wearable thermoelectric power generators (TEGs) and their existing challenges. Renew Sustain Energy Rev 73:730–744. https://doi.org/10.1016/j.rser.2017.01.177
36. Leonov V, Torfs T, Vullers RJM, et al (2010) Renewable energy microsystems integrated in maintenance-free wearable and textile-based devices: The capabilities and challenges. In: 2010 IEEE International Conference on Industrial Technology. IEEE, pp 967–972
37. Kusano K, Yamamoto A, Nakata M, et al (2018) Thermoelectric Inorganic SiGe Film Synthesized on Flexible Plastic Substrate. ACS Appl Energy Mater 1:acsaem.8b00899. https://doi.org/10.1021/acsaem.8b00899
38. Leonov V, Torfs T, Fiorini P, Van Hoof C (2007) Thermoelectric Converters of Human Warmth for Self-Powered Wireless Sensor Nodes. IEEE Sens J 7:650–657. https://doi.org/10.1109/JSEN.2007.894917
39. We JH, Kim SJ, Cho BJ (2014) Hybrid composite of screen-printed inorganic thermoelectric film and organic conducting polymer for flexible thermoelectric power generator. Energy 73:506–512. https://doi.org/10.1016/j.energy.2014.06.047
40. Chowdhury I, Prasher R, Lofgreen K, et al (2009) On-chip cooling by superlattice-based thin-film thermoelectrics. Nat Nanotechnol 4:235–238. https://doi.org/10.1038/nnano.2008.417
41. Su Y, Lu J, Villaroman D, et al (2018) Free-standing planar thermoelectric microrefrigerators based on nano-grained SiGe thin films for on-chip refrigeration. Nano Energy 48:202–210. https://doi.org/10.1016/j.nanoen.2018.03.054
42. Sun K, Bao Y, Gupta MC (2014) Laser doping of germanium for photodetector applications. In: Reutzel EW (ed) Laser Processing and Fabrication for Solar,

Displays, and Optoelectronic Devices III. International Society for Optics and Photonics, p 918008

43. Wang L, Carlson DE, Gupta MC (2015) Silicon solar cells based on all-laser-transferred contacts. Prog Photovoltaics Res Appl 23:61–68. https://doi.org/10.1002/pip.2395
44. Caffrey PO, Gupta MC (2014) Electrically conducting superhydrophobic microtextured carbon nanotube nanocomposite. Appl Surf Sci 314:40–45. https://doi.org/10.1016/j.apsusc.2014.06.055
45. Lee H, Lim CHJ, Low MJ, et al (2017) Lasers in additive manufacturing: A review. Int. J. Precis. Eng. Manuf. - Green Technol. 4:307–322
46. Hua C, Minnich AJ (2014) Importance of frequency-dependent grain boundary scattering in nanocrystalline silicon and silicon–germanium thermoelectrics. Semicond Sci Technol 29:124004. https://doi.org/10.1088/0268-1242/29/12/124004
47. Ferre Llin L, Mirando F, Samarelli A, et al (2016) (Invited) The Use of Silicon-Germanium Superlattices in Thermoelectric Devices and Microfabricated Generators. ECS Trans 75:469–478. https://doi.org/10.1149/07508.0469ecst
48. Zhu GH, Lee H, Lan YC, et al (2009) Increased Phonon Scattering by Nanograins and Point Defects in Nanostructured Silicon with a Low Concentration of Germanium. Phys Rev Lett 102:196803. https://doi.org/10.1103/PhysRevLett.102.196803
49. Markowski P, Dziedzic A (2008) Planar and three-dimensional thick-film thermoelectric microgenerators. Microelectron Reliab 48:890–896. https://doi.org/10.1016/j.microrel.2008.03.008
50. Rowe DJ, Kortshagen UR (2014) Boron- and phosphorus-doped silicon germanium alloy nanocrystals—Nonthermal plasma synthesis and gas-phase thin film deposition. APL Mater 2:022104. https://doi.org/10.1063/1.4865158
51. Dresselhaus MS, Chen G, Tang MY, et al (2007) New Directions for Low-Dimensional Thermoelectric Materials. Adv Mater 19:1043–1053. https://doi.org/10.1002/adma.200600527
52. Parrish KD, Abel JR, Jain A, et al (2017) Phonon-boundary scattering in nanoporous silicon films: Comparison of Monte Carlo techniques. J Appl Phys 122:125101. https://doi.org/10.1063/1.4993601
53. Pernot G, Stoffel M, Savic I, et al (2010) Precise control of thermal conductivity at the nanoscale through individual phonon-scattering barriers. Nat Mater 9:491–495. https://doi.org/10.1038/nmat2752
54. Wongprakarn S, Pinitsoontorn S, Tanusilp S at, Kurosaki K (2018) Enhancing thermoelectric properties of p-type SiGe alloy through optimization of carrier concentration and processing parameters. Mater Sci Semicond Process 88:239–249. https://doi.org/10.1016/j.mssp.2018.08.020
55. Zhou X, Yan Y, Lu X, et al (2018) Routes for high-performance thermoelectric materials. Mater Today 21:974–988. https://doi.org/10.1016/j.mattod.2018.03.039

56. SNYDER GJ, TOBERER ES (2010) Complex thermoelectric materials. In: Materials for Sustainable Energy. Co-Published with Macmillan Publishers Ltd, UK, pp 101–110
57. Vining CB (1991) A model for the high-temperature transport properties of heavily doped n -type silicon-germanium alloys. J Appl Phys 69:331–341. https://doi.org/10.1063/1.347717
58. Slack GA, Hussain MA (1991) The maximum possible conversion efficiency of silicon-germanium thermoelectric generators. J Appl Phys 70:2694–2718. https://doi.org/10.1063/1.349385
59. Minnich AJ, Lee H, Wang XW, et al (2009) Modeling study of thermoelectric SiGe nanocomposites. Phys Rev B 80:155327. https://doi.org/10.1103/PhysRevB.80.155327
60. Zebarjadi M, Joshi G, Zhu G, et al (2011) Power Factor Enhancement by Modulation Doping in Bulk Nanocomposites. Nano Lett 11:2225–2230. https://doi.org/10.1021/nl201206d
61. Nomura M, Nakagawa J, Sawano K, et al (2016) Thermal conduction in Si and SiGe phononic crystals explained by phonon mean free path spectrum. Appl Phys Lett 109:173104. https://doi.org/10.1063/1.4966190
62. Bachmann M, Czerner M, Heiliger C (2012) Ineffectiveness of energy filtering at grain boundaries for thermoelectric materials. Phys Rev B 86:115320. https://doi.org/10.1103/PhysRevB.86.115320
63. Lahwal AS (2015) Thermoelectric Properties of Silicon Germanium: An Investigation of the Reduction of Lattice Thermal Conductivity and Enhancement of Power Factor. Clemson University
64. Narducci D, Frabboni S, Zianni X (2015) Silicon de novo: energy filtering and enhanced thermoelectric performances of nanocrystalline silicon and silicon alloys. J Mater Chem C 3:12176–12185. https://doi.org/10.1039/C5TC01632K
65. Zamanipour Z, Shi X, Dehkordi AM, et al (2012) The effect of synthesis parameters on transport properties of nanostructured bulk thermoelectric p-type silicon germanium alloy. Phys status solidi 209:2049–2058. https://doi.org/10.1002/pssa.201228102
66. Baldridge T (2012) Laser Sintering of Si-Ge Nanoparticles for Thermoelectric Materials
67. Min G, Rowe DM (1996) Design theory of thermoelectric modules for electrical power generation. IEE Proc - Sci Meas Technol 143:351–356. https://doi.org/10.1049/ip-smt:19960714
68. Basu R, Bhattacharya S, Bhatt R, et al (2014) Improved thermoelectric performance of hot pressed nanostructured n-type SiGe bulk alloys. J Mater Chem A 2:6922–6930. https://doi.org/10.1039/c3ta14259k
69. Dismukes JP, Ekstrom L, Steigmeier EF, et al (1964) Thermal and electrical properties of heavily doped Ge-Si alloys up to 1300°K. J Appl Phys 35:2899–2907. https://doi.org/10.1063/1.1713126

70. Abeles B, Beers DS, Cody GD, Dismukes JP (1962) Thermal conductivity of Ge-Si alloys at high temperatures. Phys Rev 125:44–46. https://doi.org/10.1103/PhysRev.125.44
71. Cheaito R, Duda JC, Beechem TE, et al (2012) Experimental investigation of size effects on the thermal conductivity of silicon-germanium alloy thin films. Phys Rev Lett 109:195901. https://doi.org/10.1103/PhysRevLett.109.195901
72. Dechaumphai E, Lu D, Kan JJ, et al (2014) Ultralow thermal conductivity of multilayers with highly dissimilar Debye temperatures. Nano Lett 14:2448–2455. https://doi.org/10.1021/nl500127c
73. Lin C, Zeng ZG, Ye FJ, et al (2014) Low thermal conductivity of amorphous Si/Si0.75Ge0.25 multilayer films with Au-interlayers. EPL 105:. https://doi.org/10.1209/0295-5075/105/27003
74. Shen B, Zeng Z, Lin C, Hu Z (2013) Thermal conductivity measurement of amorphous Si/SiGe multilayer films by 3 omega method. Int J Therm Sci 66:19–23. https://doi.org/10.1016/j.ijthermalsci.2012.10.022
75. Ye FJ, Zeng ZG, Lin C, Hu ZY (2014) The investigation of electron–phonon coupling on thermal transport across metal–semiconductor periodic multilayer films. J Mater Sci 50:833–839. https://doi.org/10.1007/s10853-014-8643-z
76. Stoib B, Langmann T, Matich S, et al (2012) Laser-sintered thin films of doped SiGe nanoparticles. Appl Phys Lett 100:231907. https://doi.org/10.1063/1.4726041
77. Wingert MC, Kwon S, Hu M, et al (2015) Sub-amorphous Thermal Conductivity in Ultrathin Crystalline Silicon Nanotubes. Nano Lett 15:2605–2611. https://doi.org/10.1021/acs.nanolett.5b00167
78. Hsiao TK, Chang HK, Liou SC, et al (2013) Observation of room erature ballistic thermal conduction persisting over 8.3 μm in SiGe nanowires. Nat Nanotechnol 8:534–538. https://doi.org/10.1038/nnano.2013.121
79. Donmez Noyan I, Gadea G, Salleras M, et al (2019) SiGe nanowire arrays based thermoelectric microgenerator. Nano Energy 57:492–499. https://doi.org/10.1016/j.nanoen.2018.12.050
80. Yokogawa R, Hashimoto S, Takahashi K, et al (2018) Evaluation of Laterally Graded Silicon Germanium Wires for Thermoelectric Devices Fabricated by Rapid Melting Growth. ECS Trans 86:87–93. https://doi.org/10.1149/08607.0087ecst
81. Perez-Taborda JA, Muñoz Rojo M, Maiz J, et al (2016) Ultra-low thermal conductivities in large-area Si-Ge nanomeshes for thermoelectric applications. Sci Rep 6:32778. https://doi.org/10.1038/srep32778
82. Tang J, Wang HT, Lee DH, et al (2010) Holey silicon as an efficient thermoelectric material. Nano Lett 10:4279–4283. https://doi.org/10.1021/nl102931z
83. Lide DR (2016) CRC Handbook of Chemistry and Physics
84. Li J, Han J, Jiang T, et al (2018) Effect of Synthesis Procedure on Thermoelectric Property of SiGe Alloy. J Electron Mater 47:4579–4584. https://doi.org/10.1007/s11664-018-6334-2

85. Wagner M, Span G, Holzer S, Grasser T (2007) Thermoelectric power generation using large-area Si/SiGe pn-junctions with varying Ge content. Semicond Sci Technol 22:S173–S176. https://doi.org/10.1088/0268-1242/22/1/S41
86. Chavez R, Angst S, Hall J, et al (2014) High Temperature Thermoelectric Device Concept Using Large Area PN Junctions. J Electron Mater 43:2376–2383. https://doi.org/10.1007/s11664-014-3073-x
87. Gadea G (2017) Integration of Si/Si-Ge nanostructures in micro-thermoelectric generators. University of Barcelona
88. Bulusu A, Walker DG (2008) Review of electronic transport models for thermoelectric materials. Superlattices Microstruct 44:1–36. https://doi.org/10.1016/j.spmi.2008.02.008
89. Kasper E, Engineers I of E, INSPEC (Information service) (1995) Properties of strained and relaxed Silicon Germanium
90. Kasper E, Lyutovich K (2000) Properties of silicon germanium and SiGe: carbon. Institution of Electrical Engineers
91. Mork KC (2017) Understanding and Improving Plasma Synthesized Silicon Germanium Films for Thermoelectric Applications. University of Minnesota
92. Feser JP (2010) Scalable Routes to Efficient Thermoelectric Materials. University of California, Berkeley
93. Xie K, Mork K, Kortshagen U, Gupta MC (2019) High temperature thermoelectric properties of laser sintered thin films of phosphorous-doped silicon-germanium nanoparticles. AIP Adv 9:015227. https://doi.org/10.1063/1.5085016
94. Xie K, Mork K, Held JT, et al (2018) Quasi continuous wave laser sintering of Si-Ge nanoparticles for thermoelectrics. J Appl Phys 123:094301. https://doi.org/10.1063/1.5018337
95. Lutterotti L, Matthies S, Wenk H-R (1999) MAUD (Material Analysis Using Diffraction): a user friendly Java program for Rietveld Texture Analysis and more. In: Proceeding of the Twelfth International Conference on Textures of Materials (ICOTOM-12). p 1599
96. Iwanaga S, Snyder GJ (2012) Scanning Seebeck Coefficient Measurement System for Homogeneity Characterization of Bulk and Thin-Film Thermoelectric Materials. J Electron Mater 41:1667–1674. https://doi.org/10.1007/s11664-012-2039-0
97. Cahill DG (1990) Thermal conductivity measurement from 30 to 750 K: the 3ω method. Rev Sci Instrum 61:802–808. https://doi.org/10.1063/1.1141498
98. Hänninen T (2013) Implementing the 3-Omega Technique for Thermal Conductivity Measurements. University of Jyväskylä
99. Valalaki K, Nassiopoulou AG (2017) Improved approach for determining thin layer thermal conductivity using the 3 ω method. Application to porous Si thermal conductivity in the temperature range 77–300 K. J Phys D Appl Phys 50:195302. https://doi.org/10.1088/1361-6463/aa69fa

100. Borca-Tasciuc T, Kumar AR, Chen G (2001) Data reduction in 3ω method for thin-film thermal conductivity determination. Rev Sci Instrum 72:2139–2147. https://doi.org/10.1063/1.1353189
101. Zhou A, Wang W, Yang B, et al (2016) Thermal conductivity study of micrometer-thick thermoelectric films by using three-omega methods. Appl Therm Eng 98:683–689. https://doi.org/10.1016/j.applthermaleng.2015.12.145
102. Fardad MA (2000) Catalysts and the structure of SiO2 sol-gel films. J Mater Sci 35:1835–1841. https://doi.org/10.1023/A:1004749107134
103. Sun H-T, Cheng Z-T, Yao X, Wlodarski W (1993) Humidity sensor using sol—gel-derived silica coating on quartz crystal. Sensors Actuators B Chem 13:107–110. https://doi.org/10.1016/0925-4005(93)85336-9
104. Dames C (2013) MEASURING THE THERMAL CONDUCTIVITY OF THIN FILMS: 3 OMEGA AND RELATED ELECTROTHERMAL METHODS. Annu Rev Heat Transf 16:7–49. https://doi.org/10.1615/AnnualRevHeatTransfer.v16.20
105. Ding T, Jannot Y, Degiovanni A (2014) Theoretical study of the limits of the 3ω method using a new complete quadrupole model. Int J Therm Sci 86:314–324. https://doi.org/10.1016/j.ijthermalsci.2014.06.010
106. Xie J, Lee C, Wang M-F, et al (2009) Characterization of heavily doped polysilicon films for CMOS-MEMS thermoelectric power generators. J Micromechanics Microengineering 19:125029. https://doi.org/10.1088/0960-1317/19/12/125029
107. Wang Z, Fiorini P, Leonov V, Van Hoof C (2009) Characterization and optimization of polycrystalline Si $_{70\%}$ Ge $_{30\%}$ for surface micromachined thermopiles in human body applications. J Micromechanics Microengineering 19:094011. https://doi.org/10.1088/0960-1317/19/9/094011
108. Takashiri M, Borca-Tasciuc T, Jacquot A, et al (2006) Structure and thermoelectric properties of boron doped nanocrystalline Si0.8Ge0.2 thin film. J Appl Phys 100:054315. https://doi.org/10.1063/1.2337392
109. Kramer NJ, Schramke KS, Kortshagen UR (2015) Plasmonic Properties of Silicon Nanocrystals Doped with Boron and Phosphorus. Nano Lett 15:5597–5603. https://doi.org/10.1021/acs.nanolett.5b02287
110. Kanaya K, Okayama S (1972) Penetration and energy-loss theory of electrons in solid targets. J Phys D Appl Phys 5:308. https://doi.org/10.1088/0022-3727/5/1/308
111. Lee H, Vashaee D, Wang DZ, et al (2010) Effects of nanoscale porosity on thermoelectric properties of SiGe. J Appl Phys 107:094308. https://doi.org/10.1063/1.3388076
112. Valalaki K, Benech P, Galiouna Nassiopoulou A (2016) High Seebeck Coefficient of Porous Silicon: Study of the Porosity Dependence. Nanoscale Res Lett 11:201. https://doi.org/10.1186/s11671-016-1411-z
113. Hosokawa Y, Tomita K, Takashiri M (2019) Growth of single-crystalline Bi2Te3 hexagonal nanoplates with and without single nanopores during temperature-controlled solvothermal synthesis. Sci Rep 9:10790. https://doi.org/10.1038/s41598-019-47356-5

114. Usenko AA, Moskovskikh DO, Gorshenkov M V., et al (2015) Optimization of ball-milling process for preparation of Si-Ge nanostructured thermoelectric materials with a high figure of merit. Scr Mater 96:9–12. https://doi.org/10.1016/j.scriptamat.2014.10.001
115. Schierning G, Theissmann R, Stein N, et al (2011) Role of oxygen on microstructure and thermoelectric properties of silicon nanocomposites. J Appl Phys 110:113515. https://doi.org/10.1063/1.3658021
116. David T, Benkouider A, Aqua J-N, et al (2015) Kinetics and Energetics of Ge Condensation in SiGe Oxidation. J Phys Chem C 119:24606–24613. https://doi.org/10.1021/acs.jpcc.5b07062
117. Behrenberg D, Franzka S, Petermann N, et al (2012) Photothermal laser processing of thin silicon nanoparticle films: on the impact of oxide formation on film morphology. Appl Phys A 106:853–861. https://doi.org/10.1007/s00339-012-6779-8
118. Lu J, Guo R, Dai W, Huang B (2015) Enhanced in-plane thermoelectric figure of merit in p-type SiGe thin films by nanograin boundaries. Nanoscale 7:7331–7339. https://doi.org/10.1039/c5nr00181a
119. Gadea G, Pacios M, Morata Á, Tarancón A (2018) Silicon-based nanostructures for integrated thermoelectric generators. J Phys D Appl Phys 51:423001. https://doi.org/10.1088/1361-6463/aad683
120. Li HW, Chang CW (2019) Pressure-sensitive liquid phase epitaxy of highly-doped n-type SiGe crystals for thermoelectric applications. Sci Rep 9:1–9. https://doi.org/10.1038/s41598-019-39786-y
121. Claudio T, Stein N, Petermann N, et al (2016) Lattice dynamics and thermoelectric properties of nanocrystalline silicon-germanium alloys. Phys status solidi 213:515–523. https://doi.org/10.1002/pssa.201532500
122. He R, Schierning G, Nielsch K (2018) Thermoelectric Devices: A Review of Devices, Architectures, and Contact Optimization. Adv Mater Technol 3:1700256. https://doi.org/10.1002/admt.201700256
123. Nozariasbmarz A, Zamanipour Z, Norouzzadeh P, et al (2016) Enhanced thermoelectric performance in a metal/semiconductor nanocomposite of iron silicide/silicon germanium. RSC Adv 6:49643–49650. https://doi.org/10.1039/C6RA01947A
124. Romanjek K, Vesin S, Aixala L, et al (2015) High-Performance Silicon–Germanium-Based Thermoelectric Modules for Gas Exhaust Energy Scavenging. J Electron Mater 44:2192–2202. https://doi.org/10.1007/s11664-015-3761-1
125. Murugasami R, Vivekanandhan P, Kumaran S, et al (2018) Thermoelectric power factor performance of silicon-germanium alloy doped with phosphorus prepared by spark plasma assisted transient liquid phase sintering. Scr Mater 143:35–39. https://doi.org/10.1016/j.scriptamat.2017.08.048
126. Raz T, Edelman F, Komem Y, et al (1998) Transport properties of boron-doped crystallized amorphous Si1−xGex films. J Appl Phys 84:4343–4350. https://doi.org/10.1063/1.368697

127. Suen CH, Shi D, Su Y, et al (2017) Enhanced thermoelectric properties of SnSe thin films grown by pulsed laser glancing-angle deposition. J Mater 3:293–298. https://doi.org/10.1016/j.jmat.2017.05.001
128. Kuo CH, Chien HS, Hwang CS, et al (2011) Thermoelectric properties of fine-grained PbTe bulk materials fabricated by cryomilling and spark plasma sintering. Mater Trans 52:795–801. https://doi.org/10.2320/matertrans.M2010331
129. Tajima K, Qiu F, Shin W, et al (2004) Thermoelectric properties of RF-sputtered SiGe thin film for hydrogen gas sensor. Japanese J Appl Physics, Part 1 Regul Pap Short Notes Rev Pap 43:5978–5983. https://doi.org/10.1143/JJAP.43.5978
130. NISHIBORI M, SHIN W, IZU N, et al (2010) Thermoelectric hydrogen sensors using Si and SiGe thin films with a catalytic combustor. J Ceram Soc Japan 118:188–192. https://doi.org/10.2109/jcersj2.118.188
131. Seto JYW (1975) The electrical properties of polycrystalline silicon films. J Appl Phys 46:5247–5254. https://doi.org/10.1063/1.321593
132. Hu GY, O’Connell RF, He YL, Yu MB (1995) Electronic conductivity of hydrogenated nanocrystalline silicon films. J Appl Phys 78:3945–3948. https://doi.org/10.1063/1.359914
133. Sinkkonen J (1980) DC Conductivity of a Random Barrier Network. Phys status solidi 102:621–627. https://doi.org/10.1002/pssb.2221020222
134. Champier D (2017) Thermoelectric generators: A review of applications. Energy Convers Manag 140:167–181. https://doi.org/10.1016/j.enconman.2017.02.070
135. Xie K, Gupta MC (2019) Thermoelectric Properties of SiGe Thin Films Prepared by Laser Sintering of Nanograin Powders. to be Publ
136. Rowe DM (1995) CRC Handbook of Thermoelectrics. CRC Press
137. Bulman G, Barletta P, Lewis J, et al (2016) Superlattice-based thin-film thermoelectric modules with high cooling fluxes. Nat Commun 7:10302. https://doi.org/10.1038/ncomms10302
138. Strasser M, Aigner R, Lauterbach C, et al (2003) Micromachined CMOS thermoelectric generators as on-chip power supply. In: TRANSDUCERS ’03. 12th International Conference on Solid-State Sensors, Actuators and Microsystems. Digest of Technical Papers (Cat. No.03TH8664). IEEE, pp 45–48
139. Zhang W, Yang J, Xu D (2016) A High Power Density Micro-Thermoelectric Generator Fabricated by an Integrated Bottom-Up Approach. J Microelectromechanical Syst 25:744–749. https://doi.org/10.1109/JMEMS.2016.2565504
140. Tan M, Deng Y, Hao Y (2014) Synergistic effect between ordered Bi2Te2.7Se0.3 pillar array and layered Ag electrode for remarkably enhancing thermoelectric device performance. Energy 77:591–596. https://doi.org/10.1016/j.energy.2014.09.041
141. Shakouri A, Yan Zhang (2005) On-chip solid-state cooling for integrated circuits using thin-film microrefrigerators. IEEE Trans Components Packag Technol 28:65–69. https://doi.org/10.1109/TCAPT.2005.843219

142. Stegner AR, Pereira RN, Lechner R, et al (2009) Doping efficiency in freestanding silicon nanocrystals from the gas phase: Phosphorus incorporation and defect-induced compensation. Phys Rev B 80:165326. https://doi.org/10.1103/PhysRevB.80.165326
143. Loureiro J, Mateus T, Filonovich S, et al (2017) Improved thermoelectric properties of nanocrystalline hydrogenated silicon thin films by post-deposition thermal annealing. Thin Solid Films 642:276–280. https://doi.org/10.1016/j.tsf.2017.09.047
144. Yan J, Liao X, Yan D, Chen Y (2018) Review of Micro Thermoelectric Generator. J Microelectromechanical Syst 27:1–18. https://doi.org/10.1109/JMEMS.2017.2782748
145. Zhu T, Liu Y, Fu C, et al (2017) Compromise and Synergy in High-Efficiency Thermoelectric Materials. Adv Mater 29:1605884. https://doi.org/10.1002/adma.201605884
146. Tarkhanyan RH, Niarchos DG (2013) Seebeck coefficient of graded porous composites. J Mater Res 28:2316–2324. https://doi.org/10.1557/jmr.2013.118
147. Zhang B, Zheng T, Wang Q, et al (2018) Stable and low contact resistance electrical contacts for high temperature SiGe thermoelectric generators. Scr Mater 152:36–39. https://doi.org/10.1016/j.scriptamat.2018.03.040

Appendix A: Validation of the 3ω-method

The 3ω-method was developed by Cahill in 1990 [97], which has been widely used to determine the thermal conductivity. In this work, a 3ω-method setup was built, as mentioned in Section 4.6. In order to validate the setup, a silver heater is patterned on a fused quartz substrate. The fused quartz has a thermal conductivity of $\sim 1\ \mathrm{W/m \cdot K}$, which was used as the reference sample.

The parameters setting of the lock-in amplifier (Stanford Research Systems SR830) and the current source (Keithley 6221) are shown in Table A.1

Table A.1 The parameters setting for 3ω-method

I_{rms}	V_{rms}	Time constant	Rooloff	Reserve	Couple	Ground	Filters
5.65 mA	0.9989 V	10 s	12 dB	High	DC	Float	none

The third harmonic voltage readings were recorded by an automated LabVIEW program, as shown in Table A.2. The voltages were the running average of 30 seconds when the read-time readings had a root mean square error less than 3%.

Table A.2 The 3ω voltage readings variation with frequencies

Frequency(Hz)	V_{3x}(mV)	V_{3y}(mV)	V_{3R}(mV)	Θ(°)
1	2.687	-0.357	2.71	-7.57
3	2.437	-0.386	2.47	-9.00
10	2.137	-0.383	2.17	-10.16
30	1.855	-0.401	1.90	-12.20
80	1.605	-0.401	1.65	-14.03
350	1.231	-0.399	1.29	-17.96
1000	0.963	-0.397	1.04	-22.40
3000	0.678	-0.388	0.78	-29.78
9000	0.387	-0.357	0.53	-42.69
15000	0.238	-0.314	0.39	-52.84

20000	0.143	-0.274	0.31	-62.44
25000	0.075	-0.213	0.23	-70.60
30000	0.017	-0.153	0.15	-83.66

The plot of 3ω voltage readings variation with frequencies is shown in Figure A.1.

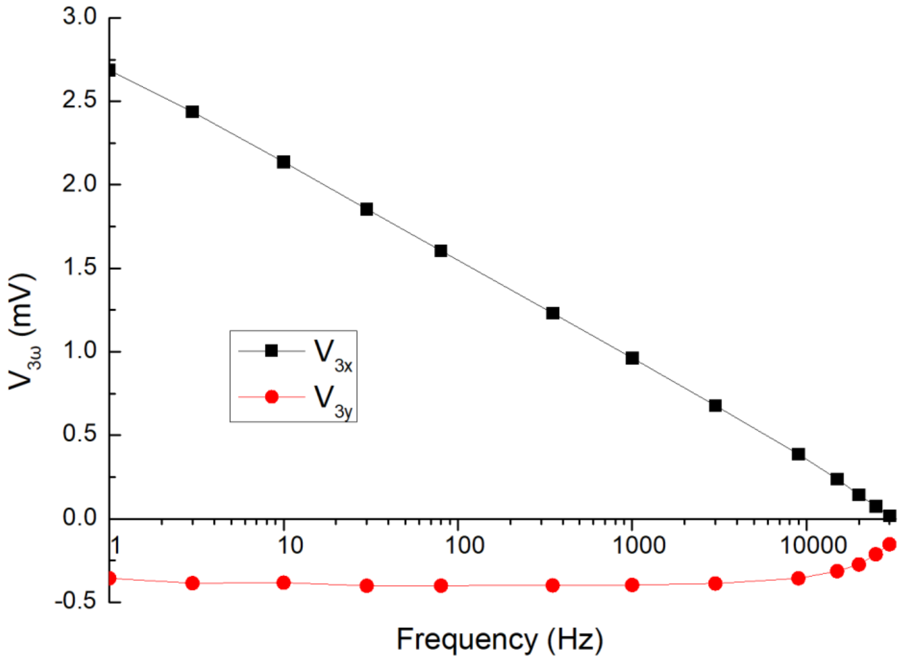

Figure A.1 The plot of 3ω voltage measurement results

Then the electrical conductivities variation with temperature (dR/dT) was measured using a temperature-controlled probe station (Lake Shore TTP-4), as shown in Table A.3.

Table A.3 The resistance variation with temperatures. dR/dT was calculated to be 0.3202

290k		295k		300k		305k		310k	
V	I	V	I	V	I	V	I	V	I
0.1	5.56E-04	0.1	5.51E-04	0.1	5.43E-04	0.1	5.40E-04	0.1	5.36E-04
0.2	1.11E-03	0.2	1.10E-03	0.2	1.09E-03	0.2	1.08E-03	0.2	1.07E-03
0.3	1.66E-03	0.3	1.65E-03	0.3	1.63E-03	0.3	1.62E-03	0.3	1.61E-03
0.4	2.22E-03	0.4	2.20E-03	0.4	2.18E-03	0.4	2.16E-03	0.4	2.14E-03
0.5	2.77E-03	0.5	2.75E-03	0.5	2.72E-03	0.5	2.70E-03	0.5	2.68E-03
R	**180.2**	**R**	**182.048**	**R**	**183.758**	**R**	**185.268**	**R**	**186.595**

The temperature was maintained at different values. Then the current readings were recorded when different compliant voltages were applied. The resistances were calculated based on the $\mathrm{dV/dI}$. Then $\mathrm{dR/dT}$ was calculated to be 0.3202 using a linear fit.

Then the thermal conductivity was calculated using the following equation [97]:

$$\kappa = \frac{V^3}{4\pi l R^2} \cdot \frac{\ln\left(\frac{f_2}{f_1}\right)}{V_{3\omega,1} - V_{3\omega,2}} \cdot \frac{dR}{dT} \qquad \text{Equation A.1}$$

where $V_{3\omega,1}$ and $V_{3\omega,2}$ are the in-phase 3ω voltage at the frequency f_1 and f_2, l is the length of the heater, and R is the electrical resistance.

Here, the linear region was selected. So f_1 and f_2 were 1 and 1000 Hz. Linear fitted $|1/\mathrm{slope}|$ was used for better accuracy. The thermal conductivity was calculated to be $1.08\ \mathrm{W/m \cdot K}$, which agreed well with the reference value.

The uncertainty of κ could be calculated as:

$$\frac{U_\kappa}{\overline{\kappa}} = \sqrt{3^2\left(\frac{U_V}{\overline{V}}\right)^2 + 1^2\left(\frac{U_l}{\overline{l}}\right)^2 + 2^2\left(\frac{U_R}{\overline{R}}\right)^2 + 1^2\left(\frac{U_{slope,3\omega}}{slope_{3\omega}}\right)^2 + 1^2\left(\frac{U_{slope,RT}}{slope_{RT}}\right)^2} \qquad \text{Equation A.2}$$

where U_κ, U_V, U_l, U_R are the uncertainty of the thermal conductivity, first harmonic voltage, length of the heater, and electrical resistance, respectively. The uncertainties of the slopes were obtained directly from curve fitting results.

The uncertainty of an individual parameter has two parts, Type A uncertainty, which is calculated from a series of observations, and Type B uncertainty, which is evaluated using available information (instrumental, environmental, etc.). The sum of uncertainty is calculated as followed using the voltage as an example.

$$U_V = \sqrt{u_A^2 + u_b^2} \qquad \text{Equation A.3}$$

$$u_A = \sqrt{\frac{\sum_{i=1}^{n}(x_i - \overline{x})^2}{n(n-1)}}$$ Equation A.4

The calculation of the uncertainty of each parameter is summarized in Table A.3

Table A.4 Calculation table of the uncertainty of each parameter

	$u_A \cdot$ avg	$u_B \cdot$ avg[1]	$U_x \cdot$ avg
V	0	0.07%	0.07%
l	0	2%	2%
R	0	2%	2%
$slope_{3\omega}$	3.25%	2%	3.81%
$slope_{RT}$	4.2%	2%	4.65%

1. The Type B uncertainties were obtained from the instrument manual and ref. [100].

Therefore, the relative uncertainty of the thermal conductivity ($U_\kappa/\overline{\kappa}$) was calculated as 7.50%. The complete thermal conductivity measurement result is $1.08 \pm 0.08\ \mathrm{W/m \cdot K}$.

Appendix B: MATLAB Code for Heat Spreader Method

```
clc; close all; clear all;

load('Thermalmap.MAT');                 %Thermalmap.MAT
A = imread('optimg.jpg');               %CCD image
const = 6.75*10^12;                     %k = const /(beta^2), obatined from k_i,z/(d_i*d)
mpp = 5.83*10^-6;                       %meter per pix at 1X magnification
magn = 60;                              %magnification

[picx,picy] = size(Thermal);
figure;
image(A);
factor = size(A,1)/size(Thermal,1);     %ccd/thermalmap=factor
disp("Select the normal line:");
disp("1) Use left-click to choose the first point near the heater, then;");
disp("2) Use right-click to choose the second point away from the heater.");
[x,y] = getpts;
switch length(x)
    case 1
        rotatedegree = 0;
    case 2
        rotatedegree = rad2deg(-atan((x(2)-x(1))/(y(2)-y(1))));
    otherwise
        error('invalid selection');
end
A = imrotate(A,rotatedegree,'bilinear','crop');
A = imresize(A,[picx,picy]);
image(A);
hold on ;
Thermal = imrotate(Thermal,rotatedegree,'bilinear','crop');
Thermal(Thermal==0) = NaN;
inpaint_nans(Thermal,4);        %interplot missing data by John D'Errico, file avaiable from Mathworks
imagesc(Thermal);
    colormap('jet');
    colorbar;
    alpha(0.5);
disp("Select the ROI for analysis, temperatures will be horizontally averaged.");
velrect = getrect();
    xmin=round(velrect(1));
    xmax=round(velrect(3)+xmin);
    ymin=round(velrect(2));
```

```
    ymax=round(velrect(4)+ymin);

close all;
ThermalReduced = Thermal(ymin:ymax,xmin:xmax);
tempdrop = mean(ThermalReduced,2);
plot(tempdrop);
disp("Select the range of x:");
disp("1) Use left-click to choose the maximum temperature point.");
disp("2) Use left-click to choose the T_infinite temperature point.");
[x,y] = getpts;
tempdrop = tempdrop(round(x(1)):round(x(2)),:);
distance = linspace(0,length(tempdrop)*factor*mpp/magn,length(tempdrop))';

% Curve fitting for exp+constant
f = @(b,distance) b(1).*exp(b(2).*distance)+b(3);
fcn = fminsearch(@(b) norm(tempdrop - f(b,distance)), ones(4,1),optimset('MaxFunEvals',2000));
% Curve fitting settings

plot(distance,tempdrop);
hold on
plot(distance, f(fcn,distance), '-r')
hold off

kappa = const/(fcn(2)^2);            %fcn(2) = beta
fprintf('\nThermal conductivity is %.2f\n', kappa);
```

Appendix C: List of Publications

1. Xie K, Mork K, Held JT, Mkhoyan KA, Kortshagen U, Gupta MC (2018) Quasi continuous wave laser sintering of Si-Ge nanoparticles for thermoelectrics. *Journal of Applied Physics*, 123(9):094301.

2. Xie K, Mork K, Kortshagen U, Gupta MC (2019) High temperature thermoelectric properties of laser sintered thin films of phosphorous-doped silicon-germanium nanoparticles. *AIP Advances*, 9(1):015227.

3. Xie K, Gupta MC (2019) Thermoelectric Properties of SiGe Thin Films Prepared by Laser Sintering of Nanograin Powders. *Submitted*.

4. Xie K, Gupta MC (2019) High Temperature Thermoelectric Energy Conversion Devices Using Si-Ge Thick Films Prepared by Laser Sintering of Nano/Micro Particles. *Submitted*.

Quasi Continuous Wave Laser Sintering of Si-Ge Nanoparticles for Thermoelectrics

Kai Xie,[1] Kelsey Mork,[2] Jacob T. Held,[3] K. Andre Mkhoyan,[3] Uwe Kortshagen,[2] and Mool C. Gupta[1]

[1] *Department of Electrical and Computer Engineering, University of Virginia, USA*

[2] *Department of Mechanical Engineering, University of Minnesota, USA*

[3] *Department of Chemical Engineering and Materials Science, University of Minnesota, USA*

Silicon-germanium is an important thermoelectric material for high temperature applications. In this study, thin films composed of SiGe nanoparticles were synthesized in a plasma reactor and sintered by millisecond pulse width, quasi continuous wave, near infrared laser of wavelength 1070 nm. We demonstrate that laser sintered SiGe thin films have high electrical and low thermal conductivity, dependent on the surface morphology and dopant concentration. Substrate wetting of laser heating induced molten SiGe was found to play an important role in the final surface morphology of the films. Interconnected percolation structures, formed when proper substrate wetting occurs, were found to be more conductive than the balling structure that formed with insufficient wetting. Laser power was adjusted to maximize dopant reactivation while still minimizing dopant evaporation. After optimizing laser sintering process parameters, the best electrical conductivity, thermal conductivity, and Seebeck coefficient were found to be 70.42 S/cm, 0.84 W/m K, and 133.7 μV/K respectively. We demonstrate that laser sintered SiGe thin films have low thermal conductivity while maintaining good electrical conductivity for high temperature thermoelectric applications.

High temperature thermoelectric properties of laser sintered thin films of phosphorous-doped silicon-germanium nanoparticles

Kai Xie,[1] Kelsey Mork,[2] Uwe Kortshagen,[2] and Mool C. Gupta[1]

[1] *Department of Electrical and Computer Engineering, University of Virginia, Charlottesville, VA 22904, USA*

[2] *Department of Mechanical Engineering, University of Minnesota, Minneapolis, MN 55455, USA*

Silicon-germanium (SiGe) is an important thermoelectric material for high-temperature applications. In this study, we show that the Seebeck coefficient of the laser sintered thin films of phosphorous (P)-doped $Si_{80}Ge_{20}$ nanoparticles increases from -144.9 $\mu V/K$ at room temperature to -390.1 $\mu V/K$ at 873 K. The electrical conductivity increases from 16.1 S/cm at room temperature to 62.1 S/cm at 873 K and demonstrates an opposite trend when compared to bulk nanostructured materials. The thermal conductivity from room temperature to 573 K is essentially constant within the measurement error of our system at ~1.35 $W/m\cdot K$. Therefore, if the thermal conductivity follows a similar temperature dependent trend as reported in past scientific literature, the figure of merit of the thin film $Si_{80}Ge_{20}$ is estimated to be 0.60 at 873 K which is comparable to a value of ~1 for bulk nanostructured materials. This result indicates that thin film P-doped SiGe can provide comparable performance with bulk nanostructured SiGe materials by using nanoparticle laser sintering as an easier, quicker, and more cost-effective processing method.

Thermoelectric Properties of SiGe Thin Films Prepared by Laser Sintering of Nanograin Powders

Kai Xie[1] and Mool C. Gupta[1]

[1] Department of Electrical and Computer Engineering, University of Virginia, Charlottesville, Virginia 22904, USA

Silicon-germanium is an important high-temperature thermoelectric material for thermal to electric energy conversion. This paper focuses on the study of nanograin thermoelectric $Si_{80}Ge_{20}$ thin films. The nanograin $Si_{80}Ge_{20}$ thin films were prepared by a novel method of ball milling to generate nanoparticles and sintered by a quasi-continuous wave, near-infrared laser of wavelength 1070 nm. The electrical and thermal properties variations with different laser sintering power were measured and the sintering mechanism is discussed. The Si/Ge wetting to substrate for a percolation morphology and the control of carrier concentration are found to be the key factors for good electrical conductivity. The stoichiometric ratio of Si and Ge was found to be unchanged in the ball milling and laser sintering process. We demonstrate that the laser sintering was capable of creating well alloyed thermoelectric materials while minimizing grain growth. The thermoelectric parameters like electrical conductivity, thermal conductivity, and figure of merit were measured and the results are compared with other reported bulk and thin-film studies, and the advantages of our method are discussed. We demonstrate that low-cost nanograin SiGe thin films prepared by ball milling and laser sintering process have a comparable thermoelectric figure of merit to other SiGe thermoelectric materials and which can be further improved.

Keywords: Thermoelectric, Nanostructured materials, Semiconductors, Laser processing, Thin films

High Temperature Thermoelectric Energy Conversion Devices Using Si-Ge Thick Films Prepared by Laser Sintering of Nano/Micro Particles

Kai Xie[1] and Mool C. Gupta[1]

[1] *Department of Electrical and Computer Engineering, University of Virginia, Charlottesville, Virginia 22904, USA*

Silicon-germanium (Si-Ge) is used as a high-temperature thermoelectric material due to its high figure of merit and good thermal stability at high temperatures. This paper focuses on the high-temperature thermoelectric energy conversion devices using $Si_{80}Ge_{20}$ thick films prepared by laser sintering of nano/micro particles. The $Si_{80}Ge_{20}$ thick films were prepared by ball milling of Si-Ge material to achieve nano/micro particles and then laser sintering to achieve thick films. The device consists of 3 pairs of n-type phosphorus-doped $Si_{80}Ge_{20}$ legs and p-type boron-doped $Si_{80}Ge_{20}$ legs. The maximum temperature difference of 200 K was achieved when the hot-side temperature was 873 K and the cold-side was kept in the air (no water cooling). The corresponding maximum thermovoltage and output-power were 311.6 mV and $15.85\ \mu W$. The effective power density was calculated as $8.8\ mW/cm^2$. The performance of the device could be further improved by increasing the hot side temperature to about 1000 ℃ and cooling the cold side by water circulation, to generate a larger temperature difference. We demonstrate that this novel fabrication method as an easier, faster, and lower-cost way to fabricate the thick film type thermoelectric devices with high performance. Our demonstrated approach will be suitable for thermoelectric devices for large-area applications on arbitrary shapes. The presented method will also find applications for on-chip cooling and powering, which could substitute MEMS-based fabrication methods for μ-TEGs or other micro-thermoelectric modules with a simpler, cheaper, and faster fabrication process.

Keywords: Thermoelectric, Nanostructured materials, Semiconductors, Laser processing